Dissertation

Measurement-based Performance Evaluation of WiMAX and HSDPA

ausgeführt zum Zwecke der Erlangung des akademischen Grades
eines Doktors der technischen Wissenschaften

eingereicht an der Technischen Universität Wien
Fakultät für Elektrotechnik und Informationstechnik

von

DI Christian Mehlführer

Erlachgasse 129/12-13

1100 Wien

geboren am 6. Juli 1979 in Wien
Matrikelnummer: 9826938

Wien, im September 2009

Begutachter:

Univ. Prof. Dr.-Ing. Markus Rupp

Institut für Nachrichtentechnik und Hochfrequenztechnik
Technische Universität Wien
Österreich

Univ. Prof. Dr.-Ing. Thomas Kaiser

Institut für Kommunikationstechnik
Gottfried Wilhelm Leibniz Universität Hannover
Deutschland

Abstract

In this work, a realistic physical layer performance evaluation of High Speed Downlink Packet Access (HSDPA) as well as IEEE 802.16-2004, commonly referred to as Worldwide Inter-operability for Microwave Access (WiMAX), is provided. The performance evaluation is carried out in two measurement campaigns that took place in an alpine and an urban environment.

Both, WiMAX and HSDPA use adaptive modulation and coding to adapt the channel coding rate and the size of the symbol alphabet to the current channel conditions. Additionally, both systems allow for multiple transmit and multiple receive antennas to increase the spectral efficiency and the reliability of the transmission. While WiMAX utilizes multiple transmit antennas by simple Alamouti space-time coding, HSDPA implements a closed-loop system with channel adaptive spatial precoding. The necessary, quantized channel information is fed back from the user equipment to the base station.

The physical layer performance of both systems is evaluated in terms of measured data throughput. This allows a direct comparison with theoretic bounds like mutual information or channel capacity. Due to inherent system losses (like for example due to the transmission of guard bands, cyclic prefix, or pilot signals), not even a system with an optimum receiver is able to achieve a throughput equal to the mutual information or the channel capacity. Therefore, a so-called *achievable throughput* is defined as performance bound that takes the inherent system losses into account.

This thesis is structured as follows: Chapter 1 introduces the methodology selected for performance evaluation. Furthermore, the scope of work is defined. Chapter 2 covers the WiMAX system and the implemented algorithms. Among others, a novel Approximate Linear Minimum Mean Square Error channel estimator is derived and compared to other channel estimation techniques in the measurement results section of this chapter. In Chapter 3, the HSDPA system is considered. A novel tap-wise Linear Minimum Mean Square Error channel estimator and the implementation of the required feedback are explained in detail before measurement results are presented. In Chapter 4, WiMAX and HSDPA are compared in terms of measured throughput, achievable throughput, mutual information, and channel capacity. Chapter 5 provides a summary of the thesis as well as an outlook to future measurements of the upcoming Long Term Evolution system. In the appendix of this thesis, the measurement setups in alpine and urban scenarios are described in detail. Furthermore, the measurement procedure involving the Vienna MIMO Testbed is explained shortly.

Kurzfassung

In dieser Arbeit wird der Datendurchsatz der Bitübertragungsschicht von High Speed Downlink Packet Access (HSDPA) sowie von IEEE 802.16-2004, auch besser bekannt unter dem Namen Worldwide Inter-operability for Microwave Access (WiMAX), gemessen. Dafür wurden zwei Messkampagnen in einer alpinen und einer städtischen Umgebung durchgeführt.

Sowohl WiMAX als auch HSDPA passen die Größe des Symbolalphabets und die Kanalkodierrate an den Übertragungskanal an. Beide Systeme erlauben die Verwendung von mehreren Sende- bzw. Empfangsantennen, um die spektrale Effizienz bzw. die Zuverlässigkeit der Übertragung zu erhöhen. Während in WiMAX mehrere Sendeantennen mittels Alamoutikodierung angesteuert werden, wird in HSDPA eine kanalabhängige Phasenverschiebung an den einzelnen Sendeantennen angewendet. Die dafür notwendige, quantisierte Kanalinformation wird vom Empfänger an die Basisstation übermittelt.

Die Leistungsfähigkeit der Bitübertragungsschicht wird anhand des gemessenen Datendurchsatzes bestimmt. Dadurch wird ein direkter Vergleich mit theoretischen Grenzen wie der Transinformation des Kanals oder der Kanalkapazität möglich. Da inhärente Systemverluste (zum Beispiel hervorgerufen durch die Übertragung von Schutzbändern, zyklischem Präfix oder Pilotsignalen) vorhanden sind, kann nicht einmal ein System mit optimalem Empfänger einen Datendurchsatz in der Größenordnung der Transinformation des Kanals oder der Kanalkapazität erreichen. Deswegen wird ein sogenannter *erreichbarer Datendurchsatz* definiert, der durch Einbeziehung der inhärenten Systemverluste eine deutlich engere theoretische Grenze darstellt.

Diese Arbeit ist folgendermaßen strukturiert. Zunächst wird in Kapitel 1 die Methodik der Evaluierung und der Umfang der Arbeit vorgestellt. Kapitel 2 behandelt das WiMAX System. Die implementierten Algorithmen, unter anderem ein neuer „Approximate Linear Minimum Mean Square Error" Kanalschätzer, sowie Messergebnisse werden präsentiert. In Kapitel 3 wird das HSDPA System betrachtet. Ein neuer „tap-wise Linear Minimum Mean Square Error" Kanalschätzer, sowie die Berechnung der Rückkanalinformation werden im Detail erklärt bevor Messergebnisse präsentiert werden. In Kapitel 4 werden WiMAX und HSDPA verglichen. Der Vergleich wird anhand von gemessenem Datendurchsatz, erreichbarem Datendurchsatz, Transinformation und Kanalkapazität durchgeführt. Kapitel 5 beinhaltet eine Zusammenfassung der wichtigsten Ergebnisse sowie einen Ausblick auf zukünftige Messungen des Long Term Evolution Systems. Im Anhang dieser Arbeit wird der Messaufbau im alpinen und städtischen Szenario im Detail beschrieben. Die Messprozedur mit dem Vienna MIMO Testbed wird ebenfalls kurz zusammengefasst.

Acknowledgements

First of all, I would like to thank my very good friend Sebastian Caban. Without his endless work and tedious optimizations of the testbed, it would not have been possible to carry out the measurements that are the basis of this thesis. I am furthermore indebted to José Antonio García Naya, Armin Disslbacher-Fink, and Michal Šimko who were very helpful with carrying out the urban measurement campaign. I also want to thank my supervisor Prof. Markus Rupp for his scientific and financial support during the years of my thesis.

The measurements required the implementation of the complete HSDPA and WiMAX physical layers, which of course cannot be accomplished by a single person. I want to thank Amalia Roca who implemented a big part of the WiMAX physical layer during her master thesis. The HSDPA physical layer was developed during the ftw projects C3, C9, C10, and C12, which I was part of. I would like to thank all members of the project teams for their excellent work and their feedback. I would especially like to thank Martin Wrulich, who helped a lot in developing the feedback implementation for the HSDPA measurements. I would also like to thank Prof. Christoph Mecklenbräuker for his input and all the fruitful discussions that led to several joint papers with him. Furthermore, I would like to thank Dagmar Bosanska and Stefan Geirhofer who implemented several parts of the HSDPA simulator during their master theses.

Moreover, I want to thank the radio frequency group of our institute, especially Robert Langwieser, Lukas W. Mayer, and Prof. Arpad L. Scholtz, for their work on the frontend of the testbed and the many radio-frequency related discussions which broadened my horizon.

Such a thesis cannot be accomplished without the right atmosphere, which was provided by everybody in our institute and especially everybody in the MIMO-Lab. I would also like to thank Luca Superiori for continuously cheering me up via Skype. Last but not least, I want to thank all my friends and my family for their support on a personal basis.

Contents

Chapter 1.

Motivation and Scope of Work

The Global System for Mobile communications (GSM), commercially launched in 1991, has been the first fully digital mobile communication system. In September 2008, estimated three billion people (or 80% of the total world-wide subscribers) [1] were connected by GSM. However, GSM in its original form only allowed the users to make mobile phone calls and to send text messages via the Short Message Service (SMS). This changed after data transmission techniques like High-Speed Circuit-Switched Data (HSCSD), General Packet Radio Service (GPRS), and Enhanced Data Rates for GSM Evolution (EDGE) were introduced in the GSM network. With a single time-slot per frame allocated to the user, the data rate supported by HSCSD is 14.4 kbit/s. Using GPRS it is 22.8 kbit/s and with EDGE 68.4 kbit/s [2]. By using multiple time-slots, the maximum data rate can be increased accordingly.

With the launch of the Universal Mobile Telecommunications System (UMTS) [3], the first mobile communication system was available that supported wireless data transmission already in the first released version. By using spreading factors of variable length, the data rate in UMTS can be adjusted up to a maximum of 384 kbit/s. On the contrary, High Speed Downlink Packet Access (HSDPA), introduced by the 3rd Generation Partnership Project (3GPP) in 2002 as an extension to UMTS, uses spreading factors of fixed length while adjusting the data rate by the combination of Adaptive Modulation and Coding (AMC) [4] and the number of spreading codes assigned to the user. The current channel condition required by the AMC is reported by the receiver to the transmitter in regular time intervals. The HSDPA user equipments are classified into several categories depending on the maximum code-block length and the maximum symbol alphabet size supported. A Category 16 user equipment, as it is assumed in this thesis, supports a data rate up to 12.8 Mbit/s within the 5 MHz channel bandwidth.

Another important feature of HSDPA, introduced with 3GPP Release 7 in the year 2007, is Multiple Input Multiple Output (MIMO) operation. Two transmit antennas are employed at the base station to enable spatial precoding in order to increase the Signal to Noise

Ratio (SNR) at the receiver. If two receive antennas are available at the user equipment as well, two spatially separated data streams can be transmitted simultaneously. Although the implementation of the MIMO capability is an additional cost for the network operator, the enhancement in spectral efficiency should —at least in theory— make up for that. A Category 16 user equipment with MIMO capability supports a maximum data rate of 28 Mbit/s.

Between Release 5 (2002) and Release 7 (2007) that were issued by 3GPP, the Institute of Electrical and Electronics Engineers (IEEE) worked on the standardization of 802.16-2004 [5], often referred to as Worldwide Inter-operability for Microwave Access (WiMAX). This standard —at least in the 2004 version— was developed for delivering last mile broadband Internet access as an alternative to cable or Digital Subscriber Line (DSL). Like HSDPA, WiMAX also supports AMC and MIMO. Multiple transmit antennas are incorporated in the standard by Alamouti space-time coding [6]. The maximum data rate of IEEE 802.16-2004 is 15.2 Mbit/s within a 5 MHz channel bandwidth.

Section 1.1 of this introductory chapter defines the requirements for a realistic performance evaluation of modern communication systems. The scope of this thesis with the underlying assumptions are explained in Section 1.2. Finally, a detailed outline of this thesis together with an overview of related work is presented in Section 1.3.

1.1. Performance Evaluation

Today's research is almost entirely based on simulations that only investigate small parts of communication systems. While such a simulation-based approach is good for optimizing a specific algorithm, it does not give information about the impact of this specific algorithm on the performance of the entire communication system. For example, new and enhanced channel estimators that evermore decrease the estimation error can be developed. Such enhanced channel estimators usually have higher complexity than standard least squares or minimum mean squared error approaches. In a communication system, however, it is not the channel estimation error that counts but rather its impact on the physical layer performance, that is, its impact on the data throughput. Although better channel estimators lead to higher throughput, it is not clear how good the channel estimator has to be. For chip manufacturers, the complexity of an algorithm, which is usually closely related to its performance, is crucial. Therefore, algorithms achieving good performance (high physical layer throughput) versus complexity (chip area, power consumption, etc.) trade-offs are desired.

For a meaningful physical-layer performance evaluation of WiMAX and HSDPA, *at least* the following features have to be considered:

Adaptive Modulation and Coding: AMC, which automatically adjusts the modulation and coding schemes based on the current channel condition, is an inherent part of modern communication systems. When comparing different receiver algorithms for a range of input SNRs, it is not sufficient to simulate only a single modulation and coding scheme since it is not clear at which SNR value the difference between the receivers has to be measured. In throughput over SNR plots that inherently include every AMC scheme, the performance of different receivers can be easily compared.

MIMO: Since both WiMAX and HSDPA support multiple transmit and receive antennas, the MIMO processing has to be included in the performance evaluation. In case of MIMO WiMAX, the Alamouti space-time coding can be implemented straightforwardly. In case of MIMO HSDPA, the channel-adaptive spatial precoding requires the implementation of a separate feedback in addition to the AMC feedback.

Standard Compliant Pilot Structure: In order to evaluate the impact of channel estimation errors, it is important that the pilot structure in the transmit signal is implemented just as defined in the standard. Thus, the performance degradation due to the channel estimator will be similar to the one in a final product.

For the performance evaluation of communication systems, different approaches with their individual strengths and weaknesses have been developed. Figure 1.1 compares five approaches in terms of flexibility and the degree of realism that can be achieved. The degree of realism is always closely related to the time needed for implementation. For example, a prototype that requires a tedious real-time implementation offers a much higher degree of realism than a double-precision MATLAB simulation. The four performance evaluation approaches shown in Figure 1.1 are:

Formula-based: In the formula-based evaluation approach [7], the communication system is described by analytic expressions. The analytic expressions give a very good insight into the dependency of the system performance on different parameters. However, modern communication systems are usually too complex to allow for closed form expressions, except for some idealized and oversimplified cases.

Simulation: The simulation approach [7] is preferred by the majority of researchers. It allows the highest degree of flexibility because simulation code can be written and changed very quickly and almost without any restriction. However, simulations always rely on existing channel models that are only available for specific scenarios. If
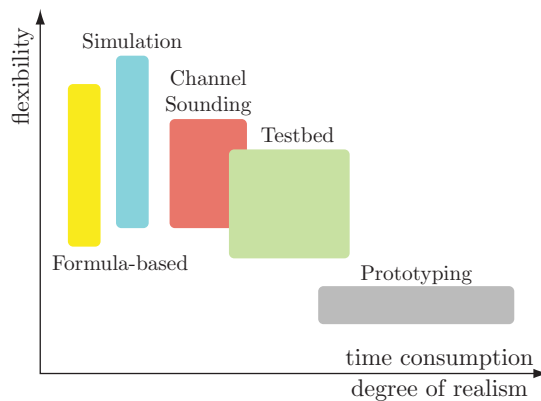
Figure 1.1: System evaluation approaches.

no appropriate channel model is available for the communication system under investigation, only assumptions can be made to model the channel. Also, since simulations are usually carried out in double-precision on a computer, hardly any conclusions about the feasibility of a real-time implementation are drawn.

Channel Sounding: In the channel sounding approach, typical impulse responses of the wireless channel are recorded using a channel sounder [8, 9]. The channel sounder transmits specific training sequences over the wireless channel and records the corresponding receive samples. Using channel estimation techniques, the receive samples are mapped in a subsequent step to impulse responses. By doing so, several effects such as time variation, jitter, or phase noise are neglected. These effects are only considered by the testbed or the prototyping approach explained below. The impulse responses measured with the channel sounder can either be directly used in simulations or as a basis for the derivation of channel models [10] which emulate [11, 12] the wireless channel in a deterministic way. The channel sounding approach has the advantage that the results of one measurement campaign can be used in as many simulations as desired. Also, other workgroups can directly repeat a simulation by using the same measured impulse responses and/or the derived channel models. However, it turns out that carrying out channel sounding experiments requires very specialized and expensive equipment. Therefore, this equipment is usually rent for a short period of time (one week or two) to minimize the equipment costs.

Testbed: In the testbed approach, signals of the system to be investigated are directly transmitted over a wireless channel by using a testbed [13]. Compared to the channel sounding approach, the testbed approach is relatively cheaper [14], especially over longer periods of time. Also, once a testbed has been built, it allows to carry out a multitude of different measurements. For example, the impact of different base

station antennas (and also their spacing) on the throughput of a transmission system can be directly investigated [15, 16]. However, since testbeds usually do not operate in real-time, their application is limited. For example, measurements with AMC at high mobility are not possible since the stringent time requirements for the AMC feedback can usually not be fulfilled.

Prototyping: The prototyping approach is the most tedious of the four approaches. Although during recent years a lot of effort was put into the development of rapid prototyping methods [17, 18], the prototyping approach still requires much more time than all the other approaches. However, since a prototype can already operate quite close to a final product, it allows to draw the most accurate conclusions about the feasibility, the complexity, and also the expected cost of an implementation.

Out of the above described evaluation approaches, the testbed approach, offering a good trade-off between flexibility, degree of realism, and cost, was chosen for the performance evaluation of the WiMAX and the HSDPA systems.

1.2. Scope of Work

In this work, a realistic, testbed-based performance evaluation of the cellular mobile communication systems HSDPA and WiMAX is carried out. In particular, the downlink physical layer between a single base station and a single user is considered. For such a performance evaluation, a complete implementation of the HSDPA and the WiMAX downlink physical layer is required. A MATLAB-based HSDPA simulator was developed at Forschungszentrum Telekommunikation Wien (ftw.) during the C3, C9, C10, and C12 projects [19–21]. A MATLAB-based WiMAX simulator was developed at the Institute of Communications and Radio Frequency Engineering [22, 23]. Although both simulators were available for this thesis, they had to be extended by a large number of features (enhanced channel estimation and channel coding schemes, MIMO capability, feedback, . . .) to implement the entire physical layer. Furthermore, both simulators had to be adapted to support testbed measurements. For example, transmit signal generation and receive signal evaluation had to be separated to be executed on the physically separated testbed transmitter and receiver. The Vienna MIMO Testbed [13] was utilized to measure the performance in two different, representative scenarios, namely an alpine and an urban scenario.

This thesis is based on the following underlying assumptions:

Single Link Physical Layer: The performance evaluation is restricted to the physical layer link between a single user and a single base station.

Linear Radio Frequency Frontends: This assumption is required for the HSDPA feedback calculation, which is based on a linear model of the physical layer. By using highly linear radio frequency frontends, this assumption was fulfilled.

Quasi-Static Channels: All measurements were carried out using a testbed that is not capable of real-time processing. For including AMC in the measurements, it has to be assumed that the channel is quasi-static meaning that the channel is not changing during the time the feedback is calculated at the receiver. It should be noted that all algorithms presented in this thesis are suited for time-variant channels. A measurement in a time-varying channel, however, would have required a real-time implementation of all algorithms and thus the tedious development of a prototype.

Perfect Synchronization: The construction of the Vienna MIMO Testbed ensures perfect timing and frequency synchronization between transmitter and receiver. The effects of imperfect synchronization on the throughput is not part of this work but can be effectively investigated by using this testbed, as it has already been shown for example for WiMAX in [24, 25].

1.3. Outline

The main contributions of this thesis comprised in Chapters 2 to 4 are shortly summarized in this section.

Chapter 2: The WiMAX System

In Chapter 2, the WiMAX physical layer (in particular IEEE 802.16-2004 [5, Section 8.3] and the implementation in [23]) is considered. This chapter is partly based on the publications [26–28]. The physical layer including the relevant receiver algorithms is explained in detail. Emphasis is put on different channel estimation schemes, in particular on a novel Approximate Linear Minimum Mean Square Error (ALMMSE) channel estimator [27]. The feedback is implemented idealized, that is, the modulation and coding scheme that achieves

the highest throughput for a given channel realization is selected after consecutively transmitting all possible schemes. In the results, the actually measured data throughput is compared to a so-called achievable throughput [26] that serves as a performance bound. The losses of different channel coding and channel estimation schemes compared to the best performing receiver are listed in detail [28].

Related Work

The potential performance of WiMAX has been evaluated by simulations presented in a large number of works before, for example [29–38]. In contrast to [29–37], in [38] Single Input Single Output (SISO) simulation results are presented in terms of physical layer data throughput *including* link adaptation. Additionally to simulations, a few testbed measurements and field trials have been carried out before [39–45]. The results of the field trials are usually throughput values given at a specific receive signal strength. However, since for field trials usually commercial prototypes are used, it is not clear what receiver algorithms are implemented. Also, in previous publications no comparisons of actually measured data throughput with appropriate theoretical bounds are available.

Chapter 3: The HSDPA System

In Chapter 3, the HSDPA system is considered. Although this chapter is mostly based on the publications [46–50], a lot of previous work [51–59] was carried out to optimize for example the transmission using the testbed, the frequency-selective space-time equalizer, or the frequency-selective channel estimator. The HSDPA physical layer including the important receiver algorithms is described. In particular, a novel tap-wise Linear Minimum Mean Square Error (LMMSE) channel estimator [50] that achieves a good performance versus complexity trade-off is explained in detail. Since HSDPA employs Hybrid Automated Repeat Request (HARQ) and adaptive precoding, the feedback implementation is more difficult than in case of WiMAX and cannot simply be mimicked by transmitting all possible modulation and coding schemes[1]. Instead, the feedback is realized in a "mini-receiver" that estimates the channel and calculates the optimum modulation and coding scheme as well as the optimum precoding. For doing so, the mini-receiver utilizes a model [49] of the MIMO HSDPA physical layer to predict the post-equalization Signal to Interference and Noise Ratio (SINR). This model, not only useful for calculating the feedback, has already been applied in system level simulations to abstract the HSDPA physical layer [60–63].

---

[1]For example in the double-stream transmission mode there are already 570 different AMC and precoding schemes, not including the HARQ retransmissions.

The closed-loop HSDPA data throughput was measured not only for the standard compliant SISO and 2×2 MIMO schemes but also for a four antenna MIMO scheme to explore potential performance gains. As in the case of WiMAX, the measured data throughput is compared to an achievable throughput [46–48] to quantify the implementation loss.

Related Work

Most of the work published on HSDPA during recent years concentrate on system level simulations [64–73], in which the physical layer is abstracted by an analytical model [74, 75]. Other theoretic works study specific details of the HSDPA physical layer, like for example HARQ [68], receive antenna diversity [76], equalizer architectures [77, 78], radio-frequency hardware impairments [79], or link adaptation [80]. In contrast to the other works cited above, only in [38] SISO simulation results are presented in terms of physical layer data throughput *including* link adaptation. As a performance bound, the data throughput is compared to the Shannon capacity of the Additive White Gaussian Noise (AWGN) channel. In frequency selective fading channels, however, the AWGN channel capacity is not a good performance bound because it only considers the SNR and not the frequency selectivity. A good performance bound should instead be based on the SNR *and* the channel coefficients.

Apart from simulations, HSDPA was also evaluated in some experimental works. In [81], the throughput performance of a SISO HSDPA system is simulated based on so-called drive test measurements. An experimental evaluation of a MIMO HSDPA multiuser detector is provided in [82]. The impact of distributed antenna systems on the HSDPA performance in indoor environments is studied in [83]. Based on extensive measurements with available SISO HSDPA hardware, the same authors provide guidelines for indoor HSDPA network planning and optimization in [84]. The quality of service in a live HSDPA network is investigated in [85]. Throughput measurement results of a SISO HSDPA system are presented in [86] and of a MIMO HSDPA system in [87]. The results in [87] were obtained with a non standard compliant MIMO scheme and are therefore not representative for the system to be deployed in the near future. None of the papers cited above compares the actual data throughput of a standard compliant MIMO HSDPA system with the mutual information and/or the capacity of the wireless channel. Thus, it cannot be inferred from previous publications how close HSDPA gets to the channel capacity predicted by the theory.

Chapter 4: WiMAX-HSDPA Comparison

In Chapter 4, the performance of WiMAX and HSDPA is compared in terms of

1. the measured throughput,
2. the achievable throughput (considering the inherent system losses),
3. the mutual information given by the estimated channel coefficients, and
4. the channel capacity that is obtained by optimum, frequency-selective precoding at the transmitter.

Related Work

Comparisons between WiMAX and HSDPA are scarce and mainly motivated by economic interests of different companies. Only a few potentially unbiased comparisons exist. For example, [88] provides a good introduction to WiMAX and HSDPA and compares several features (latency, maximum data rate, . . .) of the two systems. In [38], the throughputs of SISO WiMAX and SISO HSDPA is simulated. Economic deployment aspects of WiMAX and HSDPA are considered in [89]. System level simulations of both systems are presented in [90]. No direct, measurement-based comparisons between the WiMAX and the HSDPA physical layer throughputs and achievable throughputs seem to be publicly available, motivating the work presented in Chapter 4.

Chapter 2.

The WiMAX System

In this chapter, link level measurement results of WiMAX (in particular IEEE 802.16-2004 [5, Section 8.3] and the implementation in [23]), as well as the signal processing algorithms involved are explained. This chapter is partly based on the publications [26–28] and is organized as follows.

In Section 2.1, a short introduction about WiMAX and the measurement campaigns carried out is provided. The physical layer of WiMAX is described in detail in Section 2.2. Two important parts of the receiver—the channel estimation and the symbol detection—that have a large impact on the overall performance are explained in Section 2.3. After that, a method for optimally selecting the best AMC scheme is presented in Section 2.4. Section 2.5 introduces a so-called "achievable throughput" that is employed as a performance bound in Section 2.6, in which the measurement results are shown. Finally, Section 2.7 summarizes the findings of this chapter.

2.1. WiMAX Introduction

The WiMAX physical layer as defined in IEEE 802.16-2004 [5] was developed to provide wireless internet access for stationary and low-mobility users. In the standard, three different physical layers for WiMAX are defined, namely the Single Carrier (SC) [5, Sections 8.1 and 8.2], the Orthogonal Frequency Division Multiplexing (OFDM) [5, Section 8.3], and the Orthogonal Frequency Division Multiple Access (OFDMA) [5, Section 8.4] physical layers. The SC physical layer is designed for directional radio links with Line-Of-Sight (LOS), whereas the OFDM and OFDMA physical layers are designed for Non-Line-Of-Sight (NLOS) conditions. The OFDM physical layer utilizes 256 narrow-band sub-carriers to modulate the data symbols to be transmitted. Multiple users are supported by Time-Division Multiple Access (TDMA). The OFDMA physical layer, in contrast, provides in addition to TDMA also multiple access by assigning specific sub-carrier subsets to individual users [91]. In this

work, only the link between a single base station and a single user is investigated. Therefore, the OFDM physical layer was chosen for the measurements.

The OFDM physical layer allows to adjust the data rate by AMC. Depending on the channel realization and the receive SNR, one out of seven possible AMC values is selected for the transmission. The AMC values differ in the channel coding rate and the symbol alphabet (2-Pulse Amplitude Modulation (PAM), 4-Quadrature Amplitude Modulation (QAM), 16-QAM, or 64-QAM).

Optionally, multiple transmit antennas can be employed at the base station to utilize spatial diversity. For that, the data symbols are encoded by the simple Alamouti space-time code [6]. In theory, the Alamouti encoding increases the diversity leading in average to larger receive SNR at the same transmit power. Due to the increased receive SNR, the transmission of higher AMC schemes is already supported at lower transmit powers and thus data throughput is improved.

The potential performance of WiMAX has been evaluated by simulations in a multitude of works before, for example [29–38]. In contrast to [29–37], in [38] SISO simulation results are presented in terms of physical layer data throughput *including* link adaptation. Additionally to simulations, a few testbed measurements and field trials have been carried out before [39–45]. The results of the field trials are usually throughput values given at a specific receive signal strength. However, since for field trials usually prototypes of companies are used, it is not clear what receiver algorithms are exactly implemented. Also, in previous publications no comparisons of actually measured data throughput with appropriate theoretical bounds are available.

This motivated our physical layer MIMO WiMAX throughput measurements that were carried out in two extensive measurement campaigns. In the next sections, the WiMAX physical layer, the employed signal processing algorithms, and the results of the measurement campaigns are presented. The first campaign was carried out in an alpine valley in Austria. Due to the fact that scattering objects existed only in the immediate vicinity of the receiver, the propagation channel had a very small mean Root Mean Square (RMS) delay spread of about 260 ns. The second campaign was carried out in the inner city of Vienna, Austria. Here, the propagation conditions are non-line-of-sight with a rather large mean RMS delay spread of about 1.1 µs. The throughput results are compared to a so-called "achievable throughput" that is calculated using the mutual information of the channel.

2.2. Physical Layer Description

In this section, the functional blocks of a (MIMO) WiMAX transmitter, as shown in Figure 2.1, are described.

At first, the data bits to be transmitted over the wireless channel are encoded by one of the three following channel coding schemes:

1. The Reed-Solomon Convolutional Code (RS-CC) mandatory in the IEEE 802.16-2004 standard: This concatenated channel coding scheme consists of a systematic outer Reed-Solomon [92] and an inner convolutional [93] code. The Reed-Solomon code has a codeword length of 255 bytes, a data length of 239 bytes, and a parity length of 16 bytes. Depending on the currently selected AMC value, the Reed-Solomon code is shortened (to allow for smaller block sizes) and punctured. The inner convolutional code of rate $R = 1/2$ is generated by the polynomials 171_{OCT} and 133_{OCT}. This code is a so-called maximum free distance code ($d_{\mathrm{free}} = 10$) of constraint length seven. After puncturing depending on the AMC value, the maximum free distance is reduced to $d_{\mathrm{free}} = 6$ for $R = 2/3$, $d_{\mathrm{free}} = 5$ for $R = 3/4$, and $d_{\mathrm{free}} = 4$ for $R = 5/6$, respectively. For more details on the encoder specification refer to [5, Section 8.3.3.2.1].

2. The Convolutional Turbo Code (CTC) defined as an optional channel code in the IEEE 802.16-2004 standard: This rate $R = 1/2$ code uses a double binary circular recursive systematic convolutional code and is punctured depending on the currently selected AMC value to allow for code rates $R = 2/3$ and $R = 3/4$. The detailed specification of this channel code is given in [5, Section 8.3.3.2.3].

3. A regular Low Density Parity Check (LDPC) code with variable node degree $d_{\mathrm{v}} = 3$: This code is not part of the standard and has been implemented as a benchmark for the two standardized codes above. Different code rates (selected identically to the rates of the RS-CC) are achieved by different encoding matrices. The code matrices are constructed with the progressive edge growth algorithm [94].
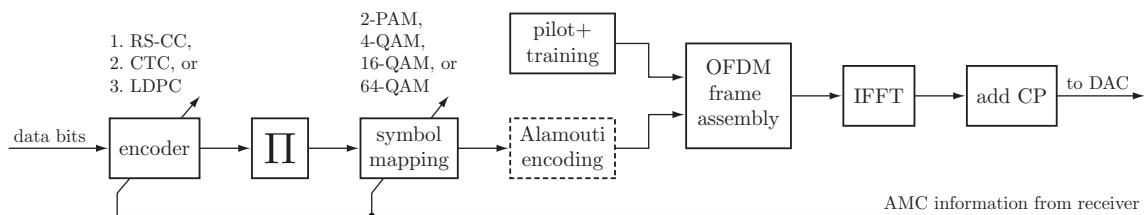
Figure 2.1: Functional blocks of the IEEE 802.16-2004 transmitter.

AMC	Data bits	Modulation	Coding Rate	Max. Throughput
1	4 224 (8 448)	2-PAM (4-QAM)	1/2	1.69 Mbit/s (3.38 Mbit/s)
2	8 448 (11 264)	4-QAM	1/2 (2/3)	3.38 Mbit/s (4.51 Mbit/s)
3	12 672	4-QAM	3/4	5.07 Mbit/s
4	16 896	16-QAM	1/2	6.76 Mbit/s
5	25 344	16-QAM	3/4	10.14 Mbit/s
6	33 792	64-QAM	2/3	13.52 Mbit/s
7	38 016	64-QAM	3/4	15.21 Mbit/s

Table 2.1: The coding rates and modulation alphabets of the seven WiMAX AMC schemes. The values in brackets are for the CTC whenever differing from the values for the RS-CC and the LDPC code. All values in the table are calculated for a frame size of 44 OFDM data symbols transmitted in a frame duration of 2.5 ms and a channel bandwidth of 5 MHz.

After coding, an interleaver is implemented to avoid long runs of low reliable bits at the decoder input. Then, the interleaved bits are mapped adaptively to a symbol alphabet defined by the AMC value. Table 2.1 shows the channel coding rates and the symbol alphabets for the seven AMC schemes. The values given in brackets are for the CTC encoding whenever differing from the values for the RS-CC and the LDPC encoding.

The modulated data symbols are arranged in a frame of OFDM symbols in which also pilot and training symbols, as defined in the IEEE 802.16-2004 specification [5], are inserted. When two transmit antennas at the base station are available, Alamouti [6] encoding of the data symbols is performed. The OFDM symbols are converted to the time-domain by an Inverse Fast Fourier Transform (IFFT) operation. A Cyclic Prefix (CP) of length 1/4-th (10.2 µs) of the total OFDM symbol length is added to avoid inter-symbol-interference in all measured scenarios. Before transmitting over the wireless channel, the signal is normalized by a factor $1/\sqrt{N_\mathrm{T}}$ (with N_T corresponding to the number of transmit antennas), ensuring equal total signal-power for single and multiple antenna transmissions.

2.3. Receiver

At the receiver, first the inverse operations of the transmitter are performed, that is, CP removal, Fast Fourier Transform (FFT), and extraction of data and training symbols, see Figure 2.2. Once the training symbols are extracted from the received frame, they can be utilized in the channel estimator, as explained in Section 2.3.1. The estimated channel coefficients are required by the soft demapper (Section 2.3.2) that calculates Log-likelihood Ratio (LLR) values of the received bits. After deinterleaving, the LLR values are further processed in a channel decoder (Section 2.3.3) to reconstruct the transmitted data bits. Since the construction of the testbed ensures perfect frequency and time synchronization [95], no algorithms are required for that purpose.
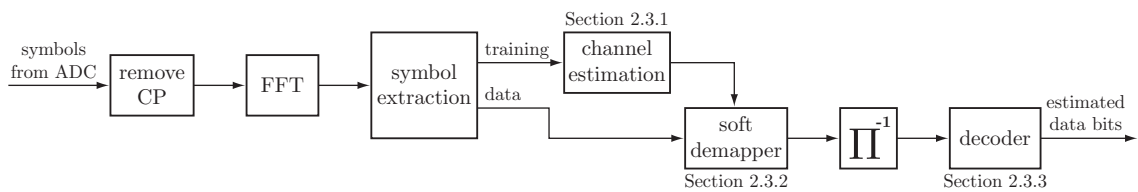
Figure 2.2: Functional blocks of the IEEE 802.16-2004 receiver.

2.3.1. Channel Estimation

In this section, a mathematical system model is defined and will be used to derive a so-called ALMMSE [27] channel estimator. The ALMMSE estimator provides a performance close to the LMMSE estimator at much lower complexity without a-priori knowledge of the channel statistics. As reference, the Least Squares (LS) and a genie-driven channel estimator will be defined.

System Model

The structure of the training sequence in the IEEE 802.16-2004 standard [5] and the resulting system model are described in this section. Since the 2004 WiMAX standard is dedicated to static and quasi-static scenarios, it only defines one OFDM training symbol in the preamble of every frame. It is therefore inherently assumed that the channel stays constant during the transmission of one frame. For this work, a frame duration of 2.5 ms (similar to the 2 ms frame duration of HSDPA) was selected.

At the first transmit antenna, training symbols are only transmitted at the even subcarriers while zeros are transmitted at the odd subcarriers. At the second transmit antenna, only the odd subcarriers are utilized for the training symbols. This structure allows to estimate the links of the MIMO channel individually by using independent SISO channel estimators. Obviously, individual SISO estimators neglect the spatial correlation between the antennas. If antenna correlation is large, better channel estimator performance can be obtained—at the expense of higher complexity—by considering the spatial correlation. However, since WiMAX only supports up to two transmit antennas for which we utilized different polarizations in the measurement setup (see Section A.1), the spatial correlation is very low. Also at the receiver, we employed antennas that were differently polarized and thus have low correlation. Therefore, spatial correlation is neglected from here onwards.

If Inter Carrier Interference (ICI) free transmission is assumed, the received length 100 OFDM training symbol vector $\mathbf{r}$ at one receive antenna can be written as

$$\mathbf{r} = \mathbf{T}\mathbf{h} + \mathbf{w}, \tag{2.1}$$

where the 100×100 diagonal matrix $\mathbf{T}$ comprises the $N = 100$ training symbols[1] of one transmit antenna on the main diagonal. The vector $\mathbf{h}$ contains the channel coefficients of the SISO link between the transmit antenna and the receive antenna to be estimated. The vector $\mathbf{w}$ is additive white Gaussian noise at the receive antenna. Note that due to the given training structure, a direct channel coefficient estimation is only possible for the even subcarriers at the first transmit antenna. At the odd subcarriers, the channel coefficients are obtained by linear interpolation in the frequency domain. The corresponding holds true for the even subcarriers at the second transmit antenna.

LS Estimator

The least squares channel estimator for the system model in Equation (2.1) can be easily verified to be equal to

$$\hat{\mathbf{h}}^{\mathrm{LS}} = \left(\mathbf{T}^{\mathrm{H}}\mathbf{T}\right)^{-1}\mathbf{T}^{\mathrm{H}}\mathbf{r}. \tag{2.2}$$

Since the training symbols on all subcarriers have energy two, as defined in the standard, and due to the diagonal structure of $\mathbf{T}$, the estimator is simplified to

$$\hat{\mathbf{h}}^{\mathrm{LS}} = \frac{1}{4}\mathbf{T}^{\mathrm{H}}\mathbf{r}. \tag{2.3}$$

---

[1] The IEEE 802.16-2004 standard specifies the OFDM physical layer to comprise 256 subcarriers. These 256 subcarriers consist of 200 data+pilot carriers, 55 guard band carriers, and one zero DC carrier. Since the training symbols only allocate every second of the 200 data+pilot carriers, $N = 100$ is obtained.

The LS estimator is therefore of very low complexity (only one complex multiplication per channel coefficient) but unfortunately yields poor performance as will be shown in the measurement results in Section 2.6.

Genie-driven Channel Estimator

In measurements, the true values of the channel coefficients are unknown, making performance comparisons of channel estimators to the perfect channel knowledge case impossible. However, the channel coefficients can be estimated with very high accuracy by simply using all transmitted data symbols of one frame (47 OFDM data symbols in contrast to one OFDM training symbol) in a simple LS estimator. The channel estimator obtained in this way is called genie-driven estimator from here onwards and is used as a benchmark for all other estimators.

LMMSE Estimator

Using the result of Appendix B and the system model in Equation (2.1), the LMMSE channel estimator is obtained as [96, 97]

$$\hat{\mathbf{h}}^{\mathrm{LMMSE}} = \mathbf{R_{hr}}\mathbf{R_{rr}^{-1}}\mathbf{r}, \tag{2.4}$$

in which $\mathbf{R_{hr}}$ denotes the 100×100 cross-correlation matrix and $\mathbf{R_{rr}}$ the 100×100 receive signal auto-correlation matrix. Assuming that the additive noise is uncorrelated with variance σ_w^2, the correlation matrices are calculated as

$$\mathbf{R_{hr}} = \mathbb{E}\{\mathbf{hr}^{\mathrm{H}}\} = \mathbb{E}\{\mathbf{h}\left(\mathbf{h}^{\mathrm{H}}\mathbf{T}^{\mathrm{H}} + \mathbf{w}^{\mathrm{H}}\right)\} = \mathbf{R_{hh}}\mathbf{T}^{\mathrm{H}}, \tag{2.5}$$

$$\mathbf{R_{rr}} = \mathbb{E}\{\mathbf{rr}^{\mathrm{H}}\} = \mathbb{E}\{\left(\mathbf{Th} + \mathbf{w}\right)\left(\mathbf{h}^{\mathrm{H}}\mathbf{T}^{\mathrm{H}} + \mathbf{w}^{\mathrm{H}}\right)\} = \mathbf{TR_{hh}}\mathbf{T}^{\mathrm{H}} + \sigma_w^2\mathbf{I}. \tag{2.6}$$

Thus, the LMMSE estimator is

$$\hat{\mathbf{h}}^{\mathrm{LMMSE}} = \mathbf{R_{hh}}\mathbf{T}^{\mathrm{H}}\left(\mathbf{TR_{hh}}\mathbf{T}^{\mathrm{H}} + \sigma_w^2\mathbf{I}\right)^{-1}\mathbf{r} \tag{2.7}$$

and can be simplified by using the relation $(\mathbf{AB})^{-1} = \mathbf{B}^{-1}\mathbf{A}^{-1}$ twice

$$\hat{\mathbf{h}}^{\mathrm{LMMSE}} = \underbrace{\mathbf{R_{hh}}\left(\mathbf{R_{hh}} + \frac{\sigma_w^2}{4}\mathbf{I}\right)^{-1}}_{\mathbf{F}}\underbrace{\frac{1}{4}\mathbf{T}^{\mathrm{H}}\mathbf{r}}_{\hat{\mathbf{h}}^{\mathrm{LS}}} = \mathbf{F}\hat{\mathbf{h}}^{\mathrm{LS}}. \tag{2.8}$$

The LMMSE estimate is thus the LS channel estimate post-processed (filtered or spectrally smoothed) by the 100×100 matrix $\mathbf{F}$. Since the direct implementation of Equation (2.8)

requires the inversion of a large matrix, it is of very high computational complexity. Also, the accurate estimation of the full correlation matrix $\mathbf{R_{hh}}$ is challenging. Usually, the correlation matrix is estimated by averaging over N_c previously estimated channels $\hat{\mathbf{h}}^{(i)}$; $i = 1 \ldots N_c$:

$$\mathbf{R_{hh}} = \mathbb{E}\{\mathbf{hh}^{\mathrm{H}}\} \approx \hat{\mathbf{R}}_{\mathbf{hh}} = \frac{1}{N_c} \sum_{i=1}^{N_c} \hat{\mathbf{h}}^{(i)} \hat{\mathbf{h}}^{(i)\mathrm{H}}. \tag{2.9}$$

In order to allow the calculation of the matrix inverse in Equation (2.8) at high SNR ($\sigma_w^2 \to 0$), $\hat{\mathbf{R}}_{\mathbf{hh}}$ has to be of full rank. This requires that the number of previously observed channel realizations has to be larger than the length of the channel vector $\mathbf{h}$ ($N_c \geq N$). The computation of the full correlation matrix therefore requires a large number of previously observed channels which are often not available. Note that the condition $N_c \geq N = 100$ is not very strict due to the additive term $\frac{\sigma_w^2}{4}\mathbf{I}$ in Equation (2.8). If this condition is not fulfilled, however, the calculation of the matrix inverse in Equation (2.8) becomes numerically challenging at high SNR.

To overcome both problems—the estimation of the full channel correlation matrix and the high complexity of the large matrix inversion—an approximate LMMSE estimator is introduced now.

Approximate LMMSE Estimator

One possibility to reduce the complexity of the LMMSE estimator in Equation (2.8) is to reduce the size of the correlation matrix $\mathbf{R_{hh}}$ and thus also the size of the filtering matrix $\mathbf{F}$. This can be achieved by partitioning the channel vector $\mathbf{h}$ into M sub-band vectors of length L (with $L \ll N$ and $M = \lfloor \frac{N}{L} \rfloor$):[2]

$$\mathbf{h} = \left[\mathbf{h}_1^{\mathrm{T}}, \ldots, \mathbf{h}_M^{\mathrm{T}}\right]^{\mathrm{T}}. \tag{2.10}$$

Here, the m-th sub-band vector is given by $\mathbf{h}_m \triangleq \left[h_{L(m-1)+1}, \ldots, h_{L(m-1)+L}\right]^{\mathrm{T}}$. The length L can be chosen depending on the coherence bandwidth of the channel or can be set to a fixed value. As it has been shown in [27], a small value of $L = 5$ almost achieves the LMMSE performance even in an LOS scenario, where the frequency correlation is large.

---

[2]The symbols $\lceil . \rceil$ and $\lfloor . \rfloor$ represent the ceiling and floor operators.

Approach of Noh, Lee, and Park

As pointed out in [97], the channel coefficient sub-band vectors $\mathbf{h}_m$ can be estimated by the following low-complexity estimator

$$\hat{\mathbf{h}}_m^{\mathrm{NLP}} = \mathbf{R}_{\mathbf{h}_m\mathbf{h}_m} \left(\mathbf{R}_{\mathbf{h}_m\mathbf{h}_m} + \frac{\sigma_w^2}{4}\mathbf{I} \right)^{-1} \hat{\mathbf{h}}_m^{\mathrm{LS}} = \mathbf{F}_m^{(L)}\hat{\mathbf{h}}_m^{\mathrm{LS}}. \tag{2.11}$$

However, this approximation suffers from an increased Mean Square Error (MSE) at the edges of the subbands created by the partitioning of the channel vector. In [97] this problem is solved by an overlap technique where the channel vector in Equation (2.10) is partitioned into overlapping sub-bands.

The estimator in Equation (2.11) requires the calculation of a separate filter matrix $\mathbf{F}_m^{(L)}$ for every sub-band m and thus the calculation of many matrix inverses.

ALMMSE Estimator

As proposed in [27], the following approach will be used for approximating the LMMSE channel estimator:

1. Calculation of only one correlation matrix $\hat{\mathbf{R}}_{\mathbf{hh}}^{(L)}$ of dimension $L{\times}L$. This matrix is obtained by averaging over the correlation matrices $\hat{\mathbf{R}}_{\mathbf{h}_m\mathbf{h}_m}$.
2. Since the correlation matrix $\hat{\mathbf{R}}_{\mathbf{hh}}^{(L)}$ is independent of the sub-band index m, only one filter matrix $\mathbf{F}^{(L)}$ has to be calculated.
3. Application of this single filter matrix $\mathbf{F}^{(L)}$ to improve the LS channel estimate to near LMMSE accuracy.

The single correlation matrix $\hat{\mathbf{R}}_{\mathbf{hh}}^{(L)}$ of size $L{\times}L$ is obtained as

$$\mathbf{R}_{\mathbf{hh}}^{(L)} = \mathbb{E}\{\mathbf{h}_m\mathbf{h}_m^{\mathrm{H}}\} \approx \hat{\mathbf{R}}_{\mathbf{hh}}^{(L)} \triangleq \frac{1}{MN_{\mathrm{c}}} \sum_{i=1}^{N_{\mathrm{c}}} \sum_{m=1}^{M} \mathbf{h}_m^{(i)}\mathbf{h}_m^{(i)\mathrm{H}}. \tag{2.12}$$

Here, the full-rank-condition for $\hat{\mathbf{R}}_{\mathbf{hh}}^{(L)}$ is reduced to $MN_{\mathrm{c}} \geq L$. If, for example, $L = 10$ is chosen, M can be calculated as $M = \lfloor \frac{N}{L} \rfloor = \lfloor \frac{100}{10} \rfloor = 10$, meaning that the number of required channel realizations is only one. In other words, after performing the LS channel estimation a full rank estimate for the reduced size channel correlation matrix can be found directly.

The reduced size correlation matrix can now be used to calculate the $L{\times}L$ filter matrix $\mathbf{F}^{(L)}$ for post processing the LS channel estimate:

$$\mathbf{F}^{(L)} = \hat{\mathbf{R}}_{\mathbf{hh}}^{(L)} \left(\hat{\mathbf{R}}_{\mathbf{hh}}^{(L)} + \frac{\sigma_w^2}{4}\mathbf{I} \right)^{-1}. \tag{2.13}$$

The ALMMSE estimator for the k-th subcarrier is now given by filtering the LS channel estimate according to

$$\hat{h}_k^{\text{ALMMSE}} = \begin{cases} \mathbf{F}_{k,:}^{(L)} \cdot \left[\hat{h}_1^{\text{LS}}, \dots, \hat{h}_L^{\text{LS}} \right]^T & ; k \leq \frac{L+1}{2} \\ \mathbf{F}_{\lceil \frac{L+1}{2} \rceil,:}^{(L)} \cdot \left[\hat{h}_{k-\lfloor \frac{L-1}{2} \rfloor}^{\text{LS}}, \dots, \hat{h}_{k+\lceil \frac{L-1}{2} \rceil}^{\text{LS}} \right]^T & ; \text{otherwise} \\ \mathbf{F}_{L+k-N,:}^{(L)} \cdot \left[\hat{h}_{N-L+1}^{\text{LS}}, \dots, \hat{h}_N^{\text{LS}} \right]^T & ; k \geq N - \frac{L-1}{2} \end{cases} \qquad (2.14)$$

Here, $\mathbf{F}_{k,:}^{(L)}$ means the k-th row of the filter matrix $\mathbf{F}^{(L)}$. The operation performed in Equation (2.14) is a weighted averaging filter with L coefficients. To avoid transient responses (leading to increased MSE) the LS channel coefficients at the band edges ($k \leq \frac{L+1}{2}$ and $k \geq N - \frac{L-1}{2}$) are filtered with different coefficients (the first and last rows of the matrix $\mathbf{F}^{(L)}$).

2.3.2. Symbol Detection

The purpose of the symbol detector is to estimate the transmitted bits using the received symbols and the estimated channel. Since soft estimates of the bits in form of LLRs (corresponding to the probability of a bit being a "one" or a "zero") yield performance gains of several decibels over hard demapping, only soft demapping will be explained in this section.

Consider the following system model for a flat fading MIMO channel with N_{T} transmit and N_{R} receive antennas

$$\mathbf{y} = \mathbf{H}\mathbf{x} + \mathbf{v}. \qquad (2.15)$$

In this model, $\mathbf{y}$ denotes the $N_{\text{R}} \times 1$ received symbol vector, $\mathbf{H}$ the $N_{\text{R}} \times N_{\text{T}}$ MIMO channel matrix, $\mathbf{x}$ the $N_{\text{T}} \times 1$ transmitted symbol vector, and $\mathbf{v}$ the $N_{\text{R}} \times 1$ additive Gaussian noise vector. This model is directly applicable to one subcarrier of the OFDM physical layer of WiMAX.

The Maximum A-Posteriori (MAP) demapper relates the probability $P(b_l = 1)$ of the transmitted bit b_l being a "one" to the probability $P(b_l = 0)$ of this bit being a "zero". When assuming the noise $\mathbf{v}$ to be circular Gaussian and uncorrelated, the LLR value of the l-th bit in the symbol vector $\mathbf{x}$ is thus calculated as

$$\text{LLR}(b_l) = \log \frac{P(b_l = 1)}{P(b_l = 0)} = \log \frac{\sum_{\mathbf{x}|b_l=1} \exp\left(-\frac{1}{2} \frac{\|\mathbf{H}\mathbf{x} - \mathbf{y}\|_2^2}{\sigma_v^2}\right)}{\sum_{\mathbf{x}|b_l=0} \exp\left(-\frac{1}{2} \frac{\|\mathbf{H}\mathbf{x} - \mathbf{y}\|_2^2}{\sigma_v^2}\right)}. \qquad (2.16)$$

Here, the summation in the nominator is over all transmit symbol vectors $\mathbf{x}$ with bit $b_l = 1$ and the summation in the denominator over all symbol vectors $\mathbf{x}$ with bit $b_l = 0$. A very well known approximation to Equation (2.16) is given by the max-log-MAP demapper, in which the summations in the nominator and denominator are approximated by their maximum values:

$$
\mathrm{LLR}(b_l) \approx \log \frac{\max_{\mathbf{x}|b_l=1} \exp\left(-\frac{1}{2}\frac{\|\mathbf{Hx}-\mathbf{y}\|_2^2}{\sigma_v^2}\right)}{\max_{\mathbf{x}|b_l=0} \exp\left(-\frac{1}{2}\frac{\|\mathbf{Hx}-\mathbf{y}\|_2^2}{\sigma_v^2}\right)} =
$$
$$
= \frac{1}{2\sigma_v^2} \min_{\mathbf{x}|b_l=0}\left(\|\mathbf{Hx}-\mathbf{y}\|_2^2\right) - \frac{1}{2\sigma_v^2} \min_{\mathbf{x}|b_l=1}\left(\|\mathbf{Hx}-\mathbf{y}\|_2^2\right). \tag{2.17}
$$

This approximation avoids the computation of the exponential function of every distance occurring in Equation (2.17). The approximation is very accurate and costs typically only a few tenth of a decibel in terms of SNR [98]. However, the max-log-MAP demapper still requires the calculation of a large number of distances that is exponentially increasing with the number of transmit antennas. This can be solved by sphere decoding which has a much lower (although still exponential) expected complexity than the full search of the MAP receiver [99]. The two minimum searches in Equation (2.17) can be efficiently performed in sphere decoders that use a single tree search [100]. Such a decoder has been implemented in the WiMAX receiver.

SISO/SIMO Demapper

The single transmit antenna case is a special case of Equation (2.15) with a scalar transmit and a scalar receive symbol. If more than one receive antenna is employed, maximum ratio combining is performed by multiplying the receive signal with the Hermitian of the estimated channel vector $\hat{\mathbf{h}}^{\mathrm{H}}$:

$$
\hat{\mathbf{h}}^{\mathrm{H}}\mathbf{y} = \hat{\mathbf{h}}^{\mathrm{H}}\mathbf{h}x + \hat{\mathbf{h}}^{\mathrm{H}}\mathbf{w} \tag{2.18}
$$

Using this modified system model, soft demapping is performed as in Equation (2.17).

Alamouti Receiver

Before explaining the linear receiver for Alamouti-coded transmissions, the Alamouti code [6] is briefly reviewed. The two transmit symbols x_1 and x_2 are transmitted within two successive OFDM symbols on the same subcarrier at two transmit antennas. In the first OFDM symbol, transmit antenna A_1 carries x_1 and transmit antenna A_2 carries x_2. In the second OFDM symbol, transmit antenna A_1 carries $-x_2^*$ and transmit antenna A_2 carries x_1^*.

When assuming that the channel does not change between the transmission of the two OFDM symbols, the transmission can be described as

$$[\mathbf{y}_1, \mathbf{y}_2] = \left[\mathbf{h}^{(1)}, \mathbf{h}^{(2)} \right] \cdot \begin{bmatrix} x_1 & -x_2^* \\ x_2 & x_1^* \end{bmatrix} + [\mathbf{w}_1, \mathbf{w}_2]. \tag{2.19}$$

Here, $\mathbf{h}^{(1)}$ and $\mathbf{h}^{(2)}$ contain the channel coefficients from the first and second transmit antennas to all N_R receive antennas, $\mathbf{y}_1$ and $\mathbf{y}_2$ the N_R receive symbols in the first and second time slot, and $\mathbf{w}_1$ and $\mathbf{w}_2$ the N_R noise symbols in the first and second time slot. Equation (2.19) can be alternatively represented by

$$\underbrace{\begin{bmatrix} \mathbf{y}_1 \\ \mathbf{y}_2^* \end{bmatrix}}_{\tilde{\mathbf{y}}} = \underbrace{\begin{bmatrix} \mathbf{h}^{(1)} & \mathbf{h}^{(2)} \\ \mathbf{h}^{(2)*} & -\mathbf{h}^{(1)*} \end{bmatrix}}_{\tilde{\mathbf{H}}} \cdot \underbrace{\begin{bmatrix} x_1 \\ x_2 \end{bmatrix}}_{\mathbf{x}} + \underbrace{\begin{bmatrix} \mathbf{w}_1 \\ \mathbf{w}_2^* \end{bmatrix}}_{\tilde{\mathbf{w}}}. \tag{2.20}$$

The Alamouti code can be efficiently decoded in a linear receiver by multiplying the received symbol vector $\tilde{\mathbf{y}}$ by the Hermitian of the effective channel matrix $\tilde{\mathbf{H}}$ [6, 101]. In the case of perfect knowledge of $\tilde{\mathbf{H}}$, Equation (2.20) reduces to

$$\tilde{\mathbf{H}}^\mathrm{H} \tilde{\mathbf{y}} = \tilde{\mathbf{H}}^\mathrm{H} \tilde{\mathbf{H}} \mathbf{x} + \tilde{\mathbf{H}}^\mathrm{H} \tilde{\mathbf{w}} = \left(\left\| \mathbf{h}^{(1)} \right\|_2^2 + \left\| \mathbf{h}^{(2)} \right\|_2^2 \right) \mathbf{I} \mathbf{x} + \tilde{\mathbf{H}}^\mathrm{H} \tilde{\mathbf{w}}. \tag{2.21}$$

This linear receiver thus perfectly separates the two transmit symbols x_1 and x_2 allowing for individual soft demapping. In practice, however, the matrix $\tilde{\mathbf{H}}$ is substituted by the estimated channel matrix $\hat{\tilde{\mathbf{H}}}$ leading to imperfect separation of the transmit symbols.

2.3.3. Decoding

The soft bits obtained from the demapper are further processed in the channel decoder. Depending on the channel coding scheme employed, one of the following channel decoders is applied at the receiver.

1. In case of RS-CC coding, the soft bits are first passed to a Viterbi decoder [102, 103] to decode the inner convolutional code. The soft bits from the output of the Viterbi decoder are further processed in a Reed Solomon decoder [92] to obtain the data bits.

2. In case of CTC coding, the soft bits are passed to a Bahl-Cocke-Jelinek-Raviv (BCJR) algorithm [104], which performs maximum a posteriori decoding.

3. In case of LDPC coding, the soft bits are decoded using the sum-product algorithm [105].

2.4. Best AMC Selection

The very limited number of AMC schemes in WiMAX allows a measurement procedure in which all schemes are transmitted consecutively over the same channel [95], as explained in Section A.2.2. Since all schemes are transmitted, later off-line investigation of different feedback schemes is possible. In this section, a so-called "best AMC selection", defined as the one that maximizes the data throughput, is introduced. All WiMAX throughput curves shown in this thesis are obtained using this AMC selection.

At a specific channel realization $c = 1, \ldots, N_{\mathrm{RXpos}}$ and a specific transmit attenuator value $m = 1, \ldots, M_{\mathrm{max}}$, the best instantaneous data throughput is calculated as

$$D_{\mathrm{best}}^{(c,m)} = \max_{i=1\cdots 7} R_i \left(1 - P_i^{(c,m)} \right), \tag{2.22}$$

where R_i corresponds to the data rate of the i-th adaptive modulation and coding scheme (as defined in Table 2.1), and $P_i^{(c,m)} \in \{0, 1\}$ is a frame error indicator. By calculating the throughput in this way, the highest rate AMC scheme that is received correctly, determines the throughput.

The data throughput at one transmit attenuation value is found by averaging over all channel realizations (N_{RXpos} receiver positions) at a specific attenuation m:

$$D_{\mathrm{best,avg}}^{(m)} = \frac{1}{N_{\mathrm{RXpos}}} \sum_{c=1}^{N_{\mathrm{RXpos}}} D^{(c,m)}. \tag{2.23}$$

Note that Equation (2.23) gives the absolute maximum data throughput that is possible with the available transmission schemes. This data rate can only be achieved by a genie driven AMC selection that knows the block errors of all transmission schemes prior to the actual transmission. In a real system, the selection of an appropriate AMC value would have to rely on the channel state information and the estimated noise variance to predict the block errors for all AMC schemes. The non-trivial problem of selecting the appropriate AMC value is not addressed in this work.

2.5. Achievable Throughput

In this section, a so-called "achievable" data throughput that is a performance bound for the measured data throughput will be derived. In this derivation, the variable k denotes the subcarrier index of the OFDM system, c the channel realization index, and m the transmit power attenuation index, as defined in the previous section.

Consider the transmission of a symbol vector over the MIMO channel of the k-th subcarrier of an OFDM system, as defined in Equation (2.15). Then, the mutual information between the transmitted and the received symbol vector is given by [106–109]:

$$I_k^{(c,m)} = \log_2 \det \left(\mathbf{I} + \frac{1}{\sigma_v^2} \mathbf{H}_k^{(c,m)} \mathbf{H}_k^{(c,m)\mathrm{H}} \right) \tag{2.24}$$

The matrix $\mathbf{H}_k^{(c,m)}$ represents the MIMO channel matrix, σ_v^2 the noise variance, and $\mathbf{I}$ the identity matrix. If the transmitter has no knowledge about the channel, in theory a transmission rate corresponding to this mutual information can be achieved. However, current communication systems require that the transmitter adapts the coding rate to the receive SNR. For doing so, the receiver feeds back the AMC value to the transmitter.

For one transmit power attenuation value m, the average mutual information $I_{\mathrm{avg}}^{(m)}$ per subcarrier is calculated by averaging over all sub carriers and the N_{RXpos} different receive antenna positions (the channel realizations)

$$I_{\mathrm{avg}}^{(m)} = \frac{1}{192 \cdot N_{\mathrm{RXpos}}} \sum_{c=1}^{N_{\mathrm{RXpos}}} \sum_{k=1}^{192} I_k^{(c,m)}. \tag{2.25}$$

The average mutual information in Equation (2.25) is in a subsequent step scaled by the bandwidth f_{s} of the WiMAX system. By doing so, a theoretical upper bound for the measured data throughput is obtained when the transmitter has no channel knowledge:

$$D^{(m)} = f_{\mathrm{s}} I_{\mathrm{avg}}^{(m)} \tag{2.26}$$

The mutual information given by Equation (2.26) can never be achieved since the transmission of an OFDM signal requires also the transmission of a cyclic prefix to avoid intersymbol interference as well as a preamble for synchronization and channel estimation. A tighter upper bound, the so-called achievable throughput $D_{\mathrm{achievable}}^{(m)}$, is obtained by accounting for the inherent system losses. The achievable throughput for transmit power attenuation value m is defined as

$$D_{\mathrm{achievable}}^{(m)} = \frac{1}{1+G} \cdot \frac{192}{256} \cdot \frac{N_{\mathrm{data}}}{N_{\mathrm{OFDM}}} \cdot D^{(m)}, \tag{2.27}$$

where G (selected equal to $1/4$ in the measurements) denotes the ratio between cyclic prefix time and useful OFDM symbol time, N_{data} (44 in the measurements) the number of OFDM data symbols, N_{OFDM} (47 in the measurements) the total number of OFDM symbols in one transmission frame, T_{s} the sampling rate of the transmit signal, and $I^{(m)}$ the mutual information as defined in Equation (2.26). The factor $\frac{192}{256}$ is the relation between the number of data subcarriers and the total number of subcarriers. Therefore, the inherent system losses in the measurements yield $D_{\text{achievable}}^{(m)} \approx 0.56 \cdot D^{(m)}$.

Equation (2.27) is used as a performance bound for comparisons with the measured data throughput in the next section.

2.6. Measurement Results

In this section, the throughput measurement results (the solid lines in Figures 2.3, 2.4, 2.6, and 2.7) are presented and compared to the achievable throughput (the dashed lines in Figures 2.3, 2.4, 2.6, and 2.7). In the figures, all throughput curves are plotted over transmit power, average received SNR, and average received signal power. The dots in the result figures represent the inferred mean throughputs, the vertical lines the corresponding 95% confidence intervals, and the corresponding horizontal lines the 2.5% and 97.5% percentiles.

Four different WiMAX transmission systems were measured:

1. a 1×1 SISO system,
2. a 1×2 Single Input Multiple Output (SIMO) system with maximum ratio combining according to Equation (2.18),
3. a 2×1 Alamouti coded system, and
4. a 2×2 Alamouti coded system.

Both Alamouti coded systems were detected with the linear receiver according to Equation (2.21). The maximum throughput of all four transmission systems is 15.21 Mbit/s, as shown in Table 2.1. For each system, the performance was evaluated for the three channel coding schemes (LDPC, CTC, and RS-CC) defined in Section 2.2 and the three channel estimators (genie-driven, ALMMSE, and LS) defined in Section 2.3.1.

2.6.1. Alpine Scenario

Figure 2.3 shows the measured and the achievable throughput of the 1×2 SIMO and the 2×1 Alamouti coded transmission systems in the alpine scenario. The measured throughput is plotted for genie-driven channel estimation and LDPC coding. This combination yields the best throughput results in all measurements and is therefore used as a reference. At a level of 5 Mbit/s, the measured throughput of both systems in Figure 2.3 is about 2 dB worse in SNR than the achievable throughput. This loss is in the same order as the SNR loss of the LDPC channel coding, see also the discussion in Section 2.6.3.

In theory, the 1×2 SIMO system should have an advantage of exactly 3 dB over the 2×1 Alamouti system. This advantage is the result of the additional receive antenna array gain of the SIMO system. In accordance with the theory, Figure 2.3 shows that both the achievable throughput and the measured throughput of the SIMO system are approximately 3 dB better than those of the 2×1 Alamouti system.

Figure 2.3: Achievable and measured throughput of the 1×2 SIMO and the 2×1 Alamouti coded systems (both for genie-driven channel estimation and LDPC coding) in the alpine scenario ("ID 2008-09-23"). Averaging was performed over 484 receiver positions. The solid lines represent the measured throughput, the dashed lines the achievable throughput.

Figure 2.4 shows the measured and the achievable throughput of the SISO and the 2×2 Alamouti coded system in the same alpine scenario. The SNR loss of the SISO system is about the same as the loss of the 1×2 SIMO and the 2×1 Alamouti coded transmission systems in Figure 2.3. However, for the 2×2 Alamouti transmission, the SNR loss of the measured throughput with respect to the achievable throughput increases with increasing SNR. This is the consequence of the non-optimality of the Alamouti code in case of 2×2 transmission. Especially at high SNR, a full-rate code, such as the Golden code [110], is expected to achieve better performance [111].
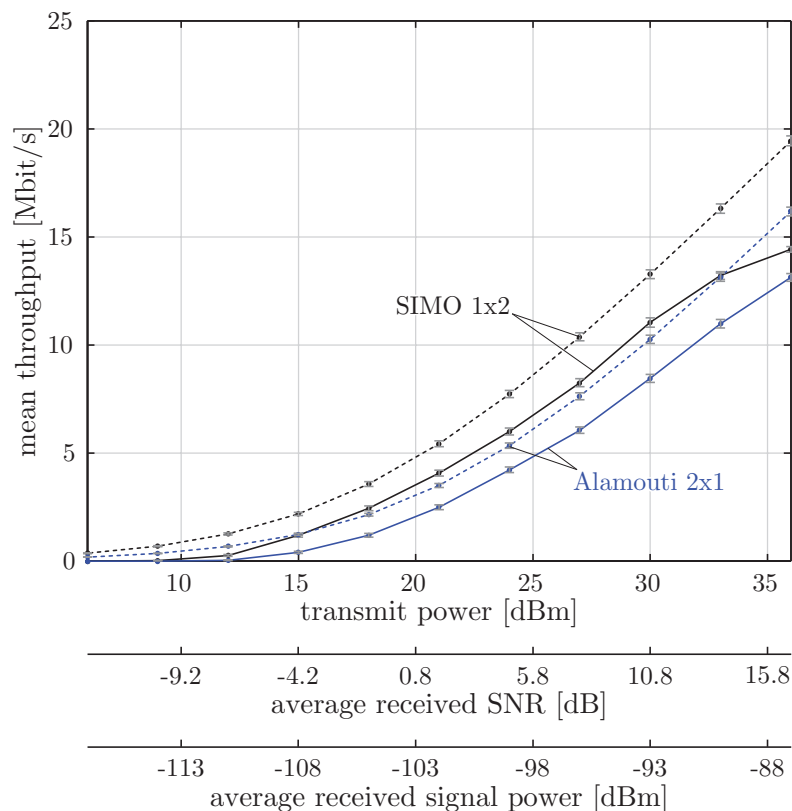

Figure 2.4: Achievable and measured throughput of the 1×1 SISO and the 2×2 Alamouti coded systems (both for genie-driven channel estimation and LDPC coding) in the alpine scenario ("ID 2008-09-23"). Averaging was performed over 484 receiver positions. The solid lines represent the measured throughput, the dashed lines the achievable throughput.

Figure 2.5 shows the SNR losses of the different channel estimation and channel coding schemes with respect to the best performing scheme: genie-driven channel estimation and LDPC coding.

The 2×1 and 2×2 Alamouti coded systems are much more sensitive to channel estimation errors than the SISO and the SIMO systems. This can be explained by the fact that for Alamouti transmission, the available transmit power and thus also the training signal power is equally distributed on the transmit antennas. Therefore only half the training signal power is available per channel coefficient to be estimated. As a consequence, the channel estimation performance is poorer than in the one transmit antenna case.

Figure 2.5 also shows that the SNR loss due to imperfect channel estimation increases more for larger number of receive antennas. The reason for this effect is that the 5 Mbit/s throughput, for which Figure 2.5 is plotted, is achieved by the two receive antenna system at lower transmit power than by the one receive antenna system. The lower transmit power causes worse channel estimator performance and thus the larger SNR loss.

In summary, depending on the actual algorithms implemented, the losses to the best performing scheme can be very large. If only a very simple system with RS-CC coding and LS channel estimation is implemented, the SISO system looses almost 4 dB and the 2×2 Alamouti coded system about 5.5 dB in SNR with respect to the best performing scheme.

Figure 2.5: 1×1 SISO, 1×1 SIMO, 2×1 Alamouti-coded, and 2×2 Alamouti-coded system: SNR losses of the different channel estimators and channel coding schemes with respect to the genie-driven channel estimator and LDPC coding, measured in the alpine scenario (ID "2008-09-23").

2.6.2. Urban Scenario

Figure 2.6 shows the measured and the achievable throughput of the 1×2 SIMO and the 2×1 Alamouti coded transmission systems in the urban scenario. As for the alpine scenario, the measured throughput is plotted for genie-driven channel estimation and LDPC coding. Besides a difference of 1 dB in SNR, caused by the different path loss, the results are very similar to the results of the alpine scenario.

Also in case of the SISO and the 2×2 Alamouti transmissions, shown in Figure 2.7 on the next page, the conclusions of the alpine scenario hold for the urban scenario.
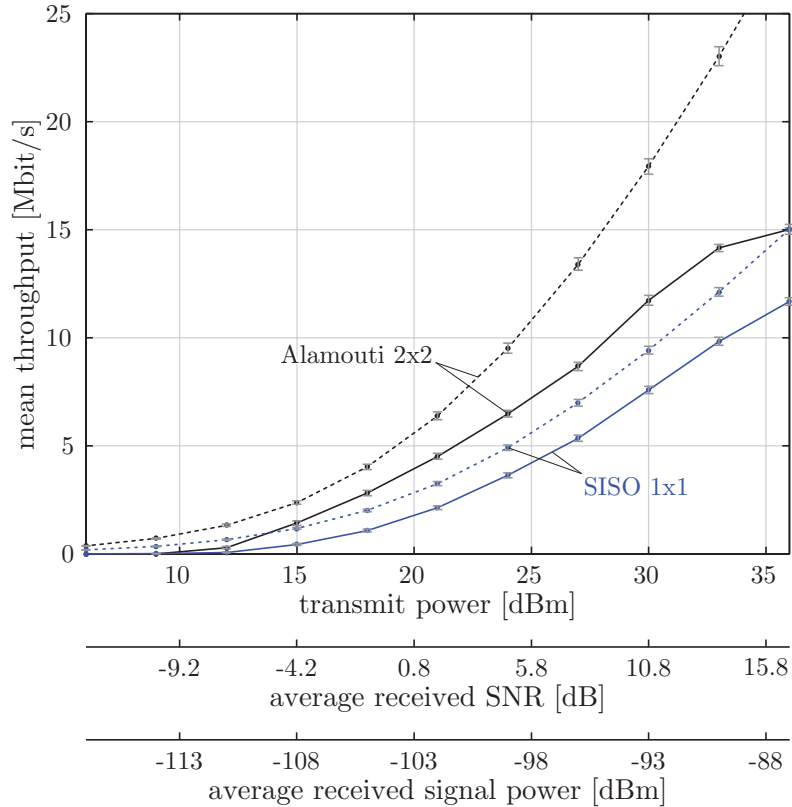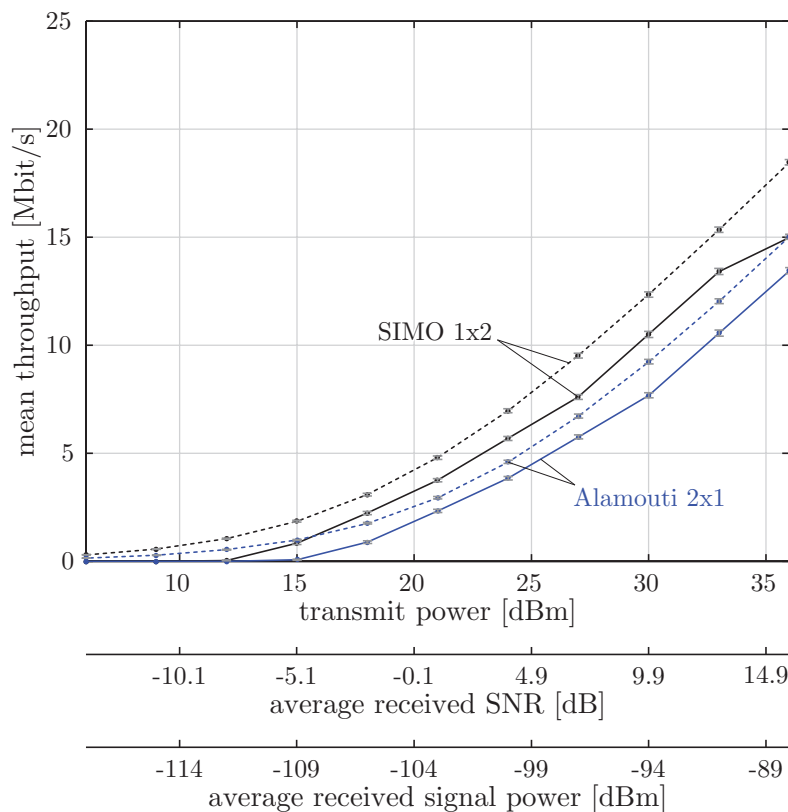

Figure 2.6: Achievable and measured throughput of the 1×2 SIMO and the 2×1 Alamouti coded systems (both for genie-driven channel estimation and LDPC coding) in the urban scenario (ID "2009-01-15c"). Averaging was performed over 484 receiver positions. The solid lines represent the measured throughput, the dashed lines the achievable throughput.
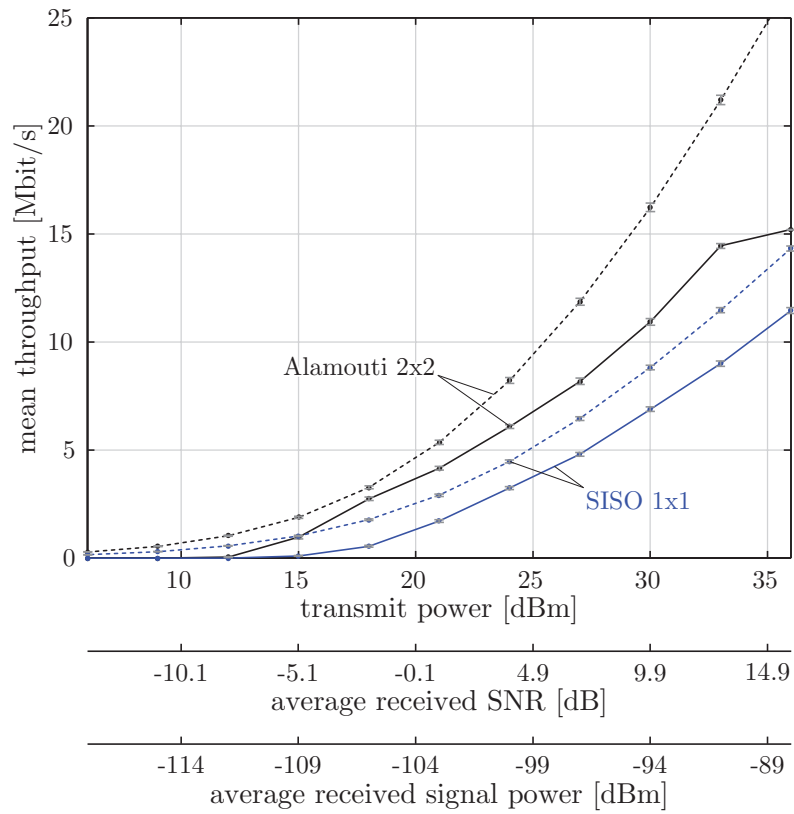
Figure 2.7: Achievable and measured throughput of the 1×1 SISO and the 2×2 Alamouti coded systems (both for genie-driven channel estimation and LDPC coding) in the urban scenario (ID "2009-01-15c"). Averaging was performed over 484 receiver positions. The solid lines represent the measured throughput, the dashed lines the achievable throughput.

Figure 2.8 shows the SNR losses of the different channel estimation and channel coding schemes with respect to the best performing scheme. The losses of the LDPC and CTC channel coding schemes are similar to the losses determined in the alpine scenario in Figure 2.5. For the RS-CC channel coding scheme, however, a significant difference is observed. Especially when a SISO transmission is performed, the SNR loss with RS-CC is significantly greater than in the alpine scenario. Also, for the 2×1 Alamouti and the 1×2 SIMO transmissions, the SNR loss with RS-CC is greater than in the alpine scenario. The reason for this increased loss lies in the frequency selective nature of the wireless channel in the urban scenario, in which a mean RMS delay spread of about 1.1 µs was measured. The large delay spread causes deep fades in the frequency response which seem to be a problem for the RS-CC channel coding. Since the 2×1 Alamouti and the 1×2 SIMO transmission systems provide spatial diversity, the deep fades are not that strong as for the SISO system and the SNR loss is smaller. For the 2×2 Alamouti system, which provides the maximum spatial diversity of the investigated systems, the SNR loss of the RS-CC in the urban scenario is similar to the SNR loss in the alpine scenario. These observations were confirmed by simulations in [26, Figures 14 and 15].
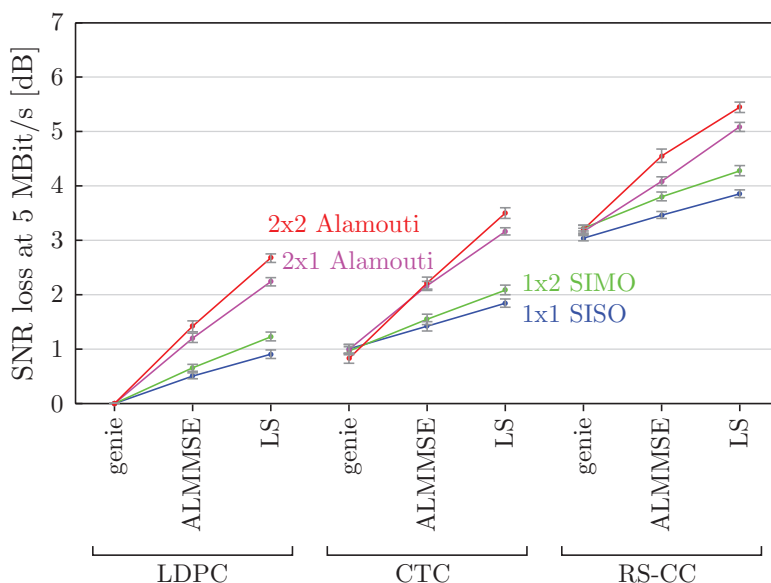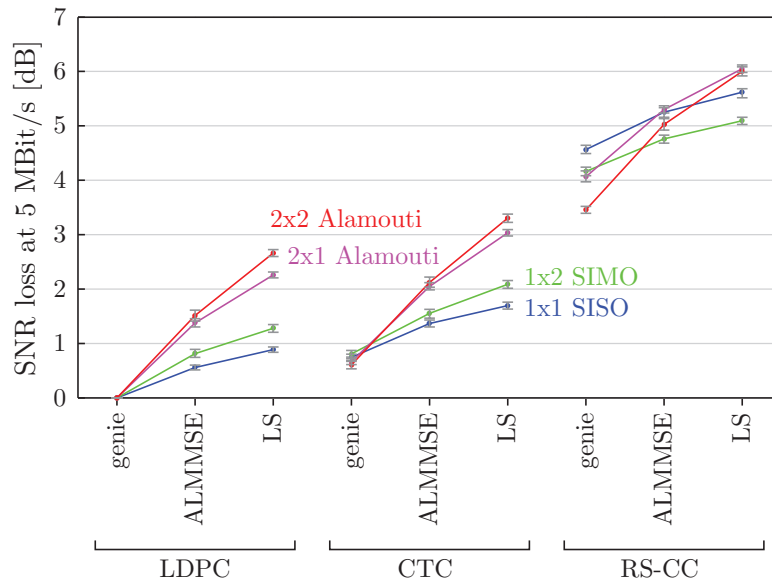

Figure 2.8: 1×1 SISO, 1×1 SIMO, 2×1 Alamouti-coded, and 2×2 Alamouti-coded system: SNR losses of the different channel estimators and channel coding schemes with respect to the genie-driven channel estimator and LDPC coding, measured in the urban scenario ("ID 2009-01-15c").

2.6.3. Discussion of the Throughput Loss

The throughput loss observed in the previous two sections is mainly caused by the non-ideal channel coding. Figure 2.9 shows the simulated SISO throughputs of the three different channel coding schemes (LDPC, CTC, RS-CC) in an AWGN channel. The seven steps of each curve in Figure 2.9 correspond to the AMC schemes. At the third step of 5.07 Mbit/s, the LDPC code looses 1.9 dB (when measuring from the edge of the step) to the achievable throughput in the AWGN channel. This is in accordance with the measured SNR loss of about 2 dB, documented in the previous two sections. The additional loss of the CTC and the RS-CC channel code compared to the LDPC channel code is about 0.5 dB and 3.4 dB. This is also in very good agreement with the losses found in Figures 2.5 and 2.8. Only in the urban scenario, the loss of the RS-CC channel code is significantly greater than expected. The reason for this seems to be the frequency selectivity of the channel, as explained in Section 2.6.2.
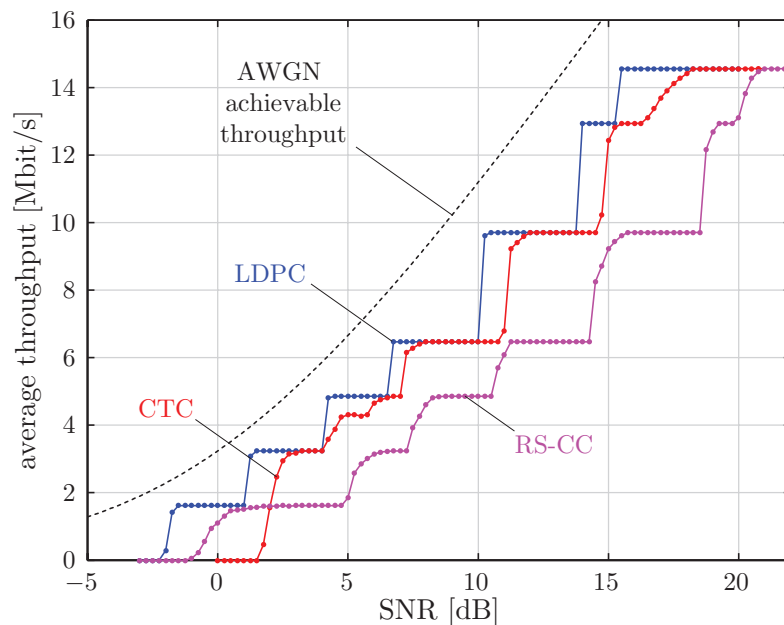
Figure 2.9: Performance of the three channel coding schemes in an AWGN channel, when the optimal scheme out of the seven AMC schemes is selected.

2.7. Summary

MIMO WiMAX throughput measurement results obtained in two extensive measurement campaigns are presented in this chapter. The campaigns were carried out in an alpine valley in Austria and in the inner city of Vienna, Austria. The scenarios differ significantly in the delay spread of the channel. An overview of the measured data throughput for the standard compliant CTC channel coding and the ALMMSE channel estimation is given in Table 2.2. The table clearly shows that throughput gains are mainly given by the utilization of two receive antennas. The exploitation of two transmit antennas by Alamouti space-time coding does not yield a significant, if any, throughput gain due to a high sensitivity of the Alamouti code on channel estimation errors.

	Alpine Scenario		Urban Scenario	
	260 ns mean RMS delay spread		1.1 µs mean RMS delay spread	
	$P_{\text{TX}} = 20\,\text{dBm}$	$P_{\text{TX}} = 30\,\text{dBm}$	$P_{\text{TX}} = 20\,\text{dBm}$	$P_{\text{TX}} = 30\,\text{dBm}$
1×1 SISO	0.9 Mbit/s	6.6 Mbit/s	0.2 Mbit/s	5.9 Mbit/s
2×1 Alamouti	0.7 Mbit/s	7.0 Mbit/s	0.2 Mbit/s	6.3 Mbit/s
1×2 SIMO	2.2 Mbit/s	9.9 Mbit/s	1.5 Mbit/s	8.8 Mbit/s
2×2 Alamouti	1.9 Mbit/s	9.9 Mbit/s	1.3 Mbit/s	8.7 Mbit/s

Table 2.2: Inferred mean measured WiMAX throughput in the alpine and urban scenarios at transmit powers $P_{\text{TX}} = 20\,\text{dBm}$ and $P_{\text{TX}} = 30\,\text{dBm}$. Values in the table are for ALMMSE channel estimation and CTC channel coding.

In order to compare the measured throughput to a performance bound, an achievable throughput was defined. This achievable throughput is calculated based on the mutual information of the channel and a correction term accounting for the inherent losses of the OFDM modulation. Comparing the measured and the achievable throughput shows that the measured throughput looses about 2 dB in SNR when LDPC channel coding and genie-driven channel estimation is employed. This 2 dB loss is similar to the loss of the LDPC channel code in an AWGN channel (see Figure 2.9). The losses for simpler channel coding and channel estimation schemes are analyzed in detail in Figures 2.5 and 2.8.

The measured throughput results presented in this chapter are all based on the "Best AMC Selection" feedback method described in Section 2.4. This method optimally selects the best (throughput-maximizing) AMC scheme. In a real system, however, a method that maps the frequency selective SNR to an AMC scheme is required. Since such a scheme usually suffers from estimation errors, the measured throughput values presented in this chapter can be interpreted as an upper bound for the throughput of a final product.

Further Work

Since the results of this chapter show the non-capacity achieving nature of the Alamouti code very clearly, it would be interesting to measure the performance of a full-rate, full-diversity space-time code, like for example the Golden code [110, 111]. Such an investigation, however, requires new measurement campaigns. Also, it is interesting to study the impact of realistic feedback calculation schemes and compare the performance to the ideal feedback scheme used here.

Chapter 3.

The HSDPA System

In this chapter, link level measurement results of HSDPA, as well as the signal processing algorithms involved are presented. Although this chapter is mostly based on the publications [46–50], a lot of previous work [51–55] was carried out to optimize for example the transmission over the testbed, the frequency-selective space-time equalizer, or the frequency selective channel estimator.

This chapter is organized as follows. In Section 3.1, a short introduction about MIMO HSDPA and the measurement campaigns carried out is provided. A more detailed description of the physical layer is provided in Section 3.2 together with a mathematical system model. Two important parts of the receiver—the channel estimation and the equalization— that have a large impact on the overall performance are explained in Section 3.3. After that, Section 3.4 elaborates on the quantized precoding utilized in the HSDPA standard. A throughput-maximizing feedback calculation method is then presented in Section 3.5. Section 3.6 introduces a so-called "achievable throughput" that is employed as performance bound for the measured throughput in Section 3.7. Finally, Section 3.8 summarizes the findings of this chapter.

3.1. HSDPA Introduction

The HSDPA mode [112] was introduced in Release 5 of UMTS to provide high data rates to mobile users. This is achieved by several techniques [64–67] like fast link adaptation [80] corresponding to the AMC in WiMAX, fast HARQ [68], and fast scheduling. In contrast to the pure transmit power adaptation performed in UMTS, fast link adaptation in HSDPA adjusts the data rate and the number of spreading codes depending on a so-called Channel Quality Indicator (CQI) feedback. MIMO HSDPA [113], recently standardized in Release 7 of UMTS, further increases the maximum downlink data rate by spatially multiplexing two independently coded and modulated data streams. Additionally, channel-adaptive spatial

precoding is implemented at the base station. The standard defines a set of precoding vectors and one of them is chosen based on a so-called Precoding Control Indicator (PCI) feedback obtained from the user equipment.

Most of the work published on HSDPA during recent years concentrate on system level simulations [64–73], in which the physical layer is abstracted by an analytical model [74, 75]. Other theoretic works study specific details of the HSDPA physical layer, like for example HARQ [68], receive antenna diversity [76], equalizer architectures [77, 78], radio-frequency hardware impairments [79], or link adaptation [80]. Only in [38], the physical layer throughput of SISO HSDPA is simulated with link adaptation and compared to the Shannon capacity of the AWGN channel. In frequency selective fading channels, however, the AWGN channel capacity is not a good performance bound because it only considers the SNR and not the frequency selectivity.

Apart from simulations, HSDPA was also evaluated in some experimental works. In [81], the throughput performance of a SISO HSDPA system is simulated based on so-called drive test measurements. An experimental evaluation of a MIMO HSDPA multiuser detector is provided in [82]. The impact of distributed antenna systems on the HSDPA performance in indoor environments is studied in [83]. Based on extensive measurements with available SISO HSDPA hardware, the same authors provide guidelines for indoor HSDPA network planning and optimization in [84]. The quality of service in a live HSDPA network is investigated in [85]. Throughput measurement results of a SISO HSDPA system are presented in [86] and of a MIMO HSDPA system in [87]. The results in [87] were obtained with a non standard compliant MIMO scheme and are thus not representative for the system to be deployed in the near future. None of the papers cited above compares the actual data throughput of a standard compliant MIMO HSDPA system with the mutual information and/or the capacity of the wireless channel. Thus, it cannot be inferred from previous publications how close HSDPA gets to the channel capacity predicted by the theory.

Motivated by this fact, we performed physical layer MIMO HSDPA throughput measurements. In the next sections, results that were obtained in two extensive measurement campaigns (the same campaigns in which also the WiMAX measurements were carried out) are presented. The first campaign took place in an alpine valley in Austria. Here, the propagation channel had a very small mean RMS delay spread of about one chip (260 ns) due to the fact that scattering objects existed only in the immediate vicinity of the receiver. The second campaign was carried out in the inner city of Vienna, Austria. Here, the propagation conditions are non-line-of-sight with a rather large mean RMS delay spread of about 4.3 chips (1.1 µs). The throughput results are compared to a so-called "achievable throughput" that is calculated using the mutual information of the channel. Additionally to the standardized 2×2 MIMO HSDPA system, also a four transmit antenna HSDPA system was defined and measured to explore future enhancements of the standard.

3.2. Physical Layer Description

In this section, the Code Division Multiple Access (CDMA) physical layer of (MIMO) HSDPA and its mathematical representation is described. After introducing all mathematical symbols, two system models are defined. The first model is required for deriving the so-called tap-wise LMMSE channel estimator in Section 3.3.1. The second model is necessary for calculating the equalizer in Section 3.3.2. Both system models describe a general (MIMO) HSDPA system and do not imply any restrictions on the number of data streams, the number of antennas, and the precoding matrices. The only restrictive assumption made in this chapter is that only one user per subframe is scheduled by the base station. This assumption is necessary because of the immense hardware effort required for multi-user measurements. It should also be noted that multi-user scheduling for HSDPA is currently a topic in research [114–116] and it is still an open question how it can be implemented optimally.

In MIMO HSDPA, a user can receive several spatially multiplexed data streams simultaneously. The number of data streams is selected by the scheduler in the base station and is denoted as N_{s} henceforth. Each data bit stream is rate 1/3 Turbo encoded, rate matched, symbol mapped, and spread using a specific number of spreading sequences of length 16. The resulting code rate at the output of the rate matching, the size of the symbol alphabet, as well as the number of spreading sequences is determined by the scheduler depending on the CQI feedback obtained from the User Equipment (UE). The n_{s}-th spread data chip sequence at time instant k is denoted by the length L_{c} column vector $\mathbf{a}_k^{(n_{\mathrm{s}})} = \left[a_k^{(n_{\mathrm{s}})}, \ldots, a_{k+L_{\mathrm{c}}-1}^{(n_{\mathrm{s}})} \right]^{\mathrm{T}}$ with $n_{\mathrm{s}} = 1 \ldots N_{\mathrm{s}}$ (see Figure 3.1). These N_{s} sequences can be stacked into a matrix $\mathbf{A}_k$ and a vector $\mathbf{a}_k$ to form a compact representation:

$$\mathbf{A}_k = \left[\mathbf{a}_k^{(1)}, \ldots, \mathbf{a}_k^{(N_{\mathrm{s}})} \right] \quad \text{and} \quad \mathbf{a}_k = \mathrm{vec}\left(\mathbf{A}_k \right). \tag{3.1}$$

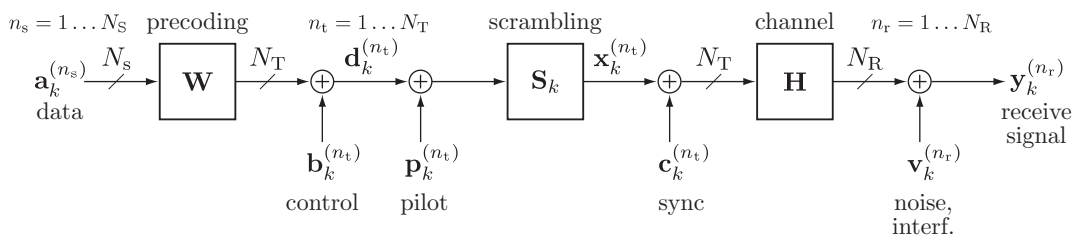**Figure 3.1:** Generalized system model of the HSDPA physical layer.

The data chip streams are spatially precoded by multiplying with an $N_\mathrm{T} \times N_\mathrm{s}$ dimensional precoding matrix

$$\mathbf{W} = \begin{bmatrix} w^{(1,1)} & \cdots & w^{(1,N_\mathrm{s})} \\ \vdots & \ddots & \vdots \\ w^{(N_\mathrm{T},1)} & \cdots & w^{(N_\mathrm{T},N_\mathrm{s})} \end{bmatrix}. \tag{3.2}$$

Depending on the PCI feedback obtained from the user equipment, the precoding matrix $\mathbf{W}$ is chosen from a predefined set of matrices (see Section 3.4) by the scheduler. More information about the calculation and implementation of the PCI feedback is provided in Section 3.5.

After precoding, the spread control channel chip streams $\mathbf{b}_k^{(1)} \ldots \mathbf{b}_k^{(N_\mathrm{T})}$ are added to the precoded data chip streams on all N_T transmit antennas. The sum of data and control channel chip streams is denoted as $\mathbf{d}_k^{(1)} \ldots \mathbf{d}_k^{(N_\mathrm{T})}$. Furthermore, the spread pilot channel chip streams $\mathbf{p}_k^{(1)} \ldots \mathbf{p}_k^{(N_\mathrm{T})}$ that are used for channel estimation at the receiver are added. Analogous to Equation (3.1), the symbols $\mathbf{B}_k, \mathbf{b}_k, \mathbf{D}_k, \mathbf{d}_k, \mathbf{P}_k, \mathbf{p}_k$ are defined:

$$\mathbf{B}_k = \begin{bmatrix} \mathbf{b}_k^{(1)}, \ldots, \mathbf{b}_k^{(N_\mathrm{T})} \end{bmatrix} \quad \text{and} \quad \mathbf{b}_k = \mathrm{vec}\left(\mathbf{B}_k\right),$$
$$\mathbf{D}_k = \begin{bmatrix} \mathbf{d}_k^{(1)}, \ldots, \mathbf{d}_k^{(N_\mathrm{T})} \end{bmatrix} \quad \text{and} \quad \mathbf{d}_k = \mathrm{vec}\left(\mathbf{D}_k\right),$$
$$\mathbf{P}_k = \begin{bmatrix} \mathbf{p}_k^{(1)}, \ldots, \mathbf{p}_k^{(N_\mathrm{T})} \end{bmatrix} \quad \text{and} \quad \mathbf{p}_k = \mathrm{vec}\left(\mathbf{P}_k\right). \tag{3.3}$$

After adding the pilot sequences $\mathbf{p}_k$, the chip streams of all transmit antennas are scrambled by multiplying with the scrambling sequence $\mathbf{S}_k = \mathrm{diag}\left[s_k, \ldots, s_{k+L_\mathrm{c}-1}\right]$ of the base station. Synchronization channels $\mathbf{c}_k^{(1)} \ldots \mathbf{c}_k^{(N_\mathrm{T})}$ are finally added before the signals are transmitted over the wireless frequency-selective channel $\mathbf{H}$. The channel matrix $\mathbf{H}$ contains the complex impulse responses between every transmit and receive antenna. Since the exact composition of the matrix $\mathbf{H}$ depends on the type of system model chosen, the detailed definitions will be given in the next two sections.

At the receiver, the signals at all N_R receive antennas are additively impaired by $\mathbf{v}_k^{(1)} \ldots \mathbf{v}_k^{(N_\mathrm{R})}$ denoting interference of other base stations and thermal noise. Finally, the received signal that is further processed in the digital baseband receiver is $\mathbf{y}_k^{(1)} \ldots \mathbf{y}_k^{(N_\mathrm{R})}$. The symbols $\mathbf{C}_k$, $\mathbf{c}_k, \mathbf{V}_k, \mathbf{v}_k, \mathbf{Y}_k$, and $\mathbf{y}_k$ are defined in the same way as in Equation (3.1):

$$\mathbf{C}_k = \begin{bmatrix} \mathbf{c}_k^{(1)}, \ldots, \mathbf{c}_k^{(N_\mathrm{T})} \end{bmatrix} \quad \text{and} \quad \mathbf{c}_k = \mathrm{vec}\left(\mathbf{C}_k\right),$$
$$\mathbf{V}_k = \begin{bmatrix} \mathbf{v}_k^{(1)}, \ldots, \mathbf{v}_k^{(N_\mathrm{R})} \end{bmatrix} \quad \text{and} \quad \mathbf{v}_k = \mathrm{vec}\left(\mathbf{V}_k\right),$$
$$\mathbf{Y}_k = \begin{bmatrix} \mathbf{y}_k^{(1)}, \ldots, \mathbf{y}_k^{(N_\mathrm{R})} \end{bmatrix} \quad \text{and} \quad \mathbf{y}_k = \mathrm{vec}\left(\mathbf{Y}_k\right). \tag{3.4}$$

3.2.1. System Model for the Channel Estimation

For the derivation of the channel estimator it is convenient to define an individual MIMO channel matrix for every tap delay of the length L_{h} channel. In this model, the $N_{\mathrm{T}} \times N_{\mathrm{R}}$ dimensional channel matrix at delay m $(m = 0, \ldots, L_{\mathrm{h}} - 1)$ is defined as

$$\tilde{\mathbf{H}}_m = \begin{bmatrix} h_m^{(1,1)} & \ldots & h_m^{(1,N_{\mathrm{R}})} \\ \vdots & \ddots & \vdots \\ h_m^{(N_{\mathrm{T}},1)} & \ldots & h_m^{(N_{\mathrm{T}},N_{\mathrm{R}})} \end{bmatrix}. \tag{3.5}$$

Using this definition of the channel matrix and the matrix descriptions of the HSDPA signals in Equations (3.1), (3.3), and (3.4), the receive signal can be compactly written as

$$\mathbf{Y}_k = \sum_{m=0}^{L_{\mathrm{h}}-1} \Big(\mathbf{S}_{k-m} \underbrace{\overbrace{(\mathbf{A}_{k-m}\mathbf{W}^{\mathrm{T}} + \mathbf{B}_{k-m}}_{\mathbf{D}_{k-m}} + \mathbf{P}_{k-m})}^{\mathbf{X}_{k-m}} + \mathbf{C}_{k-m} \Big) \tilde{\mathbf{H}}_m + \mathbf{V}_k. \tag{3.6}$$

3.2.2. System Model for the Equalizer Calculation

For the purpose of the equalizer calculation it is better to define a channel matrix that exhibits a Block-Toeplitz structure. Thus, the frequency selective link between the n_{t}-th transmit and the n_{r}-th receive antenna is modeled by the $L_{\mathrm{f}} \times L_{\mathrm{c}}$ dimensional Toeplitz matrix

$$\mathbf{H}^{(n_{\mathrm{r}},n_{\mathrm{t}})} = \begin{bmatrix} h_0^{(n_{\mathrm{r}},n_{\mathrm{t}})} & \ldots & h_{L_{\mathrm{h}}-1}^{(n_{\mathrm{r}},n_{\mathrm{t}})} & 0 \\ \ddots & & & \ddots \\ 0 & h_0^{(n_{\mathrm{r}},n_{\mathrm{t}})} & \ldots & h_{L_{\mathrm{h}}-1}^{(n_{\mathrm{r}},n_{\mathrm{t}})} \end{bmatrix} \; ; 1 \le n_{\mathrm{r}} \le N_{\mathrm{R}}, 1 \le n_{\mathrm{t}} \le N_{\mathrm{T}}, \tag{3.7}$$

where the $h_m^{(n_{\mathrm{r}},n_{\mathrm{t}})}$ $(m = 0, \ldots, L_{\mathrm{h}} - 1)$ represent the channel impulse response between the n_{t}-th transmit and the n_{r}-th receive antenna. The entire frequency selective MIMO channel is modeled by a block matrix $\mathbf{H}$ consisting of $N_{\mathrm{R}} \times N_{\mathrm{T}}$ Toeplitz matrices

$$\mathbf{H} = \begin{bmatrix} \mathbf{H}^{(1,1)} & \ldots & \mathbf{H}^{(1,N_{\mathrm{T}})} \\ \vdots & \ddots & \vdots \\ \mathbf{H}^{(N_{\mathrm{R}},1)} & \ldots & \mathbf{H}^{(N_{\mathrm{R}},N_{\mathrm{T}})} \end{bmatrix}. \tag{3.8}$$

Using this definition of the channel matrix, the identity matrix $\mathbf{I}_{N_\mathrm{T}}$ of dimension $N_\mathrm{T} \times N_\mathrm{T}$, and the vector descriptions of the HSDPA signals in Equations (3.1), (3.3), and (3.4), the receive signal can be compactly written as

$$\mathbf{y}_k = \mathbf{H} \cdot \left\{ \overbrace{\left(\mathbf{I}_{N_\mathrm{T}} \otimes \mathbf{S}_k\right) \big[\underbrace{(\mathbf{W} \otimes \mathbf{I}_{L_\mathrm{c}})\mathbf{a}_k + \mathbf{b}_k}_{\mathbf{d}_k} + \mathbf{p}_k \big] + \mathbf{c}_k}^{\mathbf{x}_k} \right\} + \mathbf{v}_k. \tag{3.9}$$

3.3. Receiver

In this section, the specific implementation of the digital baseband HSDPA receiver is explained. In particular, a tap-wise LMMSE channel estimator originally presented in [50] and the equalizer with interference cancelation will be explained and derived.

3.3.1. Channel Estimation

Channel estimation in Wideband Code Division Multiple Access (W-CDMA) based networks is strongly affected by interference that can be divided into intra-cell and inter-cell interference. At the base station usually only a small amount of power (approx. 10%) is dedicated to the pilot channels that can be applied for channel estimation. The remaining power is dedicated to all other channels and is thus considered as intra-cell interference for the channel estimator. The amount of intra-cell interference increases with the number of users receiving data in one cell since more spreading codes are used simultaneously at the base station. Furthermore, the intra-cell interference also increases with the number of transmit antennas at the base station since the same spreading codes are reused at each transmit antenna. Inter-cell interference, on the contrary, only becomes crucial at the cell edges where the received power of the desired base station is in the order of the received power from other base stations.

A good channel estimator performance can thus only be achieved if the estimator takes all types of interference into account. This can be obtained for example by an LMMSE channel estimator. However, it turns out that the resulting matrices that have to be inverted become very large (5120×5120 for a 2×2 MIMO system) [117] prohibiting real-time implementations. Another problem of LMMSE channel estimation is that the autocorrelation matrix of the receive signal (which depends on the autocorrelation matrices of the channel and the noise) is unknown and has to be estimated. Especially in time dispersive MIMO channels, the full autocorrelation matrix becomes huge and very hard to estimate with high accuracy.
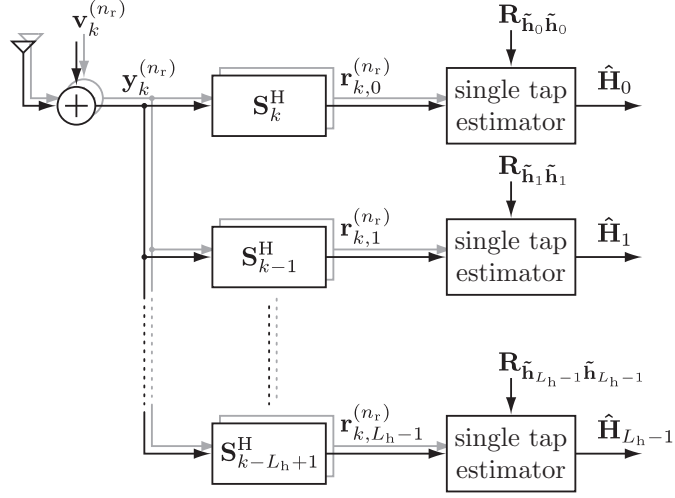
Figure 3.2: Tap-wise LMMSE channel estimator.

Both problems are tackled with the estimator structure illustrated in Figure 3.2. Here, the receive signal is first descrambled by multiplying with conjugated, delayed versions of the scrambling sequence $\mathbf{S}_k$ of the base station. The descrambling operations act as whitening or decorrelation filters. The output signals of the descramblers are thus only spatially correlated and the full autocorrelation matrix can be broken up into several, smaller autocorrelation matrices. This structure allows for estimating the MIMO channel matrix at every delay individually. Hence, this estimator is called the *tap-wise LMMSE channel estimator*.

The derivation of the tap-wise LMMSE channel estimator is based on the system model in Equation (3.6). The receive signal $\mathbf{Y}_k$ in this model is given by

$$\mathbf{Y}_k = \sum_{m=0}^{L_{\mathrm{h}}-1} \Big(\underbrace{\mathbf{S}_{k-m}\left(\mathbf{D}_{k-m} + \mathbf{P}_{k-m}\right)}_{\mathbf{X}_{k-m}} + \mathbf{C}_{k-m} \Big) \tilde{\mathbf{H}}_m + \mathbf{V}_k. \qquad (3.10)$$

Using $\mathbf{S}_{k-n}^{\mathrm{H}}\mathbf{S}_{k-n} = \mathbf{I}$, the signal $\mathbf{R}_{k,n} = \left[\mathbf{r}_{k,n}^{(1)}, \dots, \mathbf{r}_{k,n}^{(N_{\mathrm{R}})} \right]$ after the descrambling operation in the n-th tap $(n = 0, \dots, L_{\mathrm{h}} - 1)$ of Figure 3.2 is given by

$$\mathbf{R}_{k,n} = \mathbf{S}_{k-n}^{\mathrm{H}}\mathbf{Y}_k = \sum_{m=0}^{L_{\mathrm{h}}-1} \mathbf{S}_{k-n}^{\mathrm{H}}\left(\mathbf{S}_{k-m}\left(\mathbf{D}_{k-m} + \mathbf{P}_{k-m}\right) + \mathbf{C}_{k-m}\right)\tilde{\mathbf{H}}_m + \mathbf{S}_{k-n}^{\mathrm{H}}\mathbf{V}_k = \quad (3.11)$$

$$= \mathbf{D}_{k-n}\tilde{\mathbf{H}}_n + \mathbf{P}_{k-n}\tilde{\mathbf{H}}_n + \mathbf{S}_{k-n}^{\mathrm{H}}\left(\mathbf{C}_{k-n}\tilde{\mathbf{H}}_n + \sum_{m\neq n}\left(\mathbf{X}_{k-m} + \mathbf{C}_{k-m}\right)\tilde{\mathbf{H}}_m + \mathbf{V}_k \right).$$

This description can be reformulated by using the vec$(.)$ operator

$$\mathbf{r}_{k,n} = \left[\mathbf{r}_{k,n}^{(1)\mathrm{T}}, \ldots, \mathbf{r}_{k,n}^{(N_\mathrm{R})\mathrm{T}}\right]^\mathrm{T} = \mathrm{vec}\left(\mathbf{R}_{k,n}\right) = \mathrm{vec}\left(\mathbf{S}_{k-n}^\mathrm{H}\mathbf{Y}_k\right) =$$

$$= \underbrace{\left(\mathbf{I}_{N_\mathrm{R}} \otimes \mathbf{P}_{k-n}\right)}_{\mathbf{T}_{k-n}} \underbrace{\mathrm{vec}\left(\tilde{\mathbf{H}}_n\right)}_{\tilde{\mathbf{h}}_n} + \underbrace{\left(\mathbf{I}_{N_\mathrm{R}} \otimes \left(\mathbf{D}_{k-n} + \mathbf{S}_{k-n}^\mathrm{H}\mathbf{C}_{k-n}\right)\right)}_{\tilde{\mathbf{D}}_{k-n}} \underbrace{\mathrm{vec}\left(\tilde{\mathbf{H}}_n\right)}_{\tilde{\mathbf{h}}_n} +$$

$$+ \sum_{m \neq n} \underbrace{\left(\mathbf{I}_{N_\mathrm{R}} \otimes \left(\mathbf{S}_{k-n}^\mathrm{H}\left(\mathbf{X}_{k-m} + \mathbf{C}_{k-m}\right)\right)\right)}_{\tilde{\mathbf{X}}_{k-n,k-m}} \underbrace{\mathrm{vec}\left(\tilde{\mathbf{H}}_m\right)}_{\tilde{\mathbf{h}}_m} +$$

$$+ \underbrace{\left(\mathbf{I}_{N_\mathrm{R}} \otimes \mathbf{S}_{k-n}^\mathrm{H}\right) \mathrm{vec}\left(\mathbf{V}_k\right)}_{\mathbf{w}_k} \tag{3.12}$$

where $\otimes$ denotes the Kronecker product. The LMMSE estimator (refer to Appendix B for a general derivation of LMMSE estimation) of the MIMO channel matrix at time delay n is given by

$$\hat{\mathbf{h}}_n = \mathbf{R}_{\tilde{\mathbf{h}}_n\mathbf{r}}\mathbf{R}_{\mathbf{rr}}^{-1}\mathbf{r}_{k,n}. \tag{3.13}$$

The cross correlation $\mathbf{R}_{\tilde{\mathbf{h}}_n\mathbf{r}}$ in Equation (3.13) is given by

$$\mathbf{R}_{\tilde{\mathbf{h}}_n\mathbf{r}} = \mathbb{E}\left\{\tilde{\mathbf{h}}_n\mathbf{r}_{k,n}^\mathrm{H}\right\} = \mathbb{E}\left\{\tilde{\mathbf{h}}_n\tilde{\mathbf{h}}_n^\mathrm{H}\mathbf{T}_{k-n}^\mathrm{H}\right\} = \mathbf{R}_{\tilde{\mathbf{h}}_n\tilde{\mathbf{h}}_n}\mathbf{T}_{k-n}^\mathrm{H}, \tag{3.14}$$

where the zero mean of the data+control channel chip stream $\mathbb{E}\{\mathbf{D}_{k-n}\} = \mathbf{0}$ and the scrambling sequence $\mathbb{E}\{\mathbf{S}_{k-n}\} = \mathbf{0}$ was used.

Assuming that the time correlation of the channel coefficients is zero between different delays m, that is, $\mathbb{E}\left\{\mathbf{h}_m\mathbf{h}_n^\mathrm{H}\right\} = \mathbf{0}$ for $m \neq n$, the autocorrelation matrix of the receive signal $\mathbf{R}_{\mathbf{rr}}$ is given by

$$\mathbf{R}_{\mathbf{rr}} = \mathbb{E}\left\{\mathbf{r}_{k,n}\mathbf{r}_{k,n}^\mathrm{H}\right\} = \mathbf{T}_{k-n}\mathbf{R}_{\tilde{\mathbf{h}}_n\tilde{\mathbf{h}}_n}\mathbf{T}_{k-n}^\mathrm{H} + \mathbb{E}\left\{\tilde{\mathbf{D}}_{k-n}\tilde{\mathbf{h}}_n\tilde{\mathbf{h}}_n^\mathrm{H}\tilde{\mathbf{D}}_{k-n}^\mathrm{H}\right\} +$$

$$+ \sum_{m \neq n} \mathbb{E}\left\{\tilde{\mathbf{X}}_{k-n,k-m}\mathbf{h}_m\mathbf{h}_m^\mathrm{H}\tilde{\mathbf{X}}_{k-n,k-m}^\mathrm{H}\right\} + \mathbf{R}_{\mathbf{ww}}. \tag{3.15}$$

Equation (3.15) can be simplified using the following lemma.

Lemma 3.1 *Given a matrix* $\mathbf{A}$ *and a vector* $\mathbf{b}$ *with the structure*

$$\mathbf{A} = \begin{bmatrix} a^{(1,1)} & \cdots & a^{(1,N_\mathrm{b})} \\ \vdots & \ddots & \vdots \\ a^{(N_\mathrm{a},1)} & \cdots & a^{(N_\mathrm{a},N_\mathrm{b})} \end{bmatrix}, \quad \mathbf{b} = \begin{bmatrix} b^{(1)} \\ \vdots \\ b^{(N_\mathrm{b})} \end{bmatrix}, \tag{3.16}$$

and assuming that the elements of $\mathbf{A}$ *are uncorrelated and identically distributed with zero mean and variance* σ_a^2, *the elements of* $\mathbf{b}$ *are identically distributed (not necessarily uncorrelated) with zero mean and variance* σ_b^2, *and the elements of* $\mathbf{A}$ *and* $\mathbf{b}$ *are statistically independent, we have*

$$\mathbb{E}\left\{\left(\mathbf{I}_{N_\mathrm{d}} \otimes \mathbf{A}\right) \mathbf{b}\mathbf{b}^\mathrm{H} \left(\mathbf{I}_{N_\mathrm{d}} \otimes \mathbf{A}^\mathrm{H}\right)^\mathrm{H}\right\} = N_\mathrm{b}\sigma_a^2\sigma_b^2\mathbf{I}_{N_\mathrm{a}N_\mathrm{d}}. \tag{3.17}$$

The proof of this expression is carried out by first showing

$$\mathbb{E}\left\{\mathbf{A}\mathbf{b}\mathbf{b}^\mathrm{H}\mathbf{A}^\mathrm{H}\right\} = N_\mathrm{b}\sigma_a^2\sigma_b^2\mathbf{I}_{N_\mathrm{a}} \tag{3.18}$$

which itself can be shown by simple inspection of the matrix-vector multiplication.

Lemma 3.1 can be used to simplify Equation (3.15) if it is assumed that the transmit sequences $\tilde{\mathbf{D}}_k$ and $\tilde{\mathbf{X}}_k$ are spatially and temporally uncorrelated. This, in fact, is only partially fulfilled in the measurements since the synchronization signals $\mathbf{C}_k$ and the control channel signals $\mathbf{B}_k$ are identical at all transmit antennas. However, since only a small fraction of the total transmit power is allocated to $\mathbf{C}_k$ and $\mathbf{B}_k$, this assumption will hold approximately. Furthermore, it has to be assumed that the additive noise-and-interference term $\mathbf{w}_k$ is white with variance σ_w^2. This assumption is always fulfilled due to the descrambling operation that whitens the input signal and thus also the noise-and-interference term. The autocorrelation of the receive signal is thus obtained as

$$\mathbf{R_{rr}} = \mathbf{T}_{k-n}\mathbf{R}_{\mathbf{h}_n\mathbf{h}_n}\mathbf{T}_{k-n}^\mathrm{H} + \underbrace{N_\mathrm{T}\sigma_d^2\sigma_{h_n}^2\mathbf{I}_{N_\mathrm{c}N_\mathrm{R}} + N_\mathrm{T}\sigma_x^2\sum_{m\neq n}\sigma_{h_m}^2\mathbf{I}_{N_\mathrm{c}N_\mathrm{R}} + \sigma_w^2\mathbf{I}_{N_\mathrm{c}N_\mathrm{R}}}_{\approx \sigma_{r_n}^2\mathbf{I}_{N_\mathrm{R}}\otimes\mathbf{I}_{N_\mathrm{c}}}. \tag{3.19}$$

The first term in Equation (3.19) corresponds to the received power of the pilot signals arriving at delay n at the receiver. The three remaining terms in Equation (3.19) almost add up to the total receive power. The difference to the total receive power is only given by the pilot power which is usually low (about $10\,\%$ of the total base station transmit power). These three terms can thus be replaced by a diagonal matrix with an estimate of the received signal power on the main diagonal $\hat{\sigma}_{r_n}^2 = \frac{1}{N_\mathrm{R}L_\mathrm{c}}\|\mathbf{r}_{k,n}\|_2^2$:

$$\mathbf{R_{rr}} \approx \mathbf{T}_{k-n}\mathbf{R}_{\mathbf{h}_n\mathbf{h}_n}\mathbf{T}_{k-n}^\mathrm{H} + \underbrace{\hat{\sigma}_{r_n}^2\mathbf{I}_{N_\mathrm{R}}}_{=\mathbf{R}_{\sigma_{r_n}}}\otimes\mathbf{I}_{N_\mathrm{c}}. \tag{3.20}$$

The first term in Equation (3.20) is composed of the pilot signals and the channel correlation matrix at time delay n. The second term is approximated by the total received signal power. Using such an approximation, the LMMSE estimator for the channel coefficients at delay n is given by

$$\hat{\mathbf{h}}_n = \mathbf{R}_{\tilde{\mathbf{h}}_n \mathbf{r}} \mathbf{R}_{\mathbf{rr}}^{-1} \mathbf{r}_{k,n} = \mathbf{R}_{\tilde{\mathbf{h}}_n \tilde{\mathbf{h}}_n} \mathbf{T}_{k-n}^{\mathrm{H}} \cdot \left(\mathbf{T}_{k-n} \mathbf{R}_{\tilde{\mathbf{h}}_n \tilde{\mathbf{h}}_n} \mathbf{T}_{k-n}^{\mathrm{H}} + \mathbf{R}_{\sigma_r} \otimes \mathbf{I}_{N_c} \right)^{-1} \mathbf{r}_{k,n}. \qquad (3.21)$$

Applying the Woodbury identity [118, 119] for positive definite matrices $\boldsymbol{\Phi}$ and $\boldsymbol{\Omega}$

$$\boldsymbol{\Phi} \boldsymbol{\Theta}^{\mathrm{H}} \left(\boldsymbol{\Theta} \boldsymbol{\Phi} \boldsymbol{\Theta}^{\mathrm{H}} + \boldsymbol{\Omega} \right)^{-1} = \left(\boldsymbol{\Phi}^{-1} + \boldsymbol{\Theta}^{\mathrm{H}} \boldsymbol{\Omega}^{-1} \boldsymbol{\Theta} \right)^{-1} \boldsymbol{\Theta}^{\mathrm{H}} \boldsymbol{\Omega}^{-1}, \qquad (3.22)$$

the definition $\mathbf{T}_{k-n} = \mathbf{I}_{N_{\mathrm{R}}} \otimes \mathbf{P}_{k-n}$ from Equation (3.12) in a second step, and the relation $(\mathbf{A} \otimes \mathbf{B})(\mathbf{C} \otimes \mathbf{D}) = \mathbf{AC} \otimes \mathbf{BD}$ in a third step, the LMMSE estimator can be reformulated to

$$\begin{aligned}
\hat{\mathbf{h}}_n &= \left[\mathbf{R}_{\tilde{\mathbf{h}}_n \tilde{\mathbf{h}}_n}^{-1} + \mathbf{T}_{k-n}^{\mathrm{H}} \left(\mathbf{R}_{\sigma_r}^{-1} \otimes \mathbf{I}_{N_c} \right) \mathbf{T}_{k-n} \right]^{-1} \mathbf{T}_{k-n}^{\mathrm{H}} \left(\mathbf{R}_{\sigma_r}^{-1} \otimes \mathbf{I}_{N_c} \right) \mathbf{r}_{k,n} = \\
&= \left[\mathbf{R}_{\tilde{\mathbf{h}}_n \tilde{\mathbf{h}}_n}^{-1} + \left(\mathbf{I}_{N_{\mathrm{R}}} \otimes \mathbf{P}_{k-n}^{\mathrm{H}} \right) \left(\mathbf{R}_{\sigma_r}^{-1} \otimes \mathbf{I}_{N_c} \right) \left(\mathbf{I}_{N_{\mathrm{R}}} \otimes \mathbf{P}_{k-n} \right) \right]^{-1} \cdot \\
&\qquad\qquad \cdot \left(\mathbf{I}_{N_{\mathrm{R}}} \otimes \mathbf{P}_{k-n}^{\mathrm{H}} \right) \left(\mathbf{R}_{\sigma_r}^{-1} \otimes \mathbf{I}_{N_{\mathrm{T}}} \right) \mathbf{r}_{k,n} = \\
&= \left[\mathbf{R}_{\tilde{\mathbf{h}}_k \tilde{\mathbf{h}}_k}^{-1} + \left(\mathbf{R}_{\sigma_r}^{-1} \otimes \mathbf{P}_{k-n}^{\mathrm{H}} \mathbf{P}_{k-n} \right) \right]^{-1} \left(\mathbf{R}_{\sigma_r}^{-1} \otimes \mathbf{P}_{k-n}^{\mathrm{H}} \right) \mathbf{r}_{k,n}. \qquad (3.23)
\end{aligned}$$

This LMMSE estimator requires the knowledge of the channel autocorrelation matrix $\mathbf{R}_{\tilde{\mathbf{h}}_n \tilde{\mathbf{h}}_n}$ which is usually not known. Therefore, a so-called "instantaneous" estimate of $\mathbf{R}_{\tilde{\mathbf{h}}_n \tilde{\mathbf{h}}_n}$ is utilized. This instantaneous estimate is obtained similarly as in the approach for OFDM channel estimation presented in [27] and Section 2.3.1.

Instantaneous channel autocorrelation estimation

The LMMSE channel estimator using the instantaneous channel auto-correlation can be described by the following three-stage process:

1. Perform a low complexity, correlation-based channel estimation

$$\hat{\mathbf{h}}_k^{(\mathrm{cor})} = \frac{1}{\|\mathbf{p}\|_2^2} \left(\mathbf{I}_{N_{\mathrm{R}}} \otimes \mathbf{P}_{k-n}^{\mathrm{H}} \right) \mathbf{r}_{k,n} \qquad (3.24)$$

with $\|\mathbf{p}\|_2^2 = \|\mathbf{p}^{(n_{\mathrm{t}})}\|_2^2$ (assuming that the pilot power is equally distributed over the transmit antennas).

2. Calculate the channel gains, and assume them to be spatially uncorrelated. Here, we use the notation $(.)_l$ for denoting the l-th element of a vector.

$$\hat{\mathbf{R}}_{\tilde{\mathbf{h}}_n \tilde{\mathbf{h}}_n}^{-1} = \text{diag}\left(\frac{1}{|(\hat{\mathbf{h}}_n^{(\text{cor})})_l|^2}\right) \quad ; l = 1, \dots, N_{\text{R}}N_{\text{T}}. \tag{3.25}$$

3. Use the estimate of $\mathbf{R}_{\tilde{\mathbf{h}}_n \tilde{\mathbf{h}}_n}^{-1}$ in Equation (3.23) to improve the correlation-based channel estimate

$$\hat{\mathbf{h}}_n^{(\text{LMMSE})} = \left[\hat{\mathbf{R}}_{\tilde{\mathbf{h}}_n \tilde{\mathbf{h}}_n}^{-1} + \mathbf{R}_{\sigma_r}^{-1} \otimes \left(\mathbf{P}_{k-n}^{\text{H}} \mathbf{P}_{k-n}\right)\right]^{-1} \|\mathbf{p}\|^2 \left(\mathbf{R}_{\sigma_r}^{-1} \otimes \mathbf{I}_{N_{\text{T}}}\right) \hat{\mathbf{h}}_n^{(\text{cor})}. \tag{3.26}$$

At the cost of higher complexity, the LMMSE channel estimate obtained in Step 3 can be used to improve the estimate of the channel autocorrelation matrix $\hat{\mathbf{R}}_{\tilde{\mathbf{h}}_n \tilde{\mathbf{h}}_n}$ in Step 2. It was found that more than three iterations do not yield a significant performance increase anymore. Therefore, in the measurements the iterative tap-wise LMMSE channel estimator structure was used with three iterations.

Complexity Considerations

The computational complexity of the tap-wise LMMSE channel estimator with instantaneous autocorrelation estimation is slightly higher than that of the LS channel estimator. The first step of both estimators—the calculation of the correlation-based channel estimate in Equation (3.24)—is exactly the same [50]. The calculation of the actual channel estimate requires N_{R} matrix inverses of dimension $N_{\text{T}} \times N_{\text{T}}$ for every channel tap. The increased complexity of the tap-wise LMMSE channel estimator basically comes from the multiple descrambling operations and the estimation of the channel autocorrelation matrix like, for example, in Equation (3.25). If the iterative channel estimator is used, the complexity obviously increases linearly with the number of iterations.

3.3.2. Equalizer

After the channel estimation, as explained in Section 3.3.1, the interference of the deterministic signals, that is, the pilot channels $\mathbf{p}_k$ and synchronization channels $\mathbf{c}_k$, and the interference of the control channels $\mathbf{b}_k$ is canceled. Since the control channels are transmitted with a large spreading factor of 256, error-free reception is assumed. If furthermore perfect channel knowledge and thus perfect cancelation is assumed, the system model in Equation (3.9) is simplified to

$$\mathbf{y}_k = \mathbf{H} \left(\mathbf{I}_{N_\mathrm{T}} \otimes \mathbf{S}_k \right) \left(\mathbf{W} \otimes \mathbf{I}_{L_\mathrm{c}} \right) \mathbf{a}_k + \mathbf{v}_k. \tag{3.27}$$

Note that without interference cancelation (at least of the synchronization channel) the post equalization SINR would saturate at about 20 dB. CQI values requiring higher SINR can thus not be selected leading to a saturation of the throughput [120–122]. Alternatively to interference cancelation, interference aware equalization is possible and was shown to achieve high performance [123–126].

Since the precoding and the scrambling are both linear operations, their order in Equation (3.27) can be exchanged to obtain

$$\mathbf{y}_k = \mathbf{H} \left(\mathbf{W} \otimes \mathbf{I}_{L_\mathrm{c}} \right) \underbrace{\left(\mathbf{I}_{N_\mathrm{s}} \otimes \mathbf{S}_k \right) \mathbf{a}_k}_{\tilde{\mathbf{a}}_k} + \mathbf{v}_k = \mathbf{H} \left(\mathbf{W} \otimes \mathbf{I}_{L_\mathrm{c}} \right) \tilde{\mathbf{a}}_k + \mathbf{v}_k. \tag{3.28}$$

Using this system model, the equalizer coefficients for the reconstruction of the n_s-th transmitted chip sequence can be calculated by minimizing the quadratic cost function [127, 128]

$$J \left(\mathbf{f}^{(n_\mathrm{s})} \right) = \mathbb{E} \left\{ \left| \mathbf{f}^{(n_\mathrm{s})\mathrm{H}} \mathbf{y}_k - \tilde{a}_{k-\tau}^{(n_\mathrm{s})} \right|^2 \right\}, \tag{3.29}$$

where $\mathbf{f}^{(n_\mathrm{s})}$ is given by a stacked vector of N_R equalization filters

$$\mathbf{f}^{(n_\mathrm{s})} = \left[\mathbf{f}^{(1,n_\mathrm{s})\mathrm{T}}, \dots, \mathbf{f}^{(N_\mathrm{R}, n_\mathrm{s})\mathrm{T}} \right]^\mathrm{T}, \tag{3.30}$$

each of length L_f

$$\mathbf{f}^{(n_\mathrm{r}, n_\mathrm{s})} = \left[f_0^{(n_\mathrm{r}, n_\mathrm{s})}, \dots, f_{L_f - 1}^{(n_\mathrm{r}, n_\mathrm{s})} \right]^\mathrm{T}. \tag{3.31}$$

Setting the derivative of the cost function (Equation (3.29)) with respect to $\mathbf{f}^{(n_\mathrm{s})*}$ equal to zero

$$\frac{\partial J}{\partial \mathbf{f}^{(n_\mathrm{s})*}} = \left(\sigma_a^2 \mathbf{H} \left(\mathbf{W} \mathbf{W}^\mathrm{H} \otimes \mathbf{I}_{L_\mathrm{c}} \right) \mathbf{H}^\mathrm{H} + \sigma_a^2 \mathbf{I}_{N_\mathrm{R} L_\mathrm{c}} \right) \mathbf{f}^{(n_t)} - \sigma_s^2 \mathbf{H} \left(\mathbf{W} \otimes \mathbf{I}_{L_\mathrm{c}} \right) \mathbf{e}_{\tau + (n_\mathrm{s} - 1)L_\mathrm{c}} = 0 \tag{3.32}$$

yields the equalizer coefficients for the n_s-th transmitted chip sequence

$$\mathbf{f}^{(n_\text{s})} = \left(\mathbf{H} \left(\mathbf{W}\mathbf{W}^\text{H} \otimes \mathbf{I}_{L_\text{c}} \right) \mathbf{H}^\text{H} + \frac{\sigma_v^2}{\sigma_a^2} \mathbf{I}_{N_\text{R}L_\text{c}} \right)^{-1} \cdot \mathbf{H} \left(\mathbf{W} \otimes \mathbf{I}_{L_\text{c}} \right) \mathbf{e}_{\tau+(n_\text{s}-1)L_\text{c}}. \tag{3.33}$$

Here, $\mathbf{e}_{\tau+(n_\text{s}-1)L_\text{c}}$ denotes a unit vector with a single "one" at cursor position $(\tau + (n_\text{s} - 1)L_\text{c})$ and "zeros" at all other positions. The calculation of the equalizer coefficients can be implemented efficiently using FFT-based algorithms like [129, 130], the conjugated gradient algorithm [131], or other iterative algorithms like for example [132]. This receiver thus represents a low complexity HSDPA receiver that is feasible for real-time implementation in a chip [133].

3.3.3. Further Receiver Processing

The output chip stream of the equalizer is descrambled, despread, soft-demapped and soft-decoded in a Turbo decoder using eight iterations. Finally, the Cyclic redundancy check (CRC) bytes of the resulting data block are verified. If the CRC yields "false", a maximum of two HARQ retransmissions are performed. If these retransmissions also fail, the data block is considered as lost. Note that in the actual testbed implementation (see Section A.2.1), the two retransmissions are always carried out. The number of retransmissions required for a correct reception is determined in the data evaluation after the measurement.

3.4. Quantized Precoding

The precoding matrix defined in Equation (3.2) is strongly quantized and chosen from a predefined codebook in HSDPA systems [112]. For single antenna transmissions, in which obviously no spatial precoding can be performed, the precoding matrix $\mathbf{W}$ is reduced to a scalar equal to "one"

$$\mathbf{W}^{(\text{SISO})} = 1. \tag{3.34}$$

For multiple antenna transmissions, the precoding matrices are composed of the scalars

$$w_0 = \frac{1}{\sqrt{2}} \tag{3.35}$$

and

$$w_1, w_2 \in \left\{ \frac{1+\text{j}}{2}, \frac{1-\text{j}}{2}, \frac{-1+\text{j}}{2}, \frac{-1-\text{j}}{2} \right\}. \tag{3.36}$$

The Transmit Antenna Array (TxAA) transmission mode utilizes two antennas to transmit a single stream. In this mode, the precoding matrix is defined as

$$\mathbf{W}^{(\text{TxAA})} = \begin{bmatrix} w_0 \\ w_1 \end{bmatrix}. \tag{3.37}$$

This means that the signal at the first antenna is always weighted by the same scalar constant w_0, whereas the signal at the second antenna is weighted by w_1 which is chosen in order to maximize the received post equalization SINR [49]. In TxAA, the number of possible precoding matrices is equal to four, corresponding to an amount of 2 bit feedback.

In case of a Double Transmit Antenna Array (D-TxAA) transmission, the precoding matrix is given by

$$\mathbf{W}^{(\text{D}-\text{TxAA})} = \begin{bmatrix} w_0 & w_0 \\ w_1 & -w_1 \end{bmatrix}. \tag{3.38}$$

Note that this precoding matrix is a unitary matrix; that is, the precoding vector of the second stream is always chosen orthogonal to the one of the first stream. Although D-TxAA defines four precoding matrices, only the first two of them cause different SINRs at the receiver. In the other two cases, the SINRs of the first and the second stream are exchanged. Since the data rates of both streams can be adjusted individually, the third and the fourth precoding matrices are redundant. Note also, if the user experiences a low channel quality in D-TxAA, only a single stream is transmitted; that is, the precoding matrix in Equation (3.37) is applied to the data streams at the transmitter. Thus, in TxAA always a single stream is transmitted and in D-TxAA either single-stream or double-stream transmission—whichever is better—is performed.

The HSDPA standard does not define spatial precoding for four transmit antennas. The benefits of four transmit antennas in HSDPA are explored with a very simple extension of the existing precoding vectors. The precoding matrix for double-stream four transmit antenna transmission is defined as

$$\mathbf{W}^{(4\text{Tx}-\text{D}-\text{TxAA})} = \begin{bmatrix} w_0 & 0 \\ 0 & w_0 \\ w_1 & 0 \\ 0 & w_2 \end{bmatrix}. \tag{3.39}$$

In contrast to the two antenna D-TxAA system, the four antenna D-TxAA system now transmits the two data streams on individual antenna pairs. Also, the precoding of both streams is individually adjusted allowing 16 possible precoding matrices.

3.5. CQI and PCI Calculation

In this section, analytic expressions for the post equalization interference terms are derived. These expressions can be used to determine the total post equalization SINR for every possible PCI value. The estimated SINR values can be furthermore mapped to CQI values that correspond to specific Transport Block Sizes (TBSs). The TBS defines the number of data bits to be transmitted within one subframe. Maximizing the TBS of successfully transmitted data blocks over the different PCI values thus maximizes the data throughput [49].

Since the true channel matrix $\mathbf{H}$ is unknown at the receiver, a very important aspect when estimating the post equalization SINR is the modeling of the channel estimation error. The true channel matrix is thus approximated by the estimated channel matrix $\hat{\mathbf{H}}$ and a matrix $\mathbf{H}_\Delta$ representing the channel estimation error [134]. The matrix $\mathbf{H}_\Delta$ is constructed like the channel matrix $\mathbf{H}$ in Equations (3.7) and (3.8). The non-zero elements of $\mathbf{H}_\Delta$ are assumed to be i.i.d. Gaussian with a variance equal to the MSE of the channel estimator.

The SINR expressions derived in this section are verified by simulations and measurements and can be used not only for implementing the feedback on the physical layer but also for modeling the physical layer in system level HSDPA simulations [60–63, 135].

3.5.1. HS-PDSCH Interference

The High Speed Physical Downlink Shared Channel (HS-PDSCH) consists of the data chip streams in $\mathbf{a}_k$. These code division multiplexed data chip streams generate inter-code interference due to non perfect equalization at the receiver. The residual interference can be assessed by looking at the total impulse response seen by all scrambled data chip streams in $(\mathbf{I}_{N_\mathrm{s}} \otimes \mathbf{S}_k)\, \mathbf{a}_k$ to the output of the n_s-th equalization filter

$$\mathbf{h}_{\mathrm{eff},a}^{(n_\mathrm{s})\mathrm{T}} = \mathbf{f}^{(n_\mathrm{s})\mathrm{H}} \left(\hat{\mathbf{H}} + \mathbf{H}_\Delta \right) \left(\mathbf{W} \otimes \mathbf{I}_{L_c} \right). \tag{3.40}$$

The interference power at the output of the equalizer can be divided into a deterministic part (caused by $\hat{\mathbf{H}}$) and a stochastic part (caused by $\mathbf{H}_\Delta$). The deterministic interference can be canceled by a decision feedback equalizer [56], whereas the stochastic interference can only be decreased by reducing the MSE of the channel estimator. As will be shown in Section 3.5.5, however, the cancelation of the data channels alone does not yield a significant performance gain.

The deterministic HS-PDSCH interference power is calculated by accumulating the energies of the total impulse response at delays $m \neq \tau$. The remaining interference at delay τ (the

chosen delay of the transmitted chip stream after the channel and the equalizer) is irrelevant since it is perfectly removed by the despreading operation

$$\gamma_{a,\hat{\mathbf{H}}}^{(n_s)} = \frac{P_{\text{HS-PDSCH}}}{N_s} \cdot \sum_{\substack{m=1 \\ m \neq \tau}}^{L_c} \left| \left(\mathbf{f}^{(n_s)\text{T}} \hat{\mathbf{H}} \left(\mathbf{W} \otimes \mathbf{I}_{L_c} \right) \right)_m \right|^2. \qquad (3.41)$$

Here, $P_{\text{HS-PDSCH}}$ corresponds to the transmit power available for all N_s data chip streams. The operator $(.)_m$ denotes the m-th element of a vector.

The stochastic HS-PDSCH interference power is obtained by building the expectation with respect to the unknown channel estimation error

$$\gamma_{s,\mathbf{H}_\Delta}^{(n_s)} = \frac{P_{\text{HS-PDSCH}}}{N_s} \cdot \mathbb{E}_{\mathbf{H}_\Delta} \left\{ \sum_{\substack{m=1 \\ m \neq \tau}}^{L_c} \left| \left(\mathbf{f}^{(n_s)\text{T}} \mathbf{H}_\Delta \left(\mathbf{W} \otimes \mathbf{I}_{L_c} \right) \right)_m \right|^2 \right\} \approx$$

$$\approx \frac{P_{\text{HS-PDSCH}}}{N_s} \cdot \text{MSE} \cdot (L_h - 1) \, N_T \left\| \mathbf{f}^{(n_s)} \right\|_2^2. \qquad (3.42)$$

In this derivation, the last step can be verified by a careful inspection of the matrix-vector multiplications. As shown later in Figure 3.5, the approximation in Equation (3.42) only has a negligible impact on the accuracy of the SINR estimator. The same holds true for similar approximations of the stochastic interference in the next sections.

3.5.2. Pilot Interference

The total impulse response as it is experienced by the scrambled Common Pilot Channels (CPICHs) $(\mathbf{I}_{N_T} \otimes \mathbf{S}_k) \, \mathbf{p}_k$ from the transmit antennas to the output of the n_s-th equalization filter is given by the $N_T L_c$ length vector

$$\mathbf{h}_{\text{eff},p}^{(n_s)\text{T}} = \mathbf{f}^{(n_s)\text{T}} \mathbf{H} = \mathbf{f}^{(n_s)\text{T}} \left(\hat{\mathbf{H}} + \mathbf{H}_\Delta \right). \qquad (3.43)$$

Again, we can identify a deterministic interference

$$\gamma_{p,\hat{\mathbf{H}}}^{(n_s)} = \frac{P_{\text{CPICH}}}{N_T} \cdot \sum_{n_t=1}^{N_T} \sum_{\substack{m=1 \\ m \neq \tau}}^{L_c} \left| \left(\mathbf{f}^{(n_s)\text{T}} \hat{\mathbf{H}} \right)_{m+(n_t-1)L_c} \right|^2 \qquad (3.44)$$

and a stochastic interference

$$\gamma_{p,\mathbf{H}_\Delta}^{(n_\mathrm{s})} = \frac{P_\mathrm{CPICH}}{N_\mathrm{T}} \cdot \mathbb{E}_{\mathbf{H}_\Delta}\left\{ \sum_{n_\mathrm{t}=1}^{N_\mathrm{T}} \sum_{\substack{m=1 \\ m \neq \tau}}^{L_\mathrm{c}} \left| \left(\mathbf{f}^{(n_\mathrm{s})\mathrm{T}} \mathbf{H}_\Delta \right)_{m+(n_\mathrm{t}-1)L_\mathrm{c}} \right|^2 \right\} \approx$$

$$\approx \frac{P_\mathrm{CPICH}}{N_\mathrm{T}} \cdot \mathrm{MSE} \cdot (L_\mathrm{h} - 1) \left\| \mathbf{f}^{(n_\mathrm{s})} \right\|_2^2. \tag{3.45}$$

Here, P_CPICH denotes the total pilot channel power for all transmit antennas.

3.5.3. Synchronization and Control Channels Interference

For the calculation of the interference emerging from the synchronization and control channels it is assumed that these channels are transmitted on all antennas simultaneously, that is, the power is equally distributed on all transmit antennas. Since the Synchronization Channel (SCH) and the Primary Common Control Physical Channel (PCCPCH) are transmitted time multiplexed, it is furthermore assumed that both channels have equal power, that is, $P_\mathrm{SCH} = P_\mathrm{CCPCH}$. The total impulse response of the synchronization channels $\mathbf{c}_k$ and the scrambled control channels $(\mathbf{I}_{N_\mathrm{T}} \otimes \mathbf{S}_k)\, \mathbf{b}_k$ to the output of the n_s-th equalization filter is given by

$$\mathbf{h}_{\mathrm{eff},\mathrm{SCH}}^{(n_\mathrm{s})\mathrm{T}} = \frac{1}{\sqrt{N_\mathrm{T}}} \mathbf{f}^{(n_\mathrm{s})\mathrm{T}} \left(\hat{\mathbf{H}} + \mathbf{H}_\Delta \right) \left(\mathbf{1}_{N_\mathrm{T}} \otimes \mathbf{I}_{L_\mathrm{c}} \right). \tag{3.46}$$

Here, $\mathbf{1}_{N_\mathrm{T}}$ denotes an $N_\mathrm{T} \times 1$ dimensional vector with all entries equal to one. Note that the multiplication with $(\mathbf{1}_{N_\mathrm{T}} \otimes \mathbf{I}_{L_\mathrm{c}})$ represents the summation of the individual transmit antenna impulse responses. This is required because of the previous assumption that synchronization and control channels are transmitted on all antennas simultaneously. The deterministic part of the interference is calculated as

$$\gamma_{\mathrm{SCH},\hat{\mathbf{H}}}^{(n_\mathrm{s})} = \frac{P_\mathrm{SCH}}{N_\mathrm{T}} \cdot \sum_{\substack{m=1 \\ m \neq \tau}}^{L_\mathrm{c}} \left| \left(\mathbf{f}^{(n_\mathrm{s})\mathrm{T}} \hat{\mathbf{H}} \left(\mathbf{1}_{N_\mathrm{T}} \otimes \mathbf{I}_{L_\mathrm{c}} \right) \right)_m \right|^2 \tag{3.47}$$

and the stochastic interference as

$$\gamma_{\mathrm{SCH},\mathbf{H}_\Delta}^{(n_\mathrm{s})} = \frac{P_\mathrm{SCH}}{N_\mathrm{T}} \cdot \mathbb{E}_{\mathbf{H}_\Delta}\left\{ \sum_{\substack{m=1 \\ m \neq \tau}}^{L_\mathrm{c}} \left| \left(\mathbf{f}^{(n_\mathrm{s})\mathrm{T}} \mathbf{H}_\Delta \left(\mathbf{1}_{N_\mathrm{T}} \otimes \mathbf{I}_{L_\mathrm{c}} \right) \right)_m \right|^2 \right\} \approx$$

$$\approx \frac{P_\mathrm{SCH}}{N_\mathrm{T}} \cdot \mathrm{MSE} \cdot (L_\mathrm{h} - 1) \left\| \mathbf{f}^{(n_\mathrm{s})} \right\|_2^2. \tag{3.48}$$

Additionally to the two interference terms above, interference at delay lag $m = \tau$ emerges from the SCH since it is transmitted without spreading and scrambling and is thus not orthogonal to the data channels

$$
\gamma^{(n_{\mathrm{s}})}_{\mathrm{SCH},\hat{\mathbf{H}},\tau} = \frac{\gamma P_{\mathrm{SCH}}}{N_{\mathrm{T}}} \left| \left(\mathbf{f}^{(n_{\mathrm{s}})\mathrm{T}} \hat{\mathbf{H}} \left(\mathbf{1}_{N_{\mathrm{T}}} \otimes \mathbf{I}_{L_{\mathrm{c}}} \right) \right)_{\tau} \right|^2 ,
\tag{3.49}
$$

$$
\gamma^{(n_{\mathrm{s}})}_{\mathrm{SCH},\mathbf{H}_{\Delta},\tau} = \frac{\gamma P_{\mathrm{SCH}}}{N_{\mathrm{T}}} \mathbb{E}_{\mathbf{H}_{\Delta}} \left\{ \left| \left(\mathbf{f}^{(n_{\mathrm{s}})\mathrm{T}} \mathbf{H}_{\Delta} \right)_{\tau} \right|^2 \right\} =
$$

$$
= \frac{\gamma P_{\mathrm{SCH}}}{N_{\mathrm{T}}} \cdot \mathrm{MSE} \cdot \sum_{n_{\mathrm{r}}=1}^{N_{\mathrm{R}}} \sum_{m=1}^{L_{\mathrm{h}}} \left| \left(\mathbf{f}^{(n_{\mathrm{s}})} \right)_{m+\tau-L_{\mathrm{h}}+(n_{\mathrm{r}}-1)L_{\mathrm{f}}} \right|^2 .
\tag{3.50}
$$

The constant factor $\gamma = 0.1$ originates from the time-multiplexing of the SCH and the PCCPCH since the SCH occupies only the first 10% of all chips in every transmitted slot. Note that the PCCPCH does not contribute to the interference terms in Equations (3.49) and (3.50) since it is transmitted with spreading.

3.5.4. Post Equalization Noise

According to the system model in Equation (3.9), the variance of the post equalization noise at the output of the n_{s}-th equalization filter is given by

$$
\sigma_{v\prime}^{(n_{\mathrm{s}})2} = \| \mathbf{f}^{(n_{\mathrm{s}})} \|_2^2 \sigma_v^2 .
\tag{3.51}
$$

Note that in this expression it is implicitly assumed that the noise $\mathbf{v}_k$ is white with variance σ_v^2. Given the correlation of the signals received from interfering base stations, it is straightforward to include colored inter-cell interference into the post equalization noise. Since in the measurements only a single base station is considered, however, it is not required here.

3.5.5. Post Equalization SINR

The total deterministic interference caused by the pilot, control, and synchronization channels is given by

$$\gamma_{\hat{\mathbf{H}}}^{(n_\mathrm{s})} = \gamma_{p,\hat{\mathbf{H}}}^{(n_\mathrm{s})} + \gamma_{\mathrm{SCH},\hat{\mathbf{H}}}^{(n_\mathrm{s})} + \gamma_{\mathrm{SCH},\hat{\mathbf{H}},\tau}^{(n_\mathrm{s})}. \tag{3.52}$$

Analogously, the stochastic interference is calculated by

$$\gamma_{\mathbf{H}_\Delta}^{(n_\mathrm{s})} = \gamma_{p,\mathbf{H}_\Delta}^{(n_\mathrm{s})} + \gamma_{\mathrm{SCH},\mathbf{H}_\Delta}^{(n_\mathrm{s})} + \gamma_{\mathrm{SCH},\mathbf{H}_\Delta,\tau}^{(n_\mathrm{s})}. \tag{3.53}$$

Knowing all the above interference terms, the post equalization SINR [61, 135] of the n_s-th data stream at the despreader output can be calculated as

$$\mathrm{SINR_{est}}^{(n_\mathrm{s})} = \frac{\mathrm{SF}\left|\left(\mathbf{h}_{\mathrm{eff},a}^{(n_\mathrm{s})}\right)_\tau\right|^2 \frac{P_{\mathrm{HS-PDSCH}}}{N_\mathrm{s}}}{\gamma_{a,\hat{\mathbf{H}}}^{(n_\mathrm{s})} + C\gamma_{\hat{\mathbf{H}}}^{(n_\mathrm{s})} + \gamma_{a,\mathbf{H}_\Delta}^{(n_\mathrm{s})} + \gamma_{\mathbf{H}_\Delta}^{(n_\mathrm{s})} + \sigma_{v\prime}^{(n_\mathrm{s})2}}. \tag{3.54}$$

Here, SF is the spreading factor of the HS-PDSCH (SF = 16 for HSDPA). The factor C is equal to 0 if the receiver uses interference cancelation of the synchronization, pilot, and control channels and equal to 1 if no interference cancelation is employed.

In Figure 3.3, the individual post equalization interference terms of a 2×2 TxAA system are shown over $I_{\mathrm{or}}/I_{\mathrm{oc}}$ (serving base station to interfering base stations power ratio). Below $I_{\mathrm{or}}/I_{\mathrm{oc}} \approx 10\,\mathrm{dB}$, the system performance is mainly dominated by the post equalization noise. Above $I_{\mathrm{or}}/I_{\mathrm{oc}} > 10\,\mathrm{dB}$, the deterministic interference caused by the pilot and the synchronization channel becomes dominant and has to be canceled to achieve high performance. If interference cancelation is performed, the system performance at high $I_{\mathrm{or}}/I_{\mathrm{oc}} > 10$ is mainly dominated by the channel estimation error. Over the whole $I_{\mathrm{or}}/I_{\mathrm{oc}}$ range, the inter-code interference of the data channels, given by $\gamma_{a,\hat{\mathbf{H}}}^{(n_\mathrm{s})}$, is more than one magnitude smaller than the post equalization noise. Therefore, interference cancelation of the data channels does not yield additional performance gains.
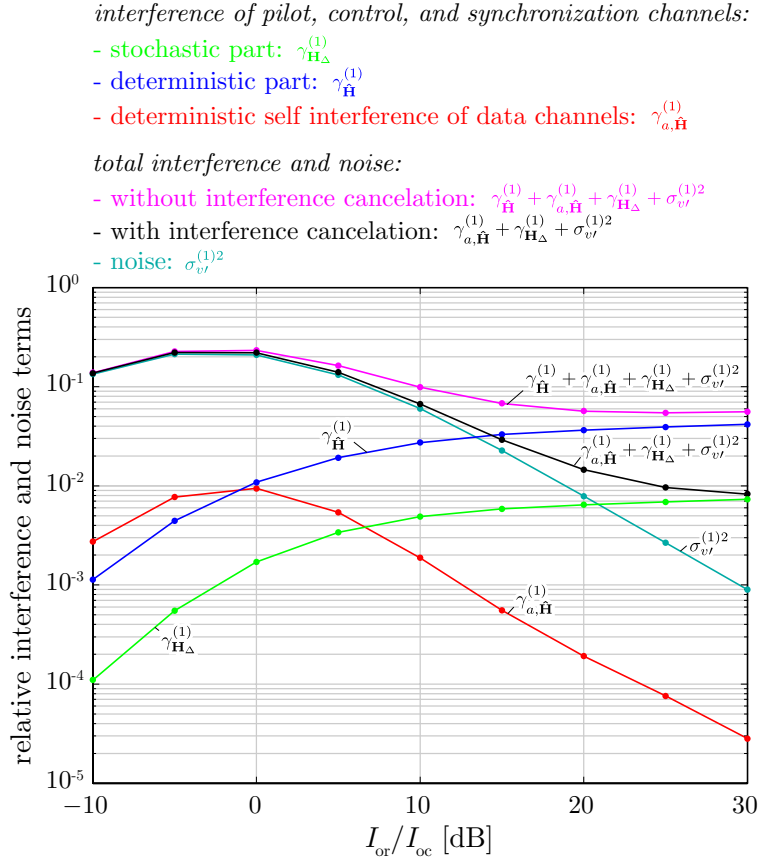
interference of pilot, control, and synchronization channels:
- stochastic part: $\gamma_{\mathbf{H}_\Delta}^{(1)}$
- deterministic part: $\gamma_{\hat{\mathbf{H}}}^{(1)}$
- deterministic self interference of data channels: $\gamma_{a,\hat{\mathbf{H}}}^{(1)}$

total interference and noise:
- without interference cancelation: $\gamma_{\hat{\mathbf{H}}}^{(1)} + \gamma_{a,\hat{\mathbf{H}}}^{(1)} + \gamma_{\mathbf{H}_\Delta}^{(1)} + \sigma_{v\prime}^{(1)2}$
- with interference cancelation: $\gamma_{a,\hat{\mathbf{H}}}^{(1)} + \gamma_{\mathbf{H}_\Delta}^{(1)} + \sigma_{v\prime}^{(1)2}$
- noise: $\sigma_{v\prime}^{(1)2}$

Figure 3.3: Interference terms for a two receive antennas TxAA transmission simulated using an uncorrelated ITU Pedestrian B channel model [136].

Figures 3.4 and 3.5 show the estimated SINR and an "observed SINR" for a simulation with perfect channel knowledge and a measurement with channel estimation employed. The "observed SINR" is monitored at the demapper input and is obtained as follows: Consider the transmitted data symbol vector $\mathbf{u}^{(n_s)}$ of the n_s-th symbol stream and the corresponding received symbol vector at the demapper input $\hat{\mathbf{u}}^{(n_s)}$. The "observed" or "true" post equalization SINR is given by

$$\text{SINR} = \frac{\|\mathbf{u}^{(n_s)}\|_2^2}{\|\hat{\mathbf{u}}^{(n_s)} - \mathbf{u}^{(n_s)}\|_2^2}. \tag{3.55}$$

In the simulations, a very good fit of the estimated SINRs (calculated according to Equation (3.54)) over the full $I_{\text{or}}/I_{\text{oc}}$ (ratio of the energy of the desired base station to the energy of the interfering base stations) range is observed. The SINR increases linearly with increasing $I_{\text{or}}/I_{\text{oc}}$. The estimated SINRs in the measurements also show a good fit at all transmit powers. In contrast to the simulations, the SINR saturates at about 30 dB which is caused by residual interference due to the channel estimation error (which is the dominating factor at high SINR, as shown in Figure 3.3).
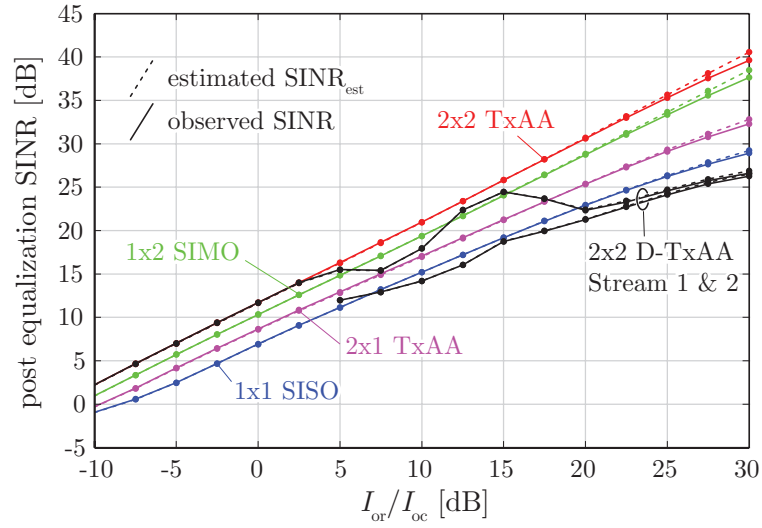
Figure 3.4: Estimated and observed SINR for perfect channel knowledge, simulated using an uncorrelated ITU Pedestrian B channel model [136].
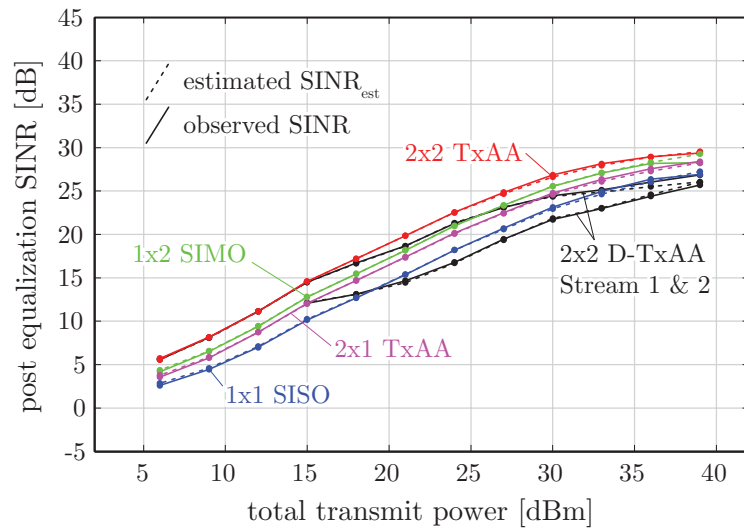

Figure 3.5: Estimated and observed SINR with iterative tap-wise LMMSE channel estimation, measured in the alpine scenario (see Section A.1).

3.5.6. SINR to CQI Mapping

Once the SINR is estimated at the receiver, it can be mapped to a CQI value. This is achieved following Table 3.1 for single-stream mode and Table 3.2 for double-stream mode. The SINR-to-CQI mapping tables were obtained by simulating the Block Error Ratio (BLER) performance of a Category 16 UE for all CQI values in an AWGN channel. The SINR values in the table are equal to the AWGN SNRs at 10 % BLER values, as suggested as maximum BLER by the HSDPA standard [112, Section 6A.2]. The mapping is performed as follows. The estimated SINR minus a 1 dB margin (to account for SINR estimation errors) is compared to the SINR values in the tables and the maximum CQI that supports transmission with 10 % BLER is selected. Since this step involves a rounding operation, the actually measured BLER can be expected to be smaller than 10 %.

The CQI values obtained from the mapping tables correspond to TBSs defined in [112, Table 7D, pp. 50] for single-stream mode and in [112, Table 7I, pp. 54] for double-stream mode. The maximum TBS in single-stream mode is 25 558 bits that are transmitted in one subframe of length 2 ms. Thus, the maximum data rate of the Category 16 UE in single-stream mode is 12.779 Mbit/s. In double-stream mode, the maximum TBS of one stream is equal to 27 952 bits allowing for a maximum data rate of 27.952 Mbit/s.

Similar CQI mapping tables as Tables 3.1 and 3.2 are available in documents of the Radio Access Network (RAN) Work Group 1, for example [137]. However, a comparison is difficult since the simulation results in the RAN documents were generated usually before the standard was finalized. Therefore, every company used different coding rates and/or number of spreading codes in the simulations. For example, in [137] the authors used 15 spreading codes for all coding rates. Nevertheless, Table 3.1 can be compared at the four largest CQI values (since only these use also 15 spreading codes) to the second table in the appendix of [137]. Since [137] gives symbol SNR values in the tables, an offset of $10 \log_{10}(15)$ dB to the SINR values given in Table 3.1 is present. Besides this offset, the values in Table 3.1 are the same as the values in [137] within a few tenth of a decibel.

CQI	1	2	3	4	5	6	7	8
SINR	-3.5 dB	-2.6 dB	-1.5 dB	-0.3 dB	0.5 dB	1.7 dB	2.5 dB	3.5 dB
CQI	9	10	11	12	13	14	15	16
SINR	4.4 dB	5.5 dB	6.5 dB	7.5 dB	8.5 dB	9.5 dB	10.7 dB	11.5 dB
CQI	17	18	19	20	21	22	23	24
SINR	12.6 dB	13.4 dB	14.7 dB	15.7 dB	16.6 dB	17.5 dB	18.6 dB	19.6 dB
CQI	25	26	27	28	29	30		
SINR	20.6 dB	21.4 dB	22.6 dB	23.5 dB	24.0 dB	24.8 dB		

Table 3.1: SINR-CQI Mapping Table for single-stream mode.

CQI	0	1	2	3	4	5	6	7
SINR	10.5 dB	10.5 dB	11.2 dB	12.7 dB	14.3 dB	15.7 dB	17.2 dB	18.8 dB
CQI	8	9	10	11	12	13	14	
SINR	20.4 dB	21.9 dB	23.4 dB	25.3 dB	26.0 dB	26.8 dB	28.3 dB	

Table 3.2: SINR-CQI Mapping Table for double-stream mode.

3.6. Achievable Throughput

In this section, a so-called "achievable throughput" is defined. It is used as a performance bound for the actually measured data throughput in Section 3.7. The calculation of the bound is based on the mutual information between transmit and receive signals, that is, the estimated frequency response. The achievable throughput is a function of the wireless channel and the allowed precoding vectors. Thus, it incorporates the restrictions given by the transmission standard (quantized, frequency-flat precoding) but not the restrictions given by the receiver employed.

Consider the time-dispersive channel of length L_h chips between the n_t-th transmit and the n_r-th receive antenna:

$$\mathbf{h}^{(n_\mathrm{r},n_\mathrm{t})} = \left[\begin{array}{ccc} h_0^{(n_\mathrm{r},n_\mathrm{t})} & \ldots & h_{L_\mathrm{h}-1}^{(n_\mathrm{r},n_\mathrm{t})} \end{array} \right]^\mathrm{T}. \tag{3.56}$$

This channel can be equivalently described in the frequency domain as $\mathbf{g}^{(n_\mathrm{r},n_\mathrm{t})} = \mathfrak{F}\left\{\mathbf{h}^{(n_\mathrm{r},n_\mathrm{t})}\right\}$ by using the N_FFT point Fourier transform $\mathfrak{F}\{.\}$. The Fourier transform separates the frequency selective channel into N_FFT frequency flat channels. The MIMO channel matrix

of the q-th frequency bin can then be written as

$$\mathbf{G}_q = \begin{bmatrix} \left(\mathbf{g}^{(1,1)}\right)_q & \cdots & \left(\mathbf{g}^{(1,N_\mathrm{T})}\right)_q \\ \vdots & \ddots & \vdots \\ \left(\mathbf{g}^{(N_\mathrm{R},1)}\right)_q & \cdots & \left(\mathbf{g}^{(N_\mathrm{R},N_\mathrm{T})}\right)_q \end{bmatrix} \quad ; q = 1 \dots N_\mathrm{FFT}. \tag{3.57}$$

By using the well-known expressions for MIMO capacity (see for example [106–109]), the achievable throughput is obtained as

$$D_\mathrm{achievable} = \max_{\mathbf{W} \in \mathcal{W}} \sum_{q=1}^{N_\mathrm{FFT}} \frac{f_\mathrm{s}}{N_\mathrm{FFT}} \log_2 \det \left(\mathbf{I}_{N_\mathrm{R}} + \frac{P_\mathrm{HS-PDSCH}}{\sigma_v^2} \mathbf{G}_q \mathbf{W} \mathbf{W}^\mathrm{H} \mathbf{G}_q^\mathrm{H} \right). \tag{3.58}$$

Here, f_s corresponds to the chip rate of HSDPA (3.84 MHz), $P_\mathrm{HS-PDSCH}$ to the amount of power assigned to the data channels by the base station, and σ_v^2 to the variance of the additive noise $\mathbf{v}_k$. The maximization is performed over the set of all possible precoding matrices $\mathcal{W}$. Note that Equation (3.58) does neither represent the mutual information, nor the channel capacity since only quantized and frequency independent precoding is utilized in HSDPA. Therefore, the symbol $D_\mathrm{achievable}$ is referred to as "achievable throughput". Also note that Equation (3.58) only gives the achievable throughput for a specific channel realization at a specific receive antenna position and a given transmit power level. In order to obtain a mean achievable throughput, averaging over all measured receive antenna positions is performed. Also, since the channel is not known perfectly, the estimated channel coefficients at the largest transmit power (thus having the smallest possible channel estimation error) are used to calculate the achievable throughput. At lower transmit powers, the different channel SNRs are obtained by scaling the channel coefficients accordingly.

3.7. Measurement Results

In this section, the throughput measurement results (the solid lines in Figures 3.6–3.9) are presented and compared to the achievable throughput (the dashed lines in Figures 3.6–3.9). The transmit powers of the different HSDPA chip streams relative to the total transmit power as well as channel estimator and equalizer lengths are listed in Table 3.3.

In the figures, all throughput curves are plotted over transmit power. Two additional x-axes show the average (over all channel realizations and all antennas) received SISO SNR and the average received SISO signal power. Note that the average SNR over all receive antennas does not necessarily reflect the typical SNR of an individual antenna. In our measurements, we observed large differences (3-5 dB) of the SNR at each individual antenna. These differences can actually be exploited by systems that use antenna selection [138].

The reason why the throughput is plotted over transmit power is the following: All MIMO schemes in HSDPA utilize adaptive precoding at the transmitter that effectively increases the received power and thus also the SNR while the total transmit power is the same as in the SISO transmission. If the throughput is plotted over SNR rather than over transmit power, the curves will be shifted against each other. For example, in case of TxAA this shift would be about 2 dB compared to SISO. The additional x-axes (average received SISO SNR and average received SISO power) are thus only shown for reference reasons to indicate the approximate SNR and receive power ranges.

	Alpine Scenario	Urban Scenario
HS-PDSCH E_c/I_{or}	-4 dB	-4 dB
CPICH E_c/I_{or}	-10 dB	-10 dB
SCH/PCCPCH E_c/I_{or}	-12 dB	-12 dB
Channel estimator length L_h	23 chips	48 chips
Equalizer length L_f	30 chips	60 chips

Table 3.3: Measurement Parameters.

3.7.1. Alpine Scenario

Figure 3.6 shows the measured and the achievable throughput of the 1×1 SISO, the 1×2 SIMO, the 2×1 TxAA, the 2×2 TxAA, and the 2×2 D-TxAA transmission systems in the alpine scenario. Although all these schemes are standardized, only the 1×1 SISO transmission is currently used in HSDPA networks.

Several observations can be made in Figure 3.6:

- The measured throughput of the 2×1 TxAA system is significantly (about 3 dB) better than the throughput of the SISO system. Since the 2×1 TxAA system almost achieves the performance of the 1×2 SIMO system, it can be concluded that the precoding works almost optimally in this scenario.
- The 2×2 D-TxAA system also performs very well, achieving more than twice the throughput of the SISO system.
- The achievable throughput of the 2×1 TxAA system is almost the same as the achievable throughput of the SISO system. This is caused by the inclusion of the quantized precoding matrices in the calculation of the achievable throughput (see Equation (3.58)). The multiplication of the channel matrix with the precoding matrix effectively reduces the 2×1 system to a SISO system. Although the achievable throughput is the same for 2×1 TxAA and SISO, it is very interesting that a significant gain in the measured throughput is observed, as explained above.
- The achievable throughput of the 2×2 TxAA system is smaller than the one of the 1×2 SIMO system. This can be explained by the same argumentation as above; that is, due to the precoding, the 2×2 TxAA system is effectively reduced to a 1×2 SIMO system in the calculation of the achievable throughput.

The comparison between the measured and the achievable throughput should be performed at a transmit power of about 10-25 dBm or a throughput of about 5 Mbit/s to avoid saturation effects of the measured throughput (since outside this range either no more smaller or larger CQI values are available). At large transmit power, when the single-stream transmission modes saturate, such a comparison would be unfair since the throughput could be easily increased by providing additional modulation and coding schemes. At a throughput of 5 Mbit/s, the measured SISO and 2×2 D-TxAA throughputs loose about 6 dB and 5 dB compared to their corresponding achievable throughputs.
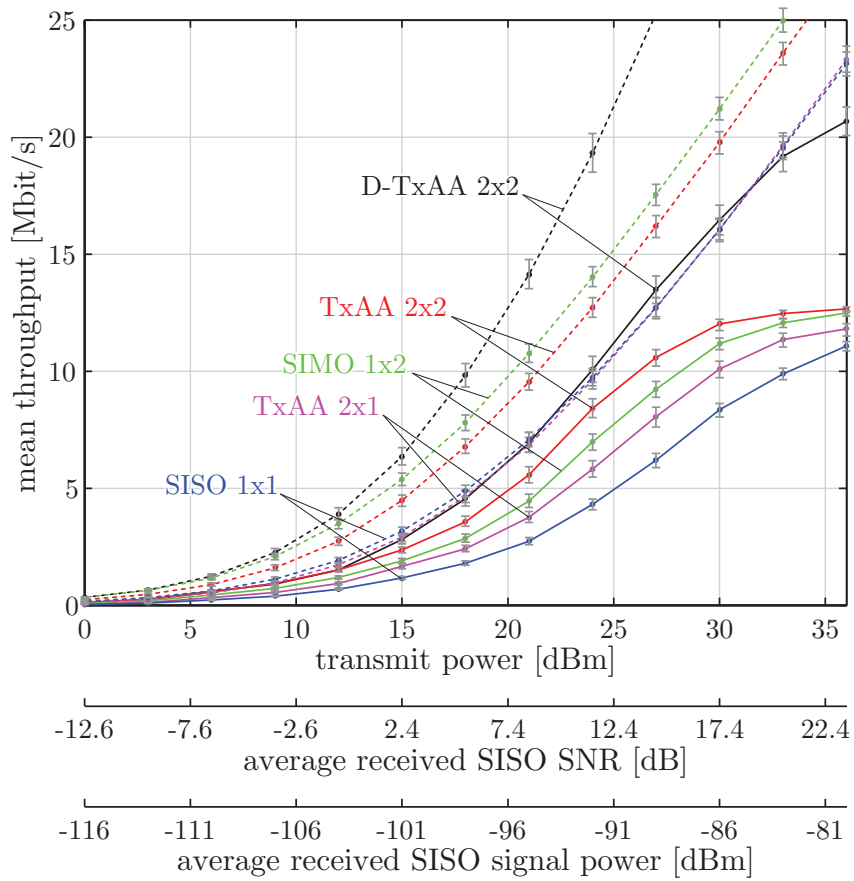
Figure 3.6: Throughput results of the standard compliant schemes in the alpine scenario (ID "2008-09-16"). Averaging was performed over 110 receiver positions. The solid lines represent the measured throughput, the dashed lines the achievable throughput.

Figure 3.7 shows the throughput of the four transmit antenna HSDPA schemes compared to the standard compliant 2×2 D-TxAA system in the alpine scenario. The following observations can be made:

- The achievable throughput curves of the 4×4 and the 4×2 systems are almost equal to the ones of the 2×4 and the 2×2 systems. Again, this is explained by the inclusion of the precoding matrices in the achievable throughput calculation.
- Although the achievable throughputs do not show a gain due to the use of four transmit antennas, the measured throughput is increased significantly. For the 4×4 system, the measured throughput is about twice of that of the 2×2 system. In terms of SNR, the 4×4 system gains about 6 dB.
- The theoretical maximum throughput of all four schemes plotted in Figure 3.7 is 27.952 Mbit/s. However, the measured throughput saturates before reaching this maximum value because of residual interference after the equalization. In the four receive antenna schemes,the equalizer is able to reduce the post equalization interference to a lower level than in the two receive antenna schemes. Therefore, the maximum measured data throughput of the four receive antenna schemes is larger than that of the two receive antenna schemes.
- Comparing the achievable throughput to the measured throughput reveals about 3 dB loss for the 4×4 system and about 6 dB loss for the 2×2 system.
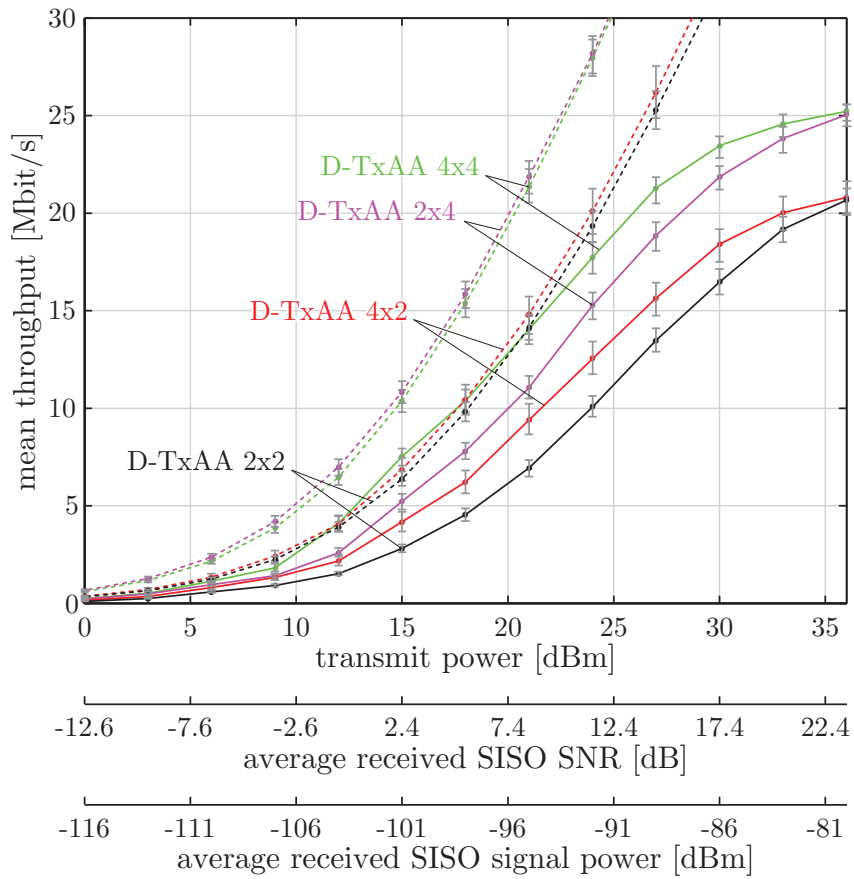
Figure 3.7: Throughput results of the extended schemes in the alpine scenario (ID "2008-09-16"). Averaging was performed over 110 receiver positions. The solid lines represent the measured throughput, the dashed lines the achievable throughput.

3.7.2. Urban Scenario

In Figure 3.8, the results of the standard compliant schemes in the urban scenario are shown. In contrast to the alpine scenario, here, at low SNRs the 2×1 TxAA system only performs marginally better than the SISO system and is worse than SISO at large SNR. The reason for this is the rather large delay spread of about 20 chips causing the precoding to be far from optimal. Optimal precoding has to be frequency dependent, for example, using a water-filling solution. Near-optimum precoding behavior can be achieved in case of OFDM even with quantized feedback [139, 140]. The large delay spread also causes inter-code interference that can only be partially removed by the LMMSE equalizer. Therefore, also the loss between measured and achievable throughput is greater than in the alpine scenario. For the SISO system about 9 dB loss in terms of SNR was measured. As in the alpine scenario, the 2×2 D-TxAA system yields about twice the throughput of the SISO system.
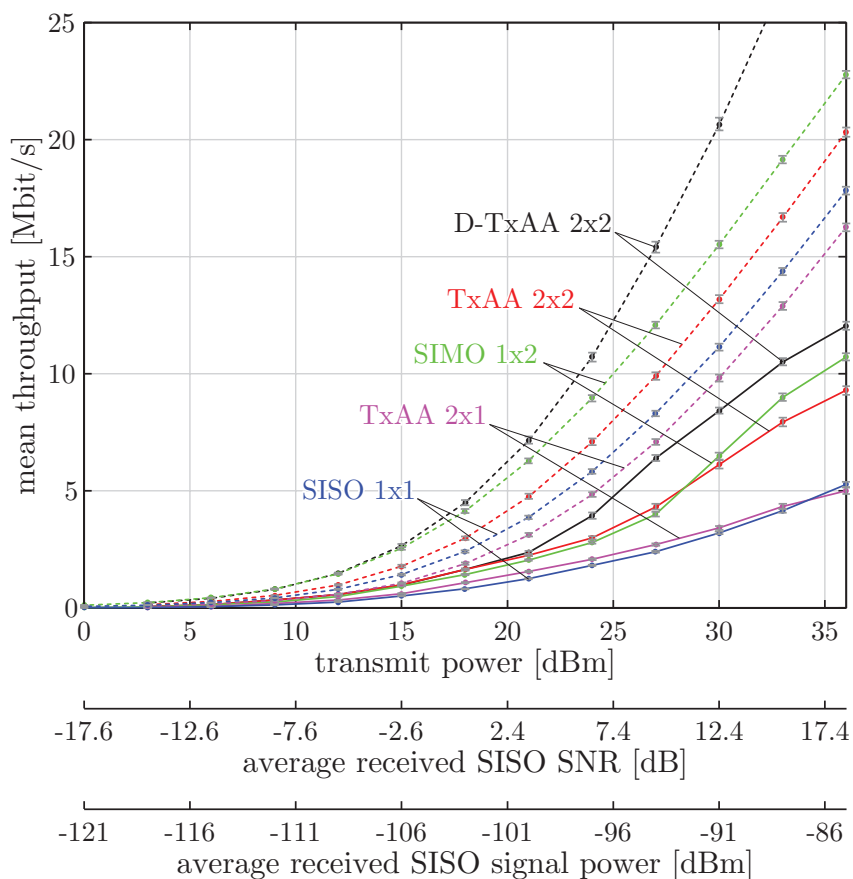

Figure 3.8: Throughput results of the standard compliant schemes in the urban scenario (ID "2009-01-15c"). Averaging was performed over 484 receiver positions. The solid lines represent the measured throughput, the dashed lines the achievable throughput.

The results for the four transmit antenna schemes in the urban scenario are plotted in Figure 3.9. Here, the gains of the four transmit antenna schemes are about the same as in the alpine scenario. The 4×4 system outperforms the 2×2 system by slightly more than 6 dB in SNR or by more than a factor of two in terms of throughput. Figure 3.9 also shows that in the urban scenario most of the throughput gains are due to the four receive antennas. Four transmit antennas only yield small throughput gains in this scenario. In contrast to the alpine scenario, the achievable throughputs of the 4×4 and the 4×2 system are lower than the ones of the 2×4 and the 2×2 system. This is a result of the long delay spread causing the precoding to be not optimal (see also the discussion above).
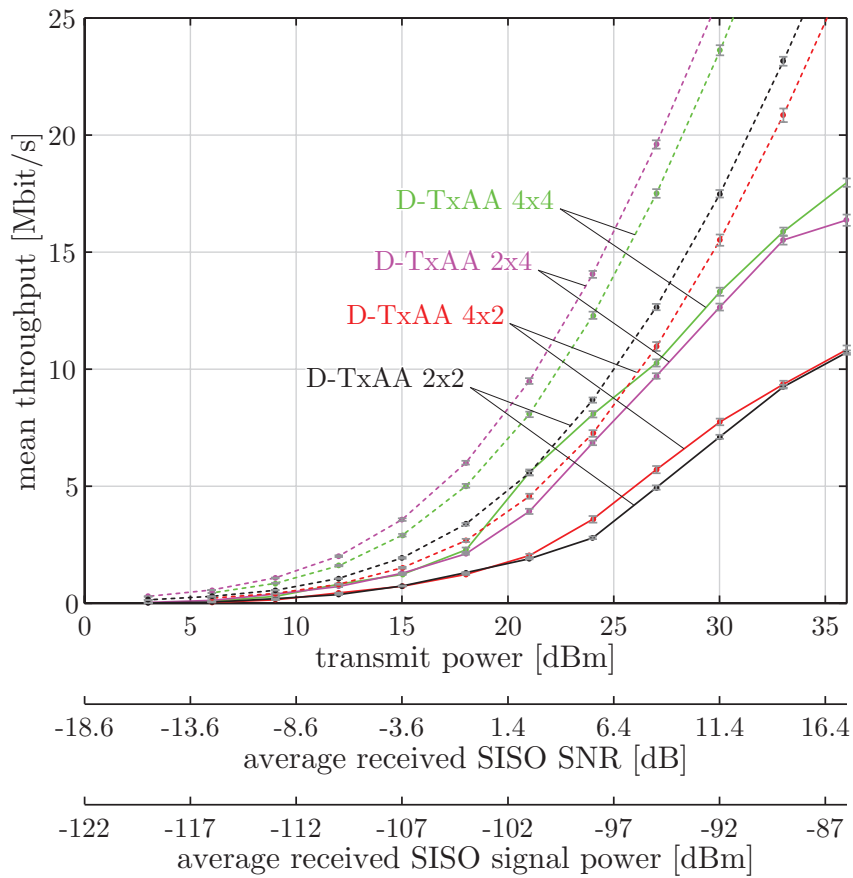

Figure 3.9: Throughput results of the extended schemes in the urban scenario (ID "2008-12-12"). Averaging was performed over 484 receiver positions. The solid lines represent the measured throughput, the dashed lines the achievable throughput.

3.7.3. Discussion of the Throughput Loss

Although the results of the previous sections show a significant performance increase of the different MIMO schemes when compared to the SISO transmission, all measured throughput curves are about 3 to 9 dB away from the achievable throughput. The following effects contribute (next to maybe others) to this loss:

- The rate-matched Turbo code utilized in HSDPA is good but not optimal. AWGN simulations show that at higher code rates, it looses up to 2 dB when decoded by a MAP decoder *(approx. 2 dB)*.
- The LMMSE equalizer representing a low complexity and cost-effective solution is also not optimal. Better receivers like the LMMSE-MAP have the potential to improve the performance by about 1 dB [141]. *(approx. 1 dB)*
- In the urban scenario, a larger throughput loss than in the alpine scenario was measured because of the larger delay spread and, consequently, the larger inter-code interference. For example, in the alpine scenario the SISO system looses about 6 dB to the achievable throughput, whereas the loss in the urban scenario is about 9 dB *(3 dB additional loss in the urban scenario compared to the alpine scenario)*.
- In case of MIMO transmission, the freedom of choosing a precoding matrix maximizing the post-equalization SINR decreases the loss to the achievable throughput. It should be noted, though, that if optimum precoding is performed at the transmitter, the achievable throughput is even larger (see Section 4.3).

3.8. Summary

MIMO HSDPA throughput measurement results obtained in two extensive measurement campaigns are presented in this chapter. The campaigns were carried out in an alpine valley in Austria and in the inner city of Vienna, Austria. The scenarios differ significantly in the delay spread of the channel. In both scenarios, the use of multiple antennas considerably increases the physical layer throughput. Already the standard compliant 2×2 system increases the physical layer throughput by more than a factor of two compared to the SISO system. The 4×4 system furthermore increases the throughput by a factor of two. Absolute values of the measured throughputs are shown in Table 3.4 and Figure 3.10 for transmit powers of 20 and 30 dBm.

	Alpine Scenario		Urban Scenario	
	260 ns mean RMS delay spread		1.1 µs mean RMS delay spread	
	$P_{\mathrm{TX}} = 20\,\mathrm{dBm}$	$P_{\mathrm{TX}} = 30\,\mathrm{dBm}$	$P_{\mathrm{TX}} = 20\,\mathrm{dBm}$	$P_{\mathrm{TX}} = 30\,\mathrm{dBm}$
1×1 SISO	2.4 Mbit/s	8.3 Mbit/s	1.1 Mbit/s	3.2 Mbit/s
2×1 TxAA	3.3 Mbit/s	10.1 Mbit/s	1.4 Mbit/s	3.4 Mbit/s
1×2 SIMO	3.9 Mbit/s	11.2 Mbit/s	1.8 Mbit/s	6.5 Mbit/s
2×2 TxAA	4.9 Mbit/s	12.0 Mbit/s	2.0 Mbit/s	6.1 Mbit/s
2×2 D-TxAA	6.1 Mbit/s	16.5 Mbit/s	2.0 Mbit/s	8.2 Mbit/s
4×2 D-TxAA	8.3 Mbit/s	18.4 Mbit/s	2.3 Mbit/s	8.5 Mbit/s
2×4 D-TxAA	10.0 Mbit/s	21.9 Mbit/s	4.4 Mbit/s	14.1 Mbit/s
4×4 D-TxAA	12.8 Mbit/s	23.5 Mbit/s	6.0 Mbit/s	14.6 Mbit/s

Table 3.4: Inferred mean measured HSDPA throughput in the alpine and urban scenarios at transmit powers $P_{\mathrm{TX}} = 20\,\mathrm{dBm}$ and $P_{\mathrm{TX}} = 30\,\mathrm{dBm}$.

In order to compare the measured throughput to a performance bound, an achievable throughput is defined. This achievable throughput is calculated based on the mutual information of the channel and the precoding employed at the transmitter. Comparing the measured and the achievable throughput shows that the measured throughput is far from optimal, loosing between 3 and 9 dB in SNR. This loss is caused by the channel coding (about 2 dB), the sub-optimal LMMSE equalizer (about 1 dB), inter-code interference, and channel estimation errors. Since HSDPA allows for a very high number of possible modulation and coding schemes (for example in D-TxAA there are 570 different schemes), a measurement procedure that requires the feedback implementation in a mini-receiver, as explained in Section A.2.1, was employed. If alternate receiver structures (for example

enhanced channel estimators or MAP detection) should be investigated using the selected procedure, the mini-receiver has to be modified. Therefore, the quantification of the exact value of the channel estimation loss requires reference measurements with a genie-driven channel estimator that perfectly knows the transmitted chip stream. After performing such a reference measurement, the unidentified SNR loss can be separated into a channel estimation loss, an inter-code interference loss, and probably also into a further, now still unknown, loss.
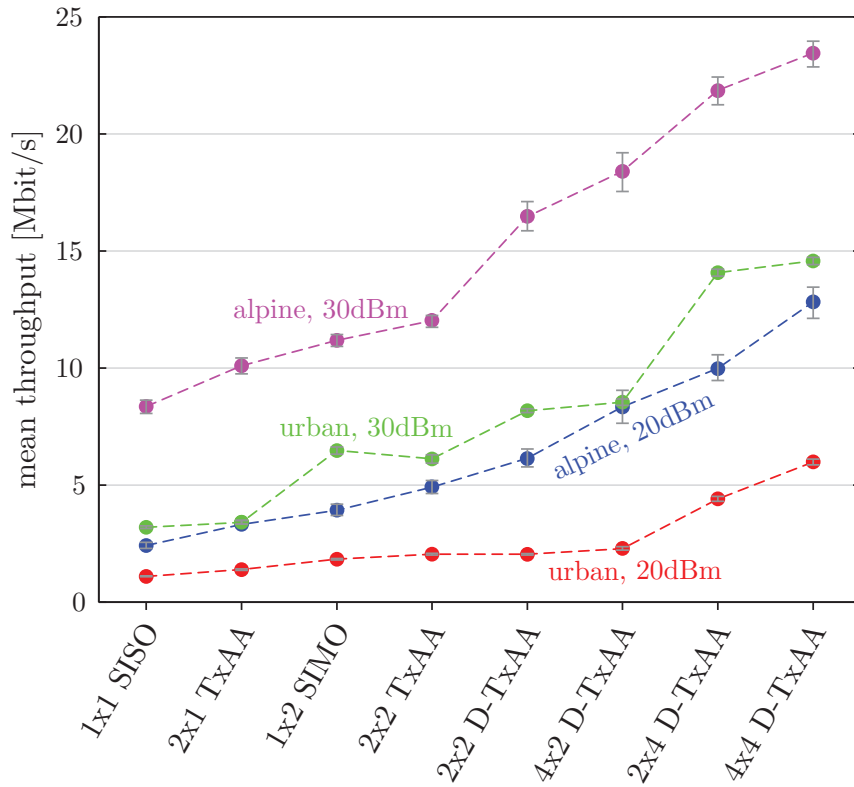

Figure 3.10: Inferred mean throughput of the different MIMO schemes in the alpine and the urban scenarios for $P_{\text{TX}} = 20\,\text{dBm}$ and $P_{\text{TX}} = 30\,\text{dBm}$.

Chapter 4.

WiMAX-HSDPA Comparison

In this chapter, a comparison between WiMAX and HSDPA is presented in terms of

1. the measured throughput,
2. the achievable throughput (considering the inherent system losses),
3. the mutual information given by the estimated channel coefficients, and
4. the channel capacity that is obtained by optimum, frequency-selective precoding at the transmitter.

The quite different nature of the HSDPA and WiMAX signals makes comparisons of the two systems difficult. Although both systems use a channel bandwidth of 5 MHz, the actually occupied spectrum is different due to the different modulation (CDMA in case of HSDPA and OFDM in case of WiMAX). In HSDPA, the transmit chip stream (3.84 MChip/s) is Root Raised Cosine (RRC) filtered with a roll-off factor $\alpha = 0.22$ leading to a total occupied bandwidth of 4.68 MHz. In WiMAX, the sampling rate in case of 5 MHz channel bandwidth is 5.76 MHz, as defined in [5, Section 8.3.2]. In this 5.76 MHz bandwidth, only 201 out of the total 256 subcarriers carry useful information. The remaining 55 carriers, modulated with zeros, are required as guard band to reduce leakage into neighboring frequency bands. Thus, only 4.52 MHz are occupied by the data and pilot symbols.

The different signals of HSDPA and WiMAX naturally lead to different receiver SNRs, if calculated after the receive filter (RRC filter in case of HSDPA and rectangular filter, corresponding to separation of data and guard band carriers, in case of WiMAX). Therefore, the SNR for a comparison of HSDPA and WiMAX must be calculated *before* receive filtering. The SNR definition used in this chapter, therefore is the SNR directly after sampling and before receive filtering. This causes some differences in the labeling of the x-axes in this chapter when compared to the results in Chapters 2 and 3.

The comparison of HSDPA and WiMAX is carried out in three steps. At first, Section 4.1 provides a comparison in terms of measured and achievable throughput. Secondly, in Section 4.2, the achievable throughput of HSDPA and WiMAX is compared to the mutual information of the channel to provide deeper insight into the inherent system losses. Thirdly, in Section 4.3, the channel capacity is calculated and compared to the mutual information. Finally, Section 4.4 presents the conclusions of this chapter.

4.1. Measured Throughput and Achievable Throughput

In case of the WiMAX system, several channel coding and channel estimation schemes have been investigated in Chapter 2. Since the ALMMSE channel estimator provides a good performance/complexity trade-off, it is selected for the following performance comparison. The best performing channel coding scheme (LDPC) is not specified in the IEEE 802.16-2004 standard [5]. Therefore, the second best performing scheme, the CTC channel coding that is optionally standardized in [5], was selected for the comparisons to HSDPA (which also employs a Turbo code).

Figure 4.1 shows the measured and achievable throughputs of SISO and 2×2 MIMO transmissions in the alpine scenario. Figure 4.2 shows the same curves for the urban scenario. Two important observations can be made in these figures:

1. The achievable throughput of the HSDPA system is larger than the achievable throughput of the WiMAX system. Thus, in HSDPA a smaller part of the mutual information is sacrificed as system overhead. In fact, the system overhead of HSDPA is given by the portion of the transmit power *not* assigned to the data channels (taken into account by the factor $P_{\text{HS-PDSCH}}$ in Equation (3.58)). In case of WiMAX, a much larger overhead is required by the cyclic prefix and the guard bands (see Equation (2.27)). However, the OFDM signal structure of WiMAX ensures interference free reception at the receiver. The advantages of the OFDM signal are especially visible in the results of the urban scenario in Figure 4.2. In this long delay spread urban scenario, HSDPA heavily suffers from inter-code interference leading to a significant throughput loss.
2. HSDPA utilizes the two transmit antennas much better than WiMAX. In the alpine scenario, MIMO HSDPA even achieves a larger throughput than MIMO WiMAX although it is the other way round for the SISO transmission. In the urban scenario, MIMO HSDPA significantly increases the performance over SISO HSDPA since the inter-code interference is effectively combated by the adaptive selection of the precoding matrices (see also the discussion in Section 3.7).
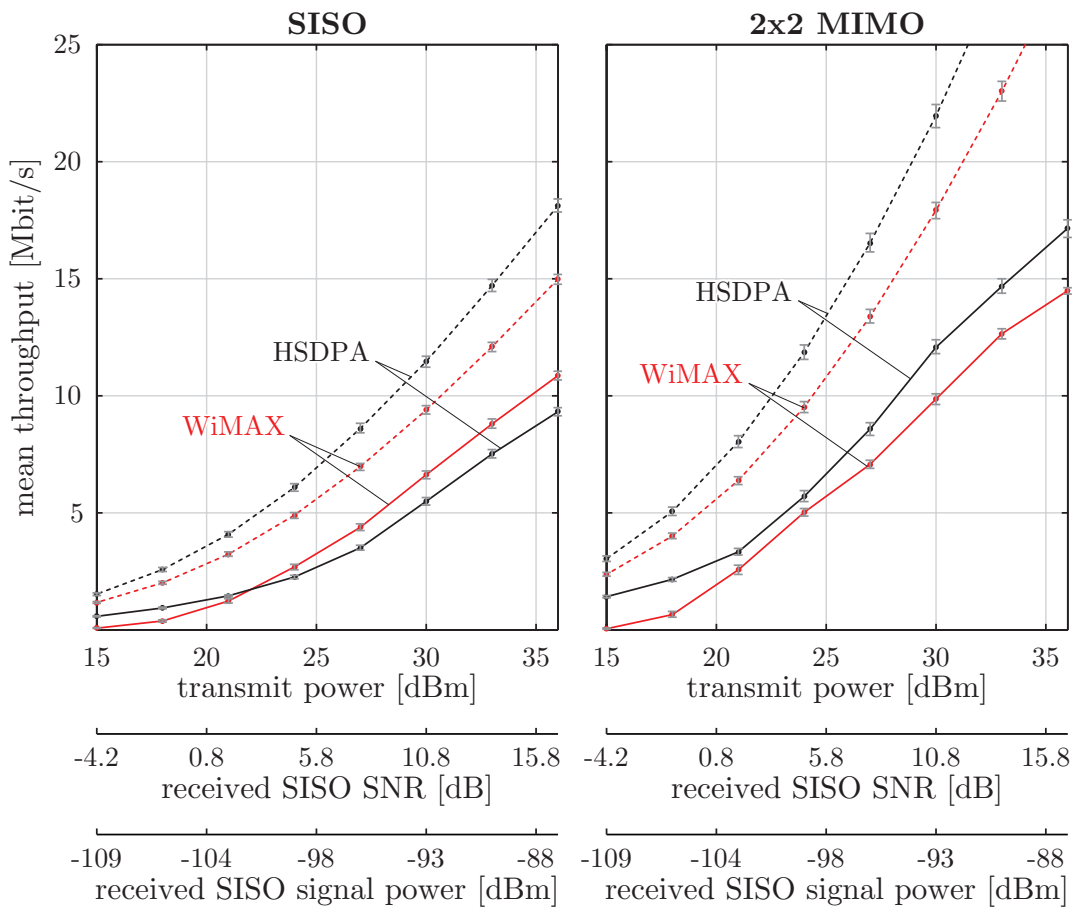
Figure 4.1: HSDPA and WiMAX throughputs of SISO and 2×2 MIMO transmissions in the alpine scenario (ID "2008-09-23"). The solid lines represent the measured throughput, the dashed lines the achievable throughput.

Overall, the WiMAX system shows slightly better performance than the HSDPA system. It should be noted, however, that the feedback of WiMAX is implemented ideally, as explained in Section 2.4. A more realistic feedback implementation would degrade the WiMAX performance by an amount that has to be investigated.
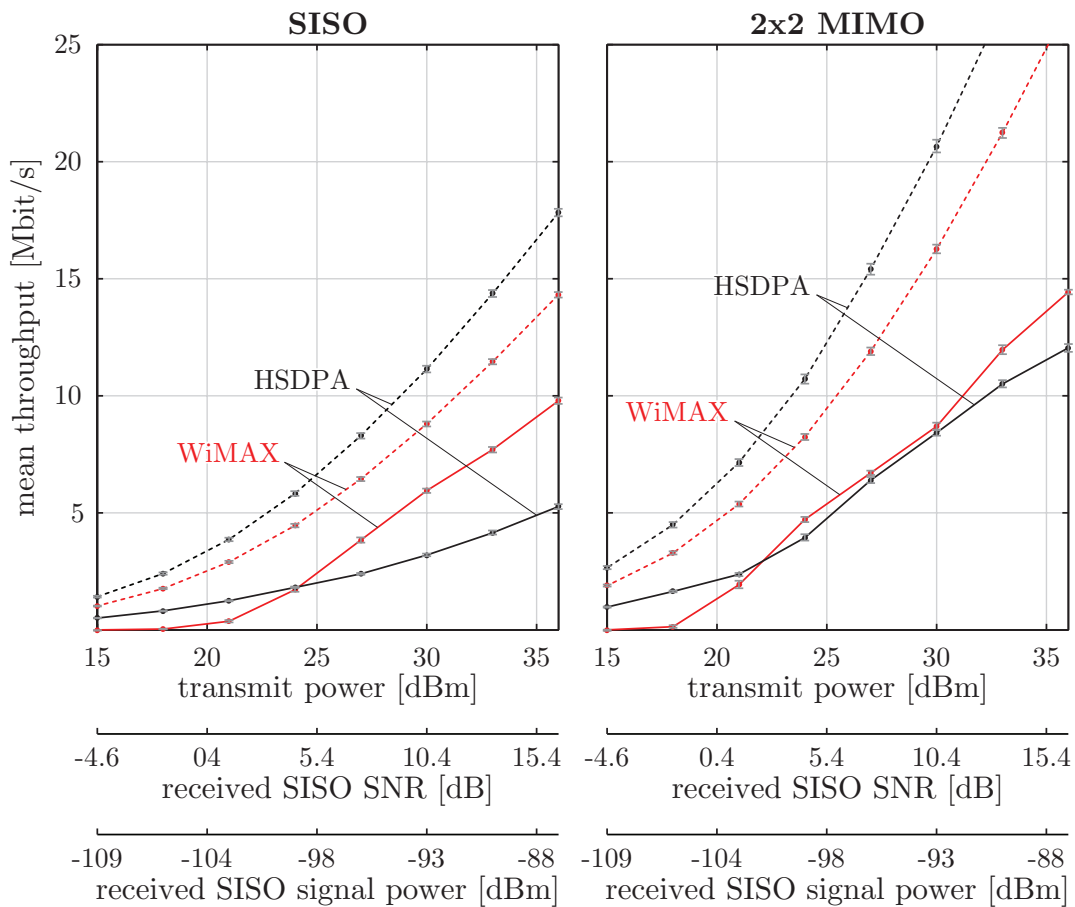
Figure 4.2: HSDPA and WiMAX throughputs of SISO and 2×2 MIMO transmissions in the urban scenario (ID "2009-01-15c"). The solid lines represent the measured throughput, the dashed lines the achievable throughput.

4.2. Achievable Throughput and Mutual Information

In this section, the mutual information of the WiMAX and the HSDPA system is defined and compared. In theory, the mutual information only depends on the channel coefficients. However, since the mutual information curves plotted here are calculated from the estimated channel coefficients of two totally different systems, the mutual information of WiMAX and HSDPA will not match exactly. One reason is that the two signals occupy different portions of the available channel bandwidth. For the comparison, the achievable throughput is normalized to the channel bandwidth, yielding a throughput value [bit/s] that can be achieved per Hertz of channel bandwidth.

WiMAX Mutual Information and Normalized Achievable Throughput

The mutual information in case of the WiMAX transmission was already defined in Equation (2.24). For a specific channel realization and transmit power value, the mutual information in bit/s/Hz is

$$\tilde{I}^{\mathrm{WiMAX}} = \frac{1}{192} \sum_{k=1}^{192} \log_2 \det \left(\mathbf{I} + \frac{1}{\sigma_v^2} \mathbf{H}_k \mathbf{H}_k^{\mathrm{H}} \right). \tag{4.1}$$

Here, $\mathbf{H}_k$ denotes the MIMO channel matrix at subcarrier index k and σ_v^2 the noise variance. The normalized achievable throughput for the same channel realization and transmit power value is given analogously to Equation (2.27) as

$$\tilde{D}_{\mathrm{achievable}}^{\mathrm{WiMAX}} = \frac{1}{1+G} \cdot \frac{192}{256} \cdot \frac{N_{\mathrm{data}}}{N_{\mathrm{OFDM}}} \cdot \frac{f_{\mathrm{s}}^{\mathrm{WiMAX}}}{f_{\mathrm{B}}} \cdot \tilde{I}, \tag{4.2}$$

in which $f_{\mathrm{s}}^{\mathrm{WiMAX}} = 5.76\,\mathrm{MHz}$ is the sampling frequency of the WiMAX signal and $f_{\mathrm{B}} = 5.0\,\mathrm{MHz}$ the channel bandwidth. Note that although the WiMAX signal actually only occupies $\frac{201}{256} \cdot 5.76\,\mathrm{MHz} = 4.5\,\mathrm{MHz}$, the channel bandwidth is $5\,\mathrm{MHz}$. The additional bandwidth is required to reduce interference into neighboring channels and can thus be considered as inherent system loss. Therefore it is taken into account when calculating the achievable throughput but not when calculating the mutual information.

HSDPA Mutual Information and Normalized Achievable Throughput

The mutual information in case of the HSDPA transmission is given by

$$\tilde{I}^{\mathrm{HSDPA}} = \frac{1}{N_{\mathrm{FFT}}} \sum_{q=1}^{N_{\mathrm{FFT}}} \log_2 \det \left(\mathbf{I}_{N_{\mathrm{R}}} + \frac{1}{\sigma_v^2} \mathbf{G}_q \mathbf{G}_q^{\mathrm{H}} \right), \tag{4.3}$$

with the MIMO channel matrices $\mathbf{G}_q$ at frequency bin q defined according to Equation (3.57). The normalized achievable throughput $\tilde{D}_{\mathrm{achievable}}^{\mathrm{HSDPA}}$ is obtained by multiplying with the chip rate $f_{\mathrm{s}}^{\mathrm{HSDPA}} = 3.84\,\mathrm{MHz}$ and normalizing to the channel bandwidth $f_{\mathrm{B}} = 5.0\,\mathrm{MHz}$. Furthermore, the spatial precoding at the transmitter has to be incorporated (see Equation (3.58)):

$$\tilde{D}_{\mathrm{achievable}}^{\mathrm{HSDPA}} = \frac{f_{\mathrm{s}}^{\mathrm{HSDPA}}}{f_{\mathrm{B}}} \frac{1}{N_{\mathrm{FFT}}} \max_{\mathbf{W} \in \mathcal{W}} \sum_{q=1}^{N_{\mathrm{FFT}}} \log_2 \det \left(\mathbf{I}_{N_{\mathrm{R}}} + \frac{P_{\mathrm{HS-PDSCH}}}{\sigma_v^2} \mathbf{G}_q \mathbf{W} \mathbf{W}^{\mathrm{H}} \mathbf{G}_q^{\mathrm{H}} \right). \tag{4.4}$$

The factor $P_{\mathrm{HS-PDSCH}}$ corresponds to the amount of power assigned to the data channels by the base station and takes the losses of transmit power due to the transmission of the pilot and control channels into account.
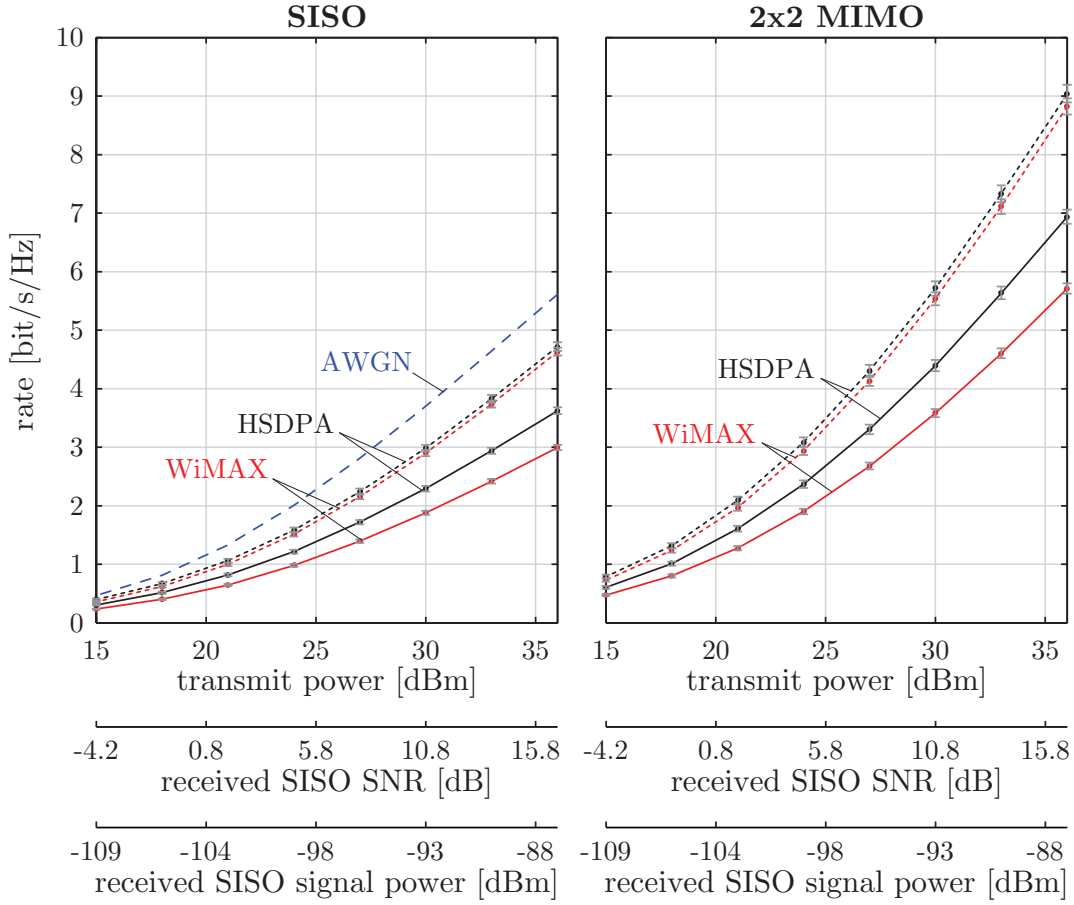
Figure 4.3: HSDPA and WiMAX mutual information and achievable throughput of SISO and 2×2 MIMO transmissions in the alpine scenario (ID "2008-09-23"). The solid lines represent the achievable throughput, the dashed lines the mutual information. As a reference, the mutual information of an AWGN channel is plotted in the SISO figure.

Figures 4.3 and 4.4 show the mutual information and normalized achievable throughput of the 1×1 SISO and 2×2 MIMO transmissions for WiMAX and HSDPA. While the achievable throughput of HSDPA is significantly larger than that of WiMAX, as in the previous section, the mutual information is almost equal. The only difference between the WiMAX and HSDPA mutual information is caused by the different transmit signal bandwidth. WiMAX spreads the available transmit power over a bandwidth of $\frac{201}{256} \cdot 5.76\,\text{MHz} = 4.5\,\text{MHz}$ and HSDPA over an effective bandwidth of 3.84 MHz. The smaller bandwidth of the HSDPA signal results after receiver filtering in an SNR gain of

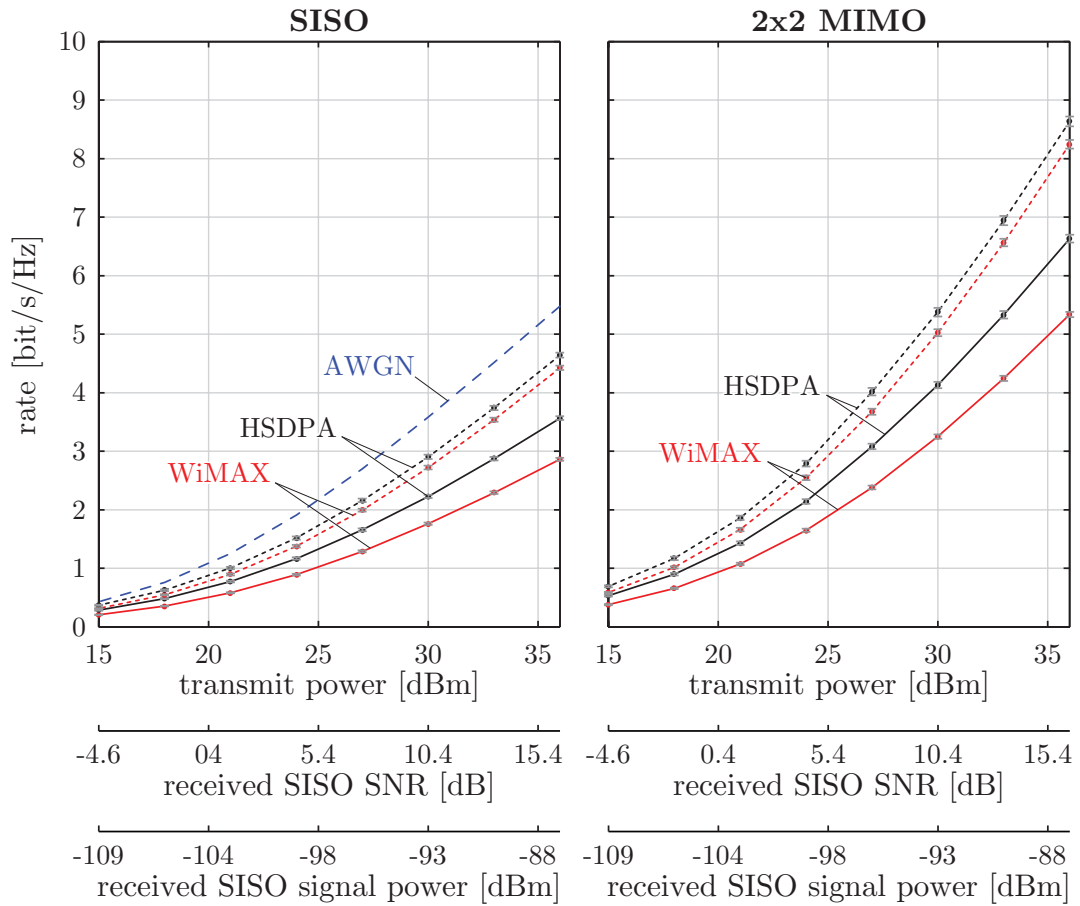$$\text{SNR}_\Delta = \frac{201}{256}\frac{5.76}{3.84} = 1.18 \approx 0.7\,\text{dB}. \tag{4.5}$$

Figure 4.4: HSDPA and WiMAX mutual information and achievable throughput of SISO and 2×2 MIMO transmissions in the urban scenario (ID "2009-01-15c"). The solid lines represent the achievable throughput, the dashed lines the mutual information. As a reference, the mutual information of an AWGN channel is plotted in the SISO figure.

This SNR gain of HSDPA corresponds to the SNR differences between the mutual information curves of HSDPA and WiMAX which are about 0.4 dB in the alpine scenario (Figure 4.3) and about 0.7 dB in the urban scenario (Figure 4.4). Note that if the effective bandwidth of both systems is the same, such an SNR difference will not occur.

As a reference, the mutual information of the AWGN channel is plotted in the left-hand sides of Figures 4.3 and 4.4. The mutual information of a 1×1 and a 2×2 uncorrelated flat Rayleigh fading channel was calculated and found to be equal to the corresponding HSDPA mutual information curves in both the alpine scenario and the urban scenario.

4.3. Channel Capacity and Mutual Information

Since the mutual information in case of the WiMAX and HSDPA transmissions is the same (besides of a 0.7 dB SNR shift due to different transmission bandwidths), the comparison between channel capacity and mutual information in this section is based on the HSDPA transmissions only.

Calculation of the Channel Capacity

For the calculation of the channel capacity of a frequency selective MIMO channel [142, 143], consider the singular value decomposition [118] of the channel at subcarrier k:

$$\frac{1}{\sigma_v}\mathbf{H}_k = \mathbf{U}_k \boldsymbol{\Sigma}_k \mathbf{V}_k^{\mathrm{H}} \quad ; \boldsymbol{\Sigma}_k = \mathrm{diag}\left(\sqrt{\lambda_k^m}\right) \quad m = 1 \ldots \min(N_{\mathrm{R}}, N_{\mathrm{T}}). \tag{4.6}$$

The optimum, capacity-achieving, frequency-depending precoding at the transmitter is given by the unitary matrix $\mathbf{V}_k$. If also at the receiver the optimum receive filter $\mathbf{U}_k^{\mathrm{H}}$ is employed, the MIMO channel is separated into $\min(N_{\mathrm{R}}, N_{\mathrm{T}})$ independent SISO channels each with gain $\sqrt{\lambda_k^m}$, $m = 1 \ldots \min(N_{\mathrm{R}}, N_{\mathrm{T}})$. The channel capacity of such parallel SISO subchannels with unequal gain is obtained by optimally distributing the available transmit power over all λ_k^m. The optimum power distribution P_k^m is the solution to the following optimization problem:

$$C = \max_{P_k} \frac{1}{192} \sum_{m=1}^{\min(N_{\mathrm{R}}, N_{\mathrm{T}})} \sum_{k=1}^{192} \log_2\left(1 + P_k^m \lambda_k^m\right) \tag{4.7}$$

$$\text{subject to} \quad \sum_{m=1}^{\min(N_{\mathrm{R}}, N_{\mathrm{T}})} \sum_{k=1}^{192} P_k^m = 192.$$

Here, the second equation is a transmit power constraint that ensures an average transmit power equal to the number of data subcarriers. The power coefficients maximizing Equation (4.7) can be calculated by using the water-filling algorithm described in [142, 143].

Figure 4.5 shows the mutual information and the capacity in case of the SISO, the 2×2 MIMO, and the 4×4 MIMO transmission in the alpine scenario. Since the channel in this scenario is relatively flat because of the small RMS delay spread of about 260 ns, the optimum power distribution is also frequency flat. Therefore, the capacity and the mutual information of the SISO transmission are the same. In case of the MIMO transmission, the water-filling operates not only over the frequency domain but also over the spatial domain. In case of a 2×2 MIMO transmission with cross polarized transmit antennas, the MIMO
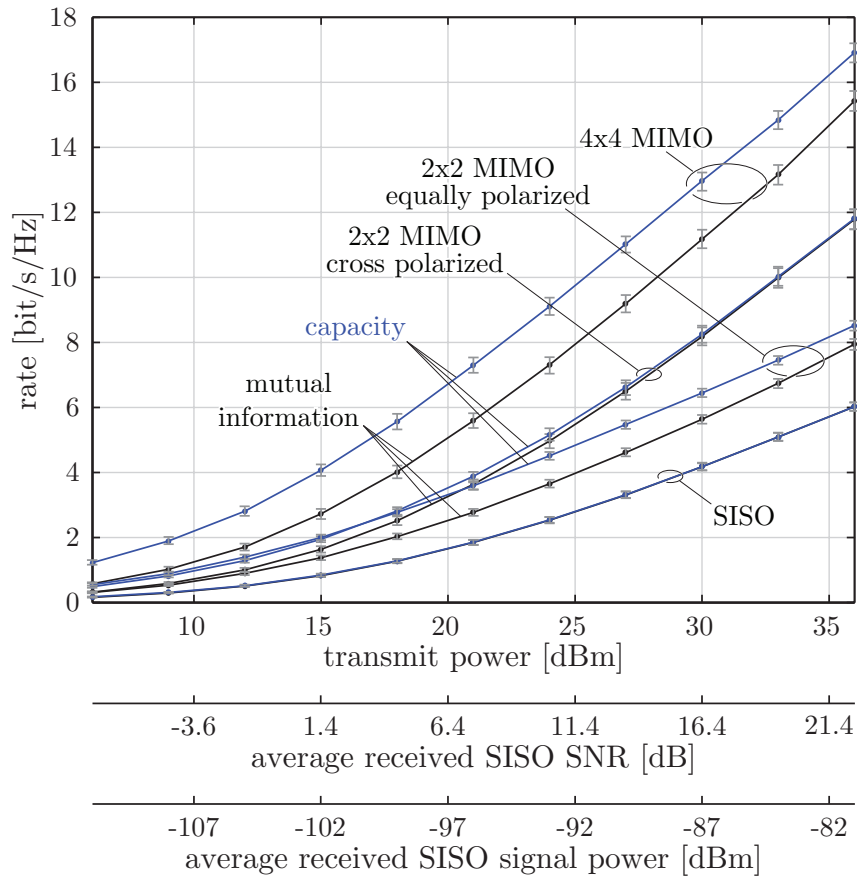
Figure 4.5: Capacity and mutual information of the SISO, the 2×2 MIMO, and the 4×4 MIMO transmissions in the alpine scenario (ID "2008-09-16").

subchannels are very well separated and the gain due to optimum precoding is only small with a maximum of about 0.5 bit/s/Hz at an SNR of 0 dB. If two equally polarized transmit antennas are utilized at the base station, the gain due to optimum precoding is significantly larger than in the cross polarized case. However, both the channel capacity and the mutual information for the transmission with equally polarized transmit antennas is smaller than for cross polarized transmit antennas. If four transmit antennas are utilized at the transmitter, always two antennas have the same polarization and thus high correlation due to the absence of scatterers near the base station. In the four transmit antenna case, optimum precoding therefore results in a large gain of about 2 bit/s/Hz over a wide SNR range.
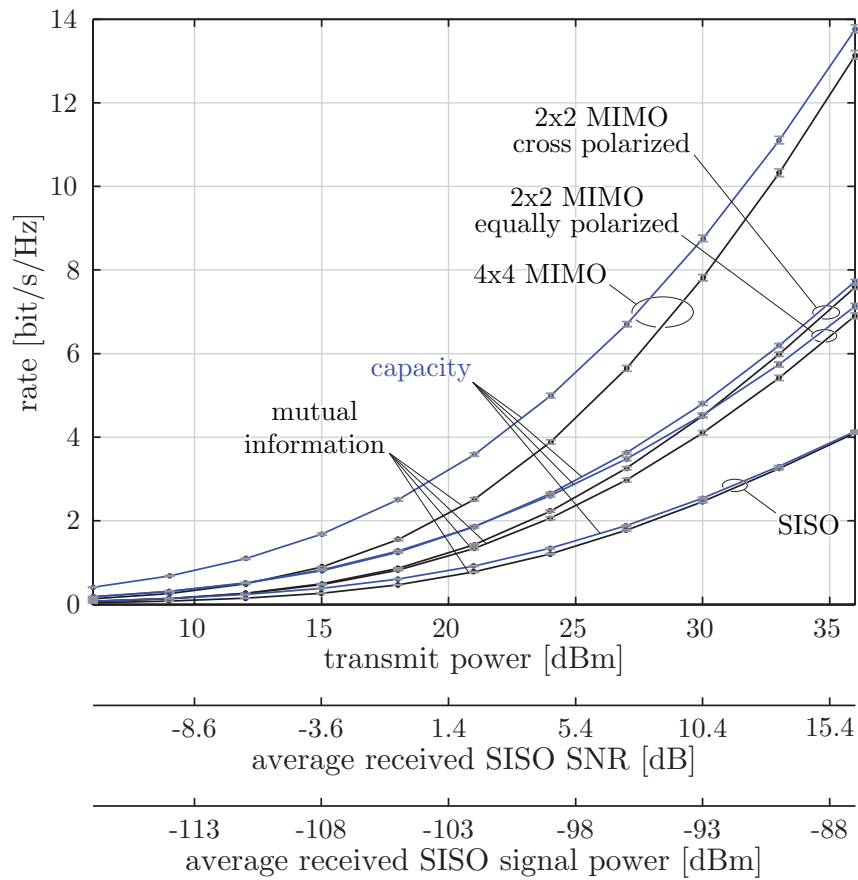
Figure 4.6: Capacity and mutual information of the SISO, the 2×2 MIMO, and the 4×4 MIMO transmissions in the urban scenario (ID "2008-12-12").

Figure 4.6 shows the mutual information and the capacity in case of the SISO, the 2×2 MIMO, and the 4×4 MIMO transmission in the urban scenario. Since the channel in this scenario is time-dispersive with a large RMS delay spread of about 1.1 µs, the capacity of the SISO system is slightly (about 0.15 bit/s/Hz) greater than the mutual information. In case of the 2×2 MIMO transmission with cross polarized transmit antennas, the capacity is —as in the alpine scenario— about 0.5 bit/s/Hz greater than the mutual information at an SNR of about 0 dB. Due to the presence of scatterers around the base station in the urban scenario, the 2×2 MIMO transmission with equally polarized transmit antennas behaves similar to the transmission with cross polarized antennas. In the 4×4 MIMO transmission, the capacity is significantly larger —but not as distinctive as in the alpine scenario— than the mutual information.

4.4. Summary

In this chapter, WiMAX and HSDPA are compared in terms of measured throughput, achievable throughput, mutual information, and capacity. Although HSDPA has a larger achievable throughput than WiMAX, the measured throughput of HSDPA is similar to that of WiMAX. In the alpine scenario, the channel adaptive spatial precoding of HSDPA offers much higher throughput gains than the simple Alamouti coding of WiMAX. In the urban scenario, the HSDPA system suffers from the long delay spread of the channel that causes inter-code interference. In this scenario, the SISO HSDPA system looses significantly compared to SISO WiMAX.

The mutual information of the channel, calculated from the estimated channel coefficients of the WiMAX and the HSDPA transmissions, is approximately the same for both systems. The only difference is a shift of about $0.7\,\text{dB}$ that is caused by the smaller signal bandwidth of HSDPA.

The comparison between mutual information and channel capacity shows that only small gains of at most $0.5\,\text{bit/s/Hz}$ (at SNR $= 0\,\text{dB}$) are possible in case of $2{\times}2$ MIMO transmission with cross polarized transmit antennas. If equally polarized transmit antennas are utilized at the transmitter, a gain of about $1\,\text{bit/s/Hz}$ is observed for the alpine scenario. However, the utilization of two equally polarized transmit antennas is not feasible since it leads to both smaller mutual information and smaller channel capacity. In case of $4{\times}4$ MIMO transmission, always two transmit antennas have the same polarization. The gain due to optimum precoding at four transmit antennas is up to $2\,\text{bit/s/Hz}$ depending on the SNR and the scenario measured.

Chapter 5.

Summary and Outlook

5.1. Summary

In this thesis, a realistic performance evaluation of IEEE 802.16-2004 WiMAX and of Release 7 HSDPA is presented. In contrast to related work in this field, the full physical layer instead of only specific parts is considered. Especially, two important parts of modern wireless communication systems, namely MIMO as well as adaptive modulation and coding, are taken into account and their implementation is described in detail. The performance evaluation is based on two extensive measurement campaigns. These campaigns were carried out in two different scenarios that are realistic and typical deployment sites for WiMAX and HSDPA: an alpine scenario in the Austrian Drautal valley and an urban scenario in the inner city of Vienna, Austria. The main findings of this thesis are summarized in the next paragraphs.

In Chapter 2, the WiMAX system is considered. Besides the standard compliant RS-CC and CTC channel codes, an LDPC channel code was implemented and measured. It turns out that the LDPC code performs about $1\,\mathrm{dB}$ better than the CTC code and about $3\,\mathrm{dB}$ better than the RS-CC code. Besides a genie-driven and a very simple LS channel estimator, a novel ALMMSE channel estimator is introduced. In contrast to the straightforward LMMSE estimator, the ALMMSE estimator inherently calculates the second order statistics of the channel to improve an initial LS estimate. Also, due to reduced matrix sizes, the ALMMSE estimator is of much lower complexity than the LS estimator. A receiver with ALMMSE estimator achieves a physical layer throughput that is approximately in the middle of those the throughput achieved by receivers equipped with a genie-driven and an LS estimator, respectively.

The SNR losses of the different channel codes and channel estimators are analyzed in detail. Depending on the selected channel coding and channel estimation schemes, the SNR loss to the best performing scheme (LDPC coding with genie-driven channel estimation) is up to 6 dB.

Two transmit antennas are utilized in WiMAX by Alamouti space-time coding. Since the Alamouti coding is more sensitive to channel estimation errors than the one transmit antenna system, no substantial performance gains are measured when ALMMSE channel estimation is employed at the receiver. A second receive antenna, however, improves the throughput considerably. When genie-driven channel estimation is employed, the SNR gap between the measured and the achievable throughput corresponds exactly to the channel coding loss. In particular, the best performing LDPC code looses about 2 dB in SNR to the achievable throughput. Only in case of 2×2 transmission, the loss of the measured throughput increases with increasing SNR because the Alamouti space-time code is not a full-rank full diversity code.

In Chapter 3, the HSDPA system is considered. Since, in contrast to WiMAX, HSDPA utilizes much more modulation and coding schemes as well as adaptive spatial precoding and hybrid automated repeat request, the feedback implementation turns out to be more difficult. For example in the double-stream transmission mode there are already 570 different AMC and precoding schemes, not including the HARQ retransmissions. This large number of schemes does not allow to simply successively transmit all schemes as in case of WiMAX. Therefore, the feedback was calculated in a mini-receiver that evaluates the channel quality by means of a test block transmission. For this feedback calculation in the mini-receiver, an analytic model of the HSDPA physical layer was developed. The analytic model considers the estimated channel, the noise variance, the equalizer length, and the channel estimation error. Besides the feedback calculation, this model has been used in system level simulations to accurately describe the HSDPA physical layer.

Since simple correlation-based channel estimation leads to poor performance, especially when the order of the MIMO system increases, a novel tap-wise LMMSE channel estimator was developed. Due to much smaller matrix sizes involved in the estimation, the tap-wise LMMSE estimator has much lower complexity than a direct implementation of the LMMSE estimator. Also, the tap-wise LMMSE estimator inherently estimates the required second order statistics of the channel.

The HSDPA measurement results show that the standard compliant 2×2 system increases the physical layer throughput by more than a factor of two compared to the SISO system. A 4×4 system using a similar precoding structure as the 2×2 system, furthermore increases the throughput by a factor of two. The comparison of the measured throughput with the

achievable throughput reveals large losses between 3 and 9 dB. These losses are caused by the channel coding (about 2 dB), the sub-optimal LMMSE equalizer (about 1 dB), inter-code interference, and channel estimation. The inter-code interference is especially a problem in the urban scenario which has a rather long mean RMS delay spread of about 4.3 chips (1.1 μs). Here, the SISO system looses about 9 dB in SNR compared to the achievable throughput. The utilization of multiple antennas in such a scenario is especially beneficial because it allows to select precoding matrices that maximize the post equalization SINR (equivalently to minimizing the inter-code interference). Therefore, the MIMO gain in the urban scenario is higher than in the alpine scenario.

In Chapter 4, a comparison between HSDPA and WiMAX is presented. The measured throughput of both systems is very similar, with some advantages for the WiMAX system in the urban scenario. In this scenario, the HSDPA system suffers from inter-code interference because of the long delay spread. In both scenarios, the alpine and the urban one, HSDPA utilizes multiple transmit antennas much more efficiently than WiMAX. This is reflected in a much higher throughput gain of the MIMO system with respect to the corresponding SISO system.

The achievable throughput of HSDPA is found to be much larger than the one of WiMAX. This is because WiMAX sacrifices more system resources for pilots, training, and guard band carriers. In HSDPA, only a small portion of the transmit power is dedicated to the pilot signal. Although the achievable throughput shows a significant difference, it is interesting that the actually measured throughput of both systems is close to each other, as explained above. Thus, sacrificing many resources as system overhead does not necessarily imply a lower data throughput over the air interface.

The mutual information of the channel, calculated from the estimated channel coefficients of the WiMAX and the HSDPA transmissions, is approximately equal for both systems. The only difference is an SNR shift of about 0.7 dB. The reason for this SNR shift is the smaller signal bandwidth of HSDPA that leads to a larger SNR after receive filtering.

The comparison between mutual information and channel capacity shows that only small gains of at most 0.5 bit/s/Hz (at SNR = 0 dB) are possible in case of 2×2 MIMO transmission with cross polarized transmit antennas. If equally polarized transmit antennas are utilized at the transmitter, a gain of about 1 bit/s/Hz is observed for the alpine scenario. However, the utilization of two equally polarized transmit antennas is not feasible since it leads to both smaller mutual information and smaller channel capacity. In case of 4×4 MIMO transmission, always two transmit antennas have the same polarization. The gain due to optimum precoding at four transmit antennas is up to 2 bit/s/Hz depending on the SNR and the scenario measured.

5.2. Outlook

In December 2008, the 3GPP completed the specification of Release 8 that defines the so-called Long Term Evolution (LTE) system. The targets for downlink and uplink peak data rate requirements were set to 100 Mbit/s and 50 Mbit/s, when operating in a 20 MHz spectrum allocation [144]. In LTE, the first version already supports up to four transmit antennas. Initial performance evaluations show that the throughput of the LTE physical layer and MIMO enhanced HSDPA is approximately the same [145–149]. However, LTE has several other features of which the most important ones for future research (and realistic performance evaluations) are briefly explained below.

The LTE downlink transmission scheme is based on OFDMA which converts the wide-band frequency selective channel into multiple flat fading subchannels. The flat fading subchannels have the advantage that —even in the case of MIMO transmission— optimum receivers can be implemented with reasonable complexity, in contrast to HSDPA. OFDMA additionally allows for frequency domain scheduling, typically trying to assign only "good" subchannels to the individual users. This offers large throughput gains in the downlink due to multi-user diversity [150, 151]. A further feature of LTE is the X2-interface between base stations. This interface can be used for interference management with the goal of decreasing inter-cell interference. The standard only defines the messages exchanged between the base stations while the algorithms and the exact implementation of the interference mitigation remain vendor specific and are currently of great scientific interest, see for example [152–154].

During the last year, a MATLAB-based LTE physical layer downlink simulator was developed at the Institute of Communications and Radio Frequency Engineering, Vienna University of Technology [155, 156]. Using this simulator, a measurement-based performance evaluation of LTE can be carried out in an initial step similar to that done for WiMAX in this thesis (simply by transmitting all possible transmit data blocks over the same channel). However, since LTE also supports HARQ and many different MIMO modes with adaptive precoding, the mini-receiver approach used for the HSDPA performance evaluation is more suitable. For this approach, an analytical model of the physical layer (similar to the one for HSDPA [49]) has to be developed and verified. While it is quite straightforward to develop such a model for linear receivers, it is challenging for non-linear receivers as for example sphere decoding. Such a verified model of the LTE physical layer is also the basis for meaningful system level simulations.

As explained above, LTE was developed as a multi-user system. The multi-user scheduling in the base station modifies the channel statistics the individual users are experiencing. (For example, by serving a user only at subchannels with high SNR.) Since the channel statistics have a great impact on the receiver performance, multi-user scheduling has to be considered for a realistic performance evaluation. Since the effort of testbed measurements in which multiple users are simultaneously connected to a single base station is immense, the following method can be applied for such a measurement. Firstly, we measure a host of different receiver locations to calculate the corresponding user feedback values. Secondly, when performing the "real" throughput measurement at different receiver locations, the scheduler is not only provided with the current user feedback but also with the previously recorded feedback values of the other users. Although in this method only the performance of one user is actually measured, a realistic performance measurement of the single base station to user link can be carried out. If interference aware receivers are to be tested, the signals received from different base stations can be recorded in a first step (by actually repositioning the only base station we have) and then added in the digital domain during the actual measurement.

The X2 interface between base stations allows for managing the inter-cell interference. Directly measuring interference management algorithms requires the use of many testbed transmitters simultaneously. In order to decrease the hardware effort but still obtain meaningful results, the probably most realistic performance evaluation of such algorithms is to first successively record the channels between several base stations and a single user. Later on, the measured channel coefficients can be used in the LTE physical layer simulator to investigate the interference management algorithms.

Appendix A.

Measurement Set-Up and Procedure

In this chapter, the MIMO WiMAX and MIMO HSDPA measurement set-ups in the alpine and the urban scenarios[1] are described and a histogram of the observed RMS delay spread is presented. Furthermore, an overview about the WiMAX and the HSDPA measurement procedures [95] utilizing the Vienna MIMO testbed [13, 14, 157–160] is given.

A.1. Measurement Set-Up

In both scenarios presented below, the transmit antennas were placed right next to existing base stations making the measurement results obtained very realistic and representative for a mobile communication system. In order to utilize polarization diversity, the first two transmitter outputs were connected to the different polarizations of the base station antenna. The third and fourth transmitter outputs (only relevant in the case of MIMO HSDPA transmissions) were connected to the same polarized antenna elements as the first and the second transmitter output. At the receiver, also differently polarized antenna elements were employed.

A.1.1. Alpine Scenario

In the alpine scenario, the base station antenna (Kathrein 800 10543 [161], [162, Appendix C], ±45° polarization, half-power beam width 58°/6.2°, down tilt 6°) was placed 5.7 km away from the RX unit which was located inside a house in a village on the opposite

---

[1]For both measured scenarios, the coordinates of the transmitter and the receiver locations can be downloaded in the Google Earth file format: `http://www.nt.tuwien.ac.at/fileadmin/data/testbed/` `Vienna-and-Carinthia-TX-RX-GPS.kmz`.
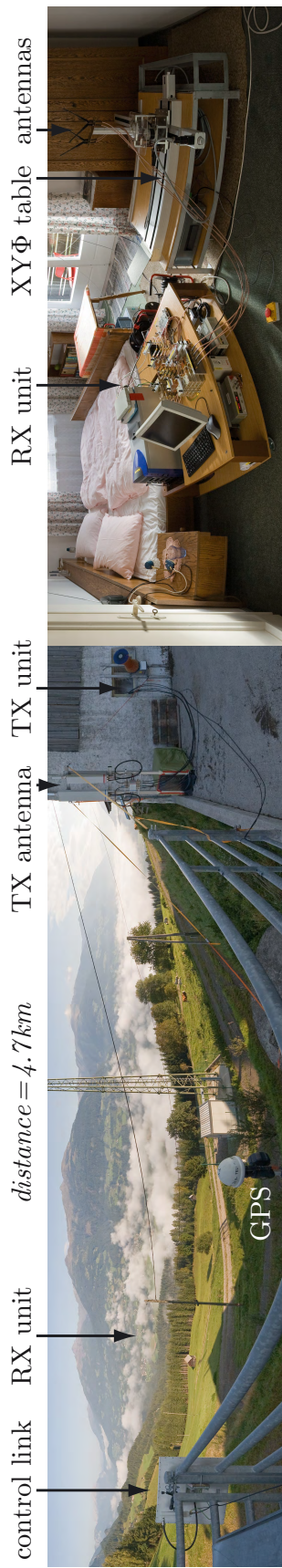
Figure A.1: Panoramic view of the alpine scenario measured (use PDF to zoom).

Figure A.2: Panoramic view of the urban scenario measured (use PDF to zoom).

side of the Drau valley as shown in Figure A.1. At the RX unit, standard Linksys WiFi-Router rod antennas were utilized. The results presented in Section 2.6.1 and Section 3.7.1 were obtained in a setup in the alpine scenario in which the receive antennas were placed indoors in non-line of sight to the transmitter. This set-up is characterized by a short mean RMS delay spread of about 1 chip (260 ns) and a single major propagation path because the receive signal was mainly propagating through one window facing the transmit antennas. Additionally to this set-up, RX antenna positions in different rooms where the TX antennas can and cannot be seen from the window were also investigated. The RX unit was also placed outside, in the middle of a field, with direct line-of-sight to the transmitter. In all measured set-ups, the results obtained did not change significantly, apart from a variation in the average path loss that only shifts the throughput curves to the left and right.

A.1.2. Urban Scenario

In the urban scenario, the same base station antenna (Kathrein 800 10543 [161], [162, Appendix C], ±45° polarization, half-power beam width 58°/6.2°, down tilt 6°) was placed on the roof of a big building in the center of Vienna, Austria, 430 m away from the RX unit that was placed inside an office room (see Figure A.2). At the RX unit, four low-cost printed monopole antennas [163] which are based on the generalized Koch pre-fractal curve were utilized. Due to their low cost and small size, such antennas are very realistic and could be build into a mobile handset or a laptop computer. The results presented in Section 2.6.2 and Section 3.7.2 were obtained in a setup in the urban scenario where the direct path from the TX to the RX antennas was blocked by the building the RX unit was located in. This scenario is characterized by a rather long mean RMS delay spread of about 4.3 chips (1.1 µs).

A.1.3. Delay Spreads of the Measured Scenarios

In order to characterize the multi-path propagation in the alpine and the urban scenario, the RMS delay spread was calculated using the time-domain channel estimate obtained in the HSDPA receiver. Usually, the RMS delay spread calculation is based on the Power Delay Profile (PDP) of the channel. Since the impulse responses measured with the testbed are not perfectly aligned in time, the PDP cannot be calculated and also the standard definition of the RMS delay spread cannot be evaluated directly. Therefore, the definition of the RMS delay spread was modified, as explained below.
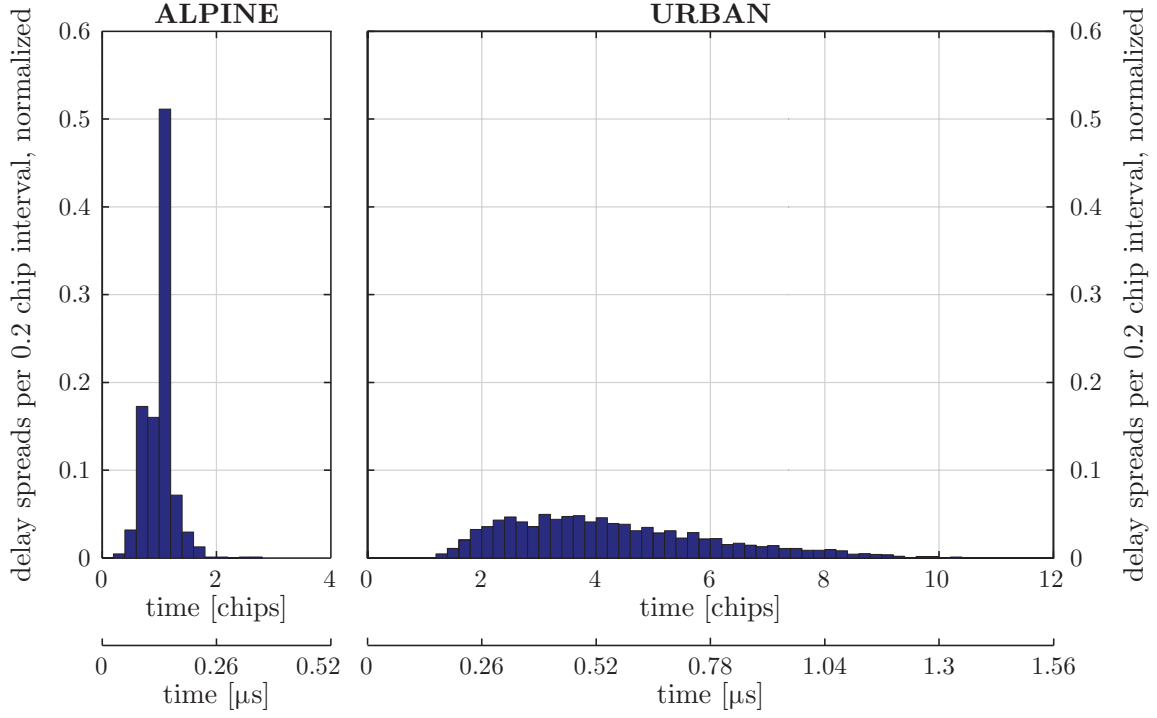
Figure A.3: Distribution of the RMS delay spreads in the alpine (ID "2008-09-16") and the urban scenario (ID "2008-12-12"). Normalized to the total number $N_\mathrm{R} N_\mathrm{T} N_\mathrm{CH}$ of SISO channel realizations. One chip corresponds to 260 ns.

Consider the complex channel gains $h_m^{(n_\mathrm{r},n_\mathrm{t},n_\mathrm{ch})}$ at tap delay $m = 0 \ldots L_\mathrm{h} - 1$, channel realization $n_\mathrm{ch} = 1 \ldots N_\mathrm{CH}$, transmit antenna $n_\mathrm{t} = 1 \ldots N_\mathrm{T}$, and receive antenna $n_\mathrm{r} = 1 \ldots N_\mathrm{R}$. The power $P^{(n_\mathrm{r},n_\mathrm{t},n_\mathrm{ch})}$ of this impulse response is calculated as

$$P^{(n_\mathrm{r},n_\mathrm{t},n_\mathrm{ch})} = \sum_{m=0}^{L_\mathrm{h}-1} \left| h_m^{(n_\mathrm{r},n_\mathrm{t},n_\mathrm{ch})} \right|^2, \tag{A.1}$$

the mean delay as

$$\tau_\mathrm{mean}^{(n_\mathrm{r},n_\mathrm{t},n_\mathrm{ch})} = \frac{1}{P^{(n_\mathrm{r},n_\mathrm{t},n_\mathrm{ch})}} \sum_{m=0}^{L_\mathrm{h}-1} \left| h_m^{(n_\mathrm{r},n_\mathrm{t},n_\mathrm{ch})} \right|^2 m, \tag{A.2}$$

and the RMS delay spread as

$$\tau_\mathrm{RMS}^{(n_\mathrm{r},n_\mathrm{t},n_\mathrm{ch})} = \sqrt{ \frac{1}{P^{(n_\mathrm{r},n_\mathrm{t},n_\mathrm{ch})}} \sum_{m=0}^{L_\mathrm{h}-1} \left| h_m^{(n_\mathrm{r},n_\mathrm{t},n_\mathrm{ch})} \right|^2 m^2 - \left(\tau_\mathrm{mean}^{(n_\mathrm{r},n_\mathrm{t},n_\mathrm{ch})} \right)^2 }. \tag{A.3}$$

By calculating the RMS delay spread in this way, one value for $\tau_\mathrm{RMS}^{(n_\mathrm{r},n_\mathrm{t},n_\mathrm{ch})}$ is obtained for every SISO channel realization. Thus, a total number of $N_\mathrm{R} N_\mathrm{T} N_\mathrm{CH}$ (with N_CH denoting

the number of channel realizations) values for $\tau_{\mathrm{RMS}}^{(n_{\mathrm{r}},n_{\mathrm{t}},n_{\mathrm{ch}})}$ is calculated. The distribution of $\tau_{\mathrm{RMS}}^{(n_{\mathrm{r}},n_{\mathrm{t}},n_{\mathrm{ch}})}$ in the alpine and the urban scenario is plotted in Figure A.3 as a normalized histogram.

To quantify the time dispersion of one scenario using a single value, the mean RMS delay spread is defined by averaging over the antennas and the channel realizations:

$$\tau_{\mathrm{RMS}} = \frac{1}{N_{\mathrm{R}}N_{\mathrm{T}}N_{\mathrm{CH}}} \sum_{n_{\mathrm{r}}=1}^{N_{\mathrm{R}}} \sum_{n_{\mathrm{t}}=1}^{N_{\mathrm{T}}} \sum_{n_{\mathrm{ch}}=1}^{N_{\mathrm{CH}}} \tau_{\mathrm{RMS}}^{(n_{\mathrm{r}},n_{\mathrm{t}},n_{\mathrm{ch}})}. \tag{A.4}$$

The evaluation of τ_{RMS} yields 1 chip (260 ns) in the alpine scenario and 4.3 chips (1.1 µs) in the urban scenario.

A.2. Measurement Procedure

Figure A.4 shows the basic measurement set-up used for all our measurements. A detailed explanation of this set-up and the measurements procedures can be found in [95, 162]. In the next two sections, the transmission of one data block is explained for the case of HSDPA and WiMAX, respectively. After that, the procedure for obtaining average throughput results for one scenario is explained.
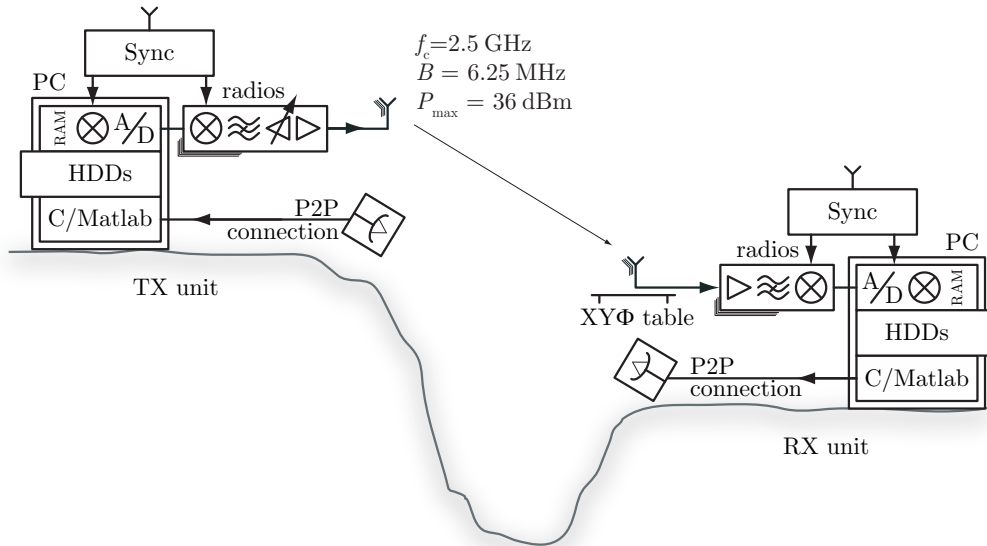

Figure A.4: Measurement set-up.

A.2.1. HSDPA

In case of HSDPA, the transmission of a "single" data block using the Vienna MIMO testbed works as explained below (see also Figure A.5). The required time for each operation is provided in parentheses at the end of each paragraph.

- At first, the RX unit (the master) requests the transmission of a "previous-block" via the control link. (HSDPA requires the receiver to feed back information calculated from the previously received block in order to transmit a channel adapted signal.) *(3 ms)*

- Then, the transmitter copies the selected block (that is, pre-generated transmit data samples) from solid state hard disks to the FIFOs of the transmit hardware. *(9 ms)*

- Next, via the control link, the TX unit tells the RX unit the exact time the following transmission will take place—that is, current time plus 4 ms. (The delay of the control link is typically less than 4 ms.) Another 4 ms are required for the handshaking between PC and external synchronization hardware. *(8 ms)*

- Consequently, at exactly the same time, the transmission and the reception of a data block is triggered by the TX and the RX hardware.

- In real-time, the transmit data samples are interpolated to 200 MSamples/s, digitally upconverted to 70 MHz, converted to the analog domain (14 bit), analog upconverted to 2.5 GHz, attenuated (digitally adjustable), amplified, and then transmitted. At the receiver, exactly the reverse procedure takes place. At the end, the already downsampled received complex baseband data samples are stored in the internal memory of the RX unit (not on the hard disks). *(5 ms)*

- These received samples are now immediately evaluated by the CPU of the RX computer, that is, synchronization, channel estimation, and feedback calculation like explained in Section 3.5 is carried out in MATLAB [49]. No further receiver processing is performed at this point. *($N_\mathrm{R} \times 26$ ms)*

- Now the RX unit requests the transmission of the actual channel-adapted data block via the control link (its index is determined by the feedback information calculated from the previous data block). Since a realistic performance evaluation of HSDPA requires to take HARQ retransmissions into account, the RX unit always requests the transmission of the two possible "retransmission data blocks" no matter if they are required or not. This is necessary because the data evaluation and the determination
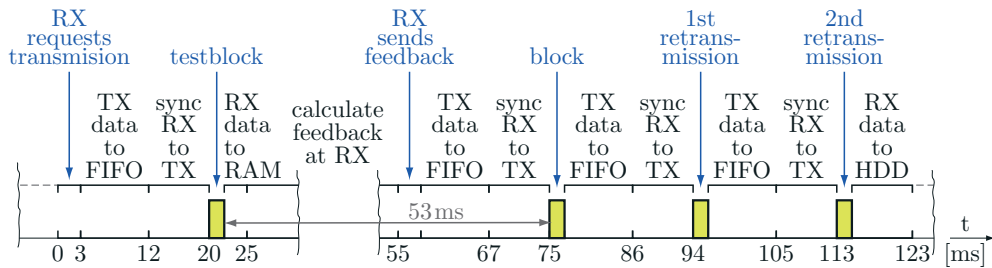
Figure A.5: Timing of the transmission of a "single" HSDPA data block.

of the required number of retransmissions is carried out later on. *(3 ms)*

- Transmission now takes place in real-time (as described above). *(57 ms)*

- At last, all four received blocks are stored on RAID hard disks for later/immediate off-line evaluation[2] in a cluster. *(10 ms)*

In our measurement, a typical value for the feedback delay between the "previous-block" used for channel sounding and the actual transmission of the first channel-adapted data block is 53 ms, as shown in Figure A.5. The actual time value depends on the MIMO HSDPA scheme under investigation. In a real HSDPA network, this feedback delay is in the order of a few milliseconds (at a maximum 7.5 slots corresponding to 5 ms). Therefore, to obtain representative results, the measurement procedure requires the channel to remain constant during the feedback delay. Later off-line testing revealed that this is the case—that is, estimation of the feedback based on the "previous" blocks and the channel-adapted blocks did not show any significant difference. Note that the delays between the channel-adapted data block and the first and second retransmission are about the same as in a real HSDPA network, thus no further requirements on the measurement procedure are necessary.

---

[2]Usually the first blocks of a measurement is evaluated immediately in order to quickly discover possible flaws in the measurement set-up (for example power amplifiers still turned off or wrong buttons on the equipment pushed by accident).

A.2.2. WiMAX

In the case of WiMAX, things are simpler because there are just seven possible feedback values, and therefore also only seven transmit blocks (in contrast to a few thousand for MIMO HSDPA). As shown in Figure A.6, all possible data blocks are transmitted one after the other without calculating any feedback information. As an advantage of this method, different methods for calculating the feedback and their impact on the throughput can be tried out later on without repeating the measurements. In addition, also all possible combinations of one, two, three, and four receive antennas can be evaluated later on from the same set of recorded data. The same holds true, for example, for trying different receiver types. In HSDPA, such investigations are only possible if the feedback (that has already been used to select the correct transmit data block) is not altered.
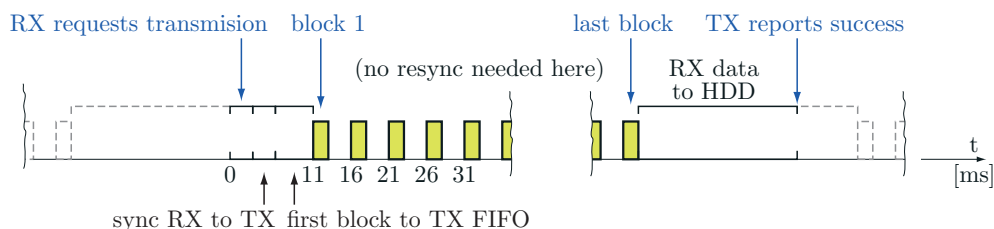

Figure A.6: Timing of the transmission of a "single" WiMAX data block.

A.2.3. Averaging Procedure

In the previous sections, the transmission of a "single" data block was explained in detail. The average throughput performance of a specific scenario is inferred by carrying out the following steps:

- The procedures explained in Sections A.2.1 and A.2.2 are repeated for all different schemes under investigation, for example different precoding schemes in the case of HSDPA or different space-time coding schemes in the case of WiMAX.

- Everything above is repeated for different transmit power levels. To achieve this, the transmit signal is attenuated prior to the power amplifier.

- Everything above is repeated for different receive antenna positions (typically a few hundred). They are created by moving the RX antennas using a fully automated XYΦ positioning table as shown in Figure A.1. To minimize large scale fading effects, uniformly distributed antenna positions within an area of $3\lambda \times 3\lambda$ are measured. Correlation between the different positions is minimized by this systematic sampling approach, maximizing the distance between all positions measured.

Measuring all this typically took from one hour up to a day. The evaluation of the data blocks (up to a terabyte of baseband data samples) is carried out employing a self programmed PC cluster software that parallelizes the off-line evaluation of the received data on a position-by-position basis on typically about 20 PCs.

- Once calculated, all results are collected from the cluster in order to average the throughput observed over the positions measured. Several tests are carried out in order to validate the results, for example, they are checked for measurement outliers or interference that should not exist.

- By measuring the output powers of all transmitters with a spectrum analyzer (Rohde and Schwarz FSQ26, relative accuracy ± 0.1 dB), we ensured that our individual power adjustment done in the digital domain resulted in identical output powers. Nevertheless, we observed that the average receive powers originating from the individual transmit antennas differ by about 1-2 dB [138, 164]. To compensate for this effect when comparing HSDPA schemes with different number of transmit antennas, we thus perform throughput averaging over the corresponding transmit/receive antennas. For example, if the 2×2 D-TxAA system is compared to the SISO transmission, the SISO throughput is obtained by averaging over the four individual SISO links (TX1→RX1, TX1→RX2, TX2→RX1, and TX2→RX2).

- Finally, the precision of the measurement is estimated by means of bootstrapping methods [165]. In all throughput graphs, the dots represent the inferred mean throughputs, the vertical lines the corresponding 95% confidence intervals, and the corresponding horizontal lines the 2.5% and 97.5% percentiles. Note that the RX antenna positions remained unchanged between measuring different schemes at different transmit power levels. This leads to smooth curves and *relative* positions that are more accurate than the confidence intervals for the *absolute* positions might suggest.

Appendix B.

Basics of LMMSE Estimation

This appendix provides an overview about LMMSE estimation [166] that is utilized by various signal processing algorithms like for example channel estimation (Sections 2.3.1 and 3.3.1) or channel equalization (Section 3.3.2). Consider the statistical dependent vectors $\mathbf{x}$ and $\mathbf{y}$. By observing the vector $\mathbf{y}$, a linear estimate $\hat{\mathbf{x}}$ for $\mathbf{x}$ can be obtained using the relation $\hat{\mathbf{x}} = \mathbf{K}\mathbf{y}$. In case of LMMSE estimation, the matrix $\mathbf{K}$ is calculated by minimizing the quadratic estimation error

$$\mathbf{J}(\mathbf{K}) = \min_{\mathbf{K}} \mathbb{E}_{\mathbf{xy}}\left\{ (\mathbf{x} - \hat{\mathbf{x}})\,(\mathbf{x} - \hat{\mathbf{x}})^{\mathrm{H}} \right\} = \min_{\mathbf{K}} \mathbb{E}_{\mathbf{xy}}\left\{ (\mathbf{x} - \mathbf{K}\mathbf{y})\,(\mathbf{x} - \mathbf{K}\mathbf{y})^{\mathrm{H}} \right\}. \tag{B.1}$$

Evaluating the expectation operator by using $\mathbf{R}_{\mathbf{xx}} = \mathbb{E}_{\mathbf{x}}\{\mathbf{x}\mathbf{x}^{\mathrm{H}}\}$, $\mathbf{R}_{\mathbf{yy}} = \mathbb{E}_{\mathbf{y}}\{\mathbf{y}\mathbf{y}^{\mathrm{H}}\}$, and $\mathbf{R}_{\mathbf{xy}} = \mathbb{E}_{\mathbf{x,y}}\{\mathbf{x}\mathbf{y}^{\mathrm{H}}\} = \mathbf{R}_{\mathbf{yx}}^{\mathrm{H}}$ yields

$$\mathbf{J}(\mathbf{K}) = \mathbf{R}_{\mathbf{xx}} - \mathbf{R}_{\mathbf{xy}}\mathbf{K}^{\mathrm{H}} - \mathbf{K}\mathbf{R}_{\mathbf{yx}} + \mathbf{K}\mathbf{R}_{\mathbf{yy}}\mathbf{K}^{\mathrm{H}}. \tag{B.2}$$

The expression $\mathbf{J}(\mathbf{K})$ can be minimized by extending it to a quadratic form

$$\mathbf{J}(\mathbf{K}) = \mathbf{K}\mathbf{R}_{\mathbf{yy}}\mathbf{K}^{\mathrm{H}} - \mathbf{R}_{\mathbf{xy}}\mathbf{K}^{\mathrm{H}} - \mathbf{K}\mathbf{R}_{\mathbf{xy}}^{\mathrm{H}} + \mathbf{R}_{\mathbf{xy}}\mathbf{R}_{\mathbf{yy}}^{-1}\mathbf{R}_{\mathbf{xy}}^{\mathrm{H}} - \mathbf{R}_{\mathbf{xy}}\mathbf{R}_{\mathbf{yy}}^{-1}\mathbf{R}_{\mathbf{xy}}^{\mathrm{H}} + \mathbf{R}_{\mathbf{xx}} =$$

$$= \left(\mathbf{K} - \mathbf{R}_{\mathbf{xy}}\mathbf{R}_{\mathbf{yy}}^{-1}\right)\mathbf{R}_{\mathbf{yy}}\left(\mathbf{K} - \mathbf{R}_{\mathbf{xy}}\mathbf{R}_{\mathbf{yy}}^{-1}\right)^{\mathrm{H}} + \mathbf{R}_{\mathbf{xx}} - \mathbf{R}_{\mathbf{xy}}\mathbf{R}_{\mathbf{yy}}^{-1}\mathbf{R}_{\mathbf{xy}}^{\mathrm{H}}. \tag{B.3}$$

Since only the quadratic form in $\mathbf{J}(\mathbf{K})$ depends on the matrix $\mathbf{K}$, and also since the matrix $\mathbf{R}_{\mathbf{yy}}$ is positive definite, the minimum is achieved at $\mathbf{K} = \mathbf{R}_{\mathbf{xy}}\mathbf{R}_{\mathbf{yy}}^{-1}$. The LMMSE estimator for the length L_{x} vector $\mathbf{x}$ and its corresponding mean square error are thus given by

$$\hat{\mathbf{x}} = \mathbf{R}_{\mathbf{xy}}\mathbf{R}_{\mathbf{yy}}^{-1}\mathbf{y} \tag{B.4}$$

$$\mathrm{MSE} = \frac{1}{L_{\mathrm{x}}}\mathrm{trace}\left(\mathbf{R}_{\mathbf{xx}} - \mathbf{R}_{\mathbf{xy}}\mathbf{R}_{\mathbf{yy}}^{-1}\mathbf{R}_{\mathbf{xy}}^{\mathrm{H}}\right). \tag{B.5}$$

Appendix C.

List of Symbols

In the look-up tables shown below, the most important mathematical symbols used in the WiMAX and the HSDPA chapters are listed.

C.1. Common Symbols

$\mathbb{E}\{.\}$	expectation operator
n_r	receive antenna index
N_R	number of receive antennas
n_t	transmit antenna index
N_T	number of transmit antennas

C.2. WiMAX Symbols

b_l	l-th bit in the transmit symbol vector $\mathbf{x}$
$D_\mathrm{achievable}^{(m)}$	achievable throughput at transmit power attenuation m
$D_\mathrm{best,avg}^{(m)}$	throughput obtained with the "best AMC selection" scheme at transmit power attenuation m
$\mathbf{F}$	spectral smoothing filter used in the LMMSE and ALMMSE estimators for post-processing the LS channel estimate
f_s	sampling rate of the transmit signal (5.76 MHz)
G	ratio between cyclic prefix time and useful OFDM symbol time
$\mathbf{h}$	N×1 channel coefficients vector (over subcarriers)

$\hat{\mathbf{h}}^{\mathrm{LS}}$	LS channel estimate of $\mathbf{h}$ (over subcarriers)
$\hat{\mathbf{h}}^{\mathrm{LMMSE}}$	LMMSE channel estimate of $\mathbf{h}$ (over subcarriers)
$\hat{\mathbf{h}}^{\mathrm{ALMMSE}}$	ALMMSE channel estimate of $\mathbf{h}$ (over subcarriers)
$\mathbf{H}$	$N_{\mathrm{R}} \times N_{\mathrm{T}}$ MIMO channel matrix on one subcarrier
i	AMC index
$I^{(m)}$	average mutual information at transmit power attenuation m
k	subcarrier index
l	index of the bit b_l in the transmit symbol vector $\mathbf{x}$
L	number of training symbols within one sub-band of the ALMMSE estimator
$\mathrm{LLR}(\mathrm{b_l})$	LLR value of the bit b_l
m	sub-band index
M	number of sub-bands the total frequency range is partitioned into by the ALMMSE estimator
N	number of training symbols within one OFDM symbol
N_{data}	number of OFDM data symbols
N_{OFDM}	total number of OFDM symbols
N_{c}	number of channel realizations used to estimate the channel autocorrelation matrix $\mathbf{R_{hh}}$
$\mathbf{r}$	N$\times$1 receive symbol vector (over subcarriers)
$\mathbf{R_{hh}}$	auto-correlation matrix of the channel coefficients
$\hat{\mathbf{R}}_{\mathbf{hh}}$	estimate of $\mathbf{R_{hh}}$
$\mathbf{R_{hr}}$	cross-correlation matrix between the channel coefficients and the received signal
$\mathbf{R_{rr}}$	auto-correlation matrix of the received signal
σ_v^2	noise variance of the elements in $\mathbf{v}$
$\mathbf{T}$	N$\times$N diagonal training symbol matrix (over subcarriers)
$\mathbf{v}$	$N_{\mathrm{R}} \times 1$ received noise vector on one subcarrier
$\mathbf{w}$	N$\times$1 additive Gaussian noise vector (over subcarriers)
$\mathbf{x}$	$N_{\mathrm{T}} \times 1$ transmit symbol vector on one subcarrier
$\mathbf{y}$	$N_{\mathrm{R}} \times 1$ receive symbol vector on one subcarrier

C.3. HSDPA Symbols

a_k, $\mathbf{a}_k$, $\mathbf{A}_k$ spread data chip streams at time index k

$\tilde{\mathbf{a}}_k$ spread and scrambled data chip streams at time index k

b_k, $\mathbf{b}_k$, $\mathbf{B}_k$ spread control channel chip streams at time index k

c_k, $\mathbf{c}_k$, $\mathbf{C}_k$ synchronization channel chip streams at time index k

d_k, $\mathbf{d}_k$, $\mathbf{D}_k$ sum of the spread data and control channel chip streams at time index k

$\tilde{\mathbf{D}}_k$ sum of the spread data and control channel chip streams plus the descrambled synchronization channel chip streams at time index k

$D_{\text{achievable}}$ the achievable throughput, defined in Equation (3.58)

$\mathbf{e}_k$ unit vector with a single "one" at position k and "zeros" at all other positions

f_{s} chip rate of HSDPA (3.84 MHz)

$\mathbf{f}^{(n_{\text{s}})}$ equalizer coefficients for the n_{s}-th data stream

$\gamma_{\hat{\mathbf{H}}}^{(n_{\text{s}})}$ total deterministic interference occurring at the n_{s}-th equalizer output

$\gamma_{\mathbf{H}_\Delta}^{(n_{\text{s}})}$ total stochastic interference occurring at the n_{s}-th equalizer output

$\gamma_{a,\hat{\mathbf{H}}}^{(n_{\text{s}})}$ deterministic interference caused by the data chip streams at the n_{s}-th equalizer output

$\gamma_{a,\mathbf{H}_\Delta}^{(n_{\text{s}})}$ stochastic interference caused by the data chip streams at the n_{s}-th equalizer output

$\gamma_{p,\hat{\mathbf{H}}}^{(n_{\text{s}})}$ deterministic interference caused by the pilot chip streams at the n_{s}-th equalizer output

$\gamma_{p,\mathbf{H}_\Delta}^{(n_{\text{s}})}$ stochastic interference caused by the pilot chip streams at the n_{s}-th equalizer output

$\gamma_{\text{SCH},\hat{\mathbf{H}}}^{(n_{\text{s}})}$ deterministic interference caused by the synchronization and the control channel chip streams at the n_{s}-th equalizer output

$\gamma_{\text{SCH},\mathbf{H}_\Delta}^{(n_{\text{s}})}$ stochastic interference caused by the synchronization and the control channel chip streams at the n_{s}-th equalizer output

$\gamma_{\text{SCH},\hat{\mathbf{H}},\tau}^{(n_{\text{s}})}$ deterministic interference caused by the synchronization chip streams at delay $m = \tau$ at the n_{s}-th equalizer output

$\gamma_{\text{SCH},\mathbf{H}_\Delta,\tau}^{(n_{\text{s}})}$ stochastic interference caused by the synchronization chip streams at delay $m = \tau$ at the n_{s}-th equalizer output

$\mathbf{G}_q$ MIMO channel matrix of the q-th frequency bin, obtained by Fourier transforming the channel impulse response in Equation (3.57)

$h_m^{(n_{\text{t}},n_{\text{r}})}$ channel coefficient between transmit antenna n_{t} and receive antenna n_{r} at delay m

$\mathbf{h}_{\text{eff},a}^{(n_{\text{s}})}$ total impulse response (channel plus equalizer) as experienced by the n_{s}-th data chip stream $\mathbf{a}_k$

$\mathbf{h}_{\text{eff},p}^{(n_{\text{s}})}$	total impulse response (channel plus equalizer) as experienced by the pilot chip streams $\mathbf{p}_k$
$\mathbf{h}_{\text{eff},\text{SCH}}^{(n_{\text{s}})}$	total impulse response (channel plus equalizer) as experienced by the synchronization and control channel chip streams
$\tilde{\mathbf{H}}_m$	channel matrix at delay m, defined according to Equation (3.5)
$\hat{\mathbf{H}}$	estimated MIMO channel matrix
$\mathbf{H}$	MIMO channel matrix, defined according to Equation (3.7)
$\mathbf{H}_\Delta$	channel estimation error matrix
$\mathbf{I}$	identity matrix
I_{or}	received signal power of the serving base station
I_{oc}	received signal power of interfering base stations
k	time index (in chips)
L_{c}	number of chips for which the system model is written in matrix-vector notation
L_{f}	equalizer span (in chips)
L_{h}	channel length (in chips)
m	delay index (chip spaced)
MSE	MSE of the channel estimator employed
n	shift of the descrambling operation in the tap-wise LMMSE channel estimator (in chips)
n_{ch}	channel realization index
N_{CH}	number of channel realizations
n_{s}	data chip stream index
N_{s}	maximum number of spatial multiplexed data chip streams
p_k, $\mathbf{p}_k$, $\mathbf{P}_k$	spread pilot channel chip streams at time index k
P_{CPICH}	power assigned to the CPICH by the base station
$P_{\text{HS}-\text{PDSCH}}$	power assigned to the HS-PDSCH by the base station
P_{SCH}	power assigned to the SCH and the PCCPCH, respectively, by the base station
q	frequency index
$\mathbf{r}_{k,n}$	receive signal at time index k descrambled by the scrambling sequenced shifted by n chips
$\mathbf{R}_{\tilde{\mathbf{h}}_n \tilde{\mathbf{h}}_n}$	autocorrelation of the channel coefficients at delay n
$\mathbf{R}_{\tilde{\mathbf{h}}_n \mathbf{r}}$	cross correlation between the channel coefficients and the receive signal
$\mathbf{R}_{\mathbf{rr}}$	autocorrelation of the receive signal

$\mathbf{R_{ww}}$ autocorrelation of the descrambled noise and/or interference

$\mathbf{R}_{\sigma_r}$ diagonal matrix with the receive signal energy on the main diagonal

s_k, $\mathbf{S}_k$ scrambling sequence of the base station

τ delay of the equalized chip stream compared to the transmit chip stream

$\mathbf{T}_k$ training signal matrix used for channel estimation, for definition see Equation (3.12)

v_k, $\mathbf{v}_k$, $\mathbf{V}_k$ additive noise and/or interference at time index k

$\mathbf{w}_k$ descrambled noise and/or interference at time index k

$\mathbf{W}$ precoding matrix

x_k, $\mathbf{x}_k$, $\mathbf{X}_k$ transmit chip streams at time index k (without synchronization channel chip stream)

$\tilde{\mathbf{X}}$ descrambled transmit chip stream, for definition see Equation (3.12)

y_k, $\mathbf{y}_k$, $\mathbf{Y}_k$ receive chip streams at time index k

Appendix D.

Acronyms

3GPP   3rd Generation Partnership Project

ALMMSE   Approximate Linear Minimum Mean Square Error

AMC   Adaptive Modulation and Coding

AWGN   Additive White Gaussian Noise

BCJR   Bahl-Cocke-Jelinek-Raviv

BLER   Block Error Ratio

CDMA   Code Division Multiple Access

CPICH   Common Pilot Channel

CQI   Channel Quality Indicator

CRC   Cyclic redundancy check

CTC   Convolutional Turbo Code

CP   Cyclic Prefix

D-TxAA   Double Transmit Antenna Array

DSL   Digital Subscriber Line

EDGE   Enhanced Data Rates for GSM Evolution

FIFO   First In First Out

FFT   Fast Fourier Transform

GPRS	General Packet Radio Service
GSM	Global System for Mobile communications
HARQ	Hybrid Automated Repeat Request
HSCSD	High-Speed Circuit-Switched Data
HSDPA	High Speed Downlink Packet Access
HS-PDSCH	High Speed Physical Downlink Shared Channel
ICI	Inter Carrier Interference
IEEE	Institute of Electrical and Electronics Engineers
IFFT	Inverse Fast Fourier Transform
LDPC	Low Density Parity Check
LLR	Log-likelihood Ratio
LOS	Line-Of-Sight
LS	Least Squares
LMMSE	Linear Minimum Mean Square Error
LTE	Long Term Evolution
MAP	Maximum A-Posteriori
MIMO	Multiple Input Multiple Output
MSE	Mean Square Error
NLOS	Non-Line-Of-Sight
OFDM	Orthogonal Frequency Division Multiplexing
OFDMA	Orthogonal Frequency Division Multiple Access
PAM	Pulse Amplitude Modulation
PCCPCH	Primary Common Control Physical Channel

PCI	Precoding Control Indicator
PDP	Power Delay Profile
QAM	Quadrature Amplitude Modulation
RAID	Redundant Array of Inexpensive Disks
RAN	Radio Access Network
RMS	Root Mean Square
RRC	Root Raised Cosine
RS-CC	Reed-Solomon Convolutional Code
SC	Single Carrier
SCH	Synchronization Channel
SIMO	Single Input Multiple Output
SINR	Signal to Interference and Noise Ratio
SISO	Single Input Single Output
SMS	Short Message Service
SNR	Signal to Noise Ratio
TBS	Transport Block Size
TDMA	Time-Division Multiple Access
TxAA	Transmit Antenna Array
UE	User Equipment
UMTS	Universal Mobile Telecommunications System
WiMAX	Worldwide Inter-operability for Microwave Access
W-CDMA	Wideband Code Division Multiple Access

Appendix E.

Bibliography

[1] GSM World, "**Market data summary**."
http://www.gsmworld.com/newsroom/market-data/market_data_summary.htm

[2] T. Halonen, J. Romero, and J. Melero, *GSM, GPRS and EDGE Performance: Evolution Towards 3G/UMTS*, 2nd ed. John Wiley and Sons Ltd, 2003.

[3] 3GPP, "**Technical specification group services and system aspects; release 1999 specifications 3G TS 21.101 version 1.0.0**," Oct. 1999.
http://www.3gpp.org/ftp/Specs/html-info/21101.htm

[4] W. Webb and R. Steele, "**Variable rate QAM for mobile radio**," *IEEE Transactions on Communications*, vol. 43, no. 7, pp. 2223–2230, July 1995, doi: 10.1109/26.392965.
http://ieeexplore.ieee.org/stamp/stamp.jsp?arnumber=00392965

[5] IEEE, "**IEEE standard for local and metropolitan area networks; part 16: Air interface for fixed broadband wireless access systems, IEEE Std. 802.16-2004**," Oct. 2004.
http://standards.ieee.org/getieee802/download/802.16-2004.pdf

[6] S. M. Alamouti, "**A simple transmit diversity technique for wireless communications**," *IEEE Journal on Selected Areas in Communications*, vol. 16, no. 8, pp. 1451–1458, Oct. 1998.
http://ieeexplore.ieee.org/iel4/49/15739/00730453.pdf?tp=&arnumber=730453&isnumber=15739

[7] M. C. Jeruchim, P. Balaban, and K. S. Shanmugan, Eds., *Simulation of Communication Systems: Modeling, Methodology and Techniques*, 2nd ed. Springer, 2000.

[8] R. S. Thomä, D. Hampicke, A. Richter, G. Sommerkorn, and U. Trautwein, "**MIMO vector channel sounder measurement for smart antenna system evaluation**," *European Transactions on Telecommunications*, vol. 12, no. 5, pp. 427–438, 2001, doi: 10.1002/ett.4460120508.
http://www.channelsounder.de/papers/2001-002.pdf

[9] L. Hentilä, P. Kyösti, J. Ylitalo, X. Zhao, J. Meinilä, and J.-P. Nuutinen, "**Experimental characterization of multi-dimensional parameters at 2.45 and 5.25 GHz indoor channels**," in *Proc. International Symposium on Wireless Personal Multimedia Communication 2005 (WPMC 2005)*, pp. 254–258, Sept. 2005.

[10] J. P. Kermoal, L. Schumacher, K. I. Pedersen, P. E. Mogensen, and F. Frederiksen, "**A stochastic MIMO radio channel model with experimental validation**," *IEEE Journal on Selected Areas in Communications*, vol. 20, no. 6, pp. 1211–1226, Aug. 2002, doi: 10.1109/JSAC.2002.801223.
http://ieeexplore.ieee.org/stamp/stamp.jsp?tp=&arnumber=1021913

[11] C. Mehlführer, F. Kaltenberger, M. Rupp, and G. Humer, "**Low-complexity MIMO channel simulation by reducing the number of paths**," in *Proc. ITG/IEEE Workshop on Smart Antennas (WSA 2007)*, Vienna, Austria, Feb. 2007.
http://publik.tuwien.ac.at/files/pub-et_12315.pdf

[12] C. Mehlführer and M. Rupp, "**Approximation and resampling of tapped delay line channel models with guaranteed channel properties**," in *Proc. IEEE International Conference on Acoustics, Speech and Signal Processing (ICASSP 2008)*, pp. 2869–2872, Las Vegas, NV, USA, Mar. 2008, doi: 10.1109/ICASSP.2008.4518248.
http://publik.tuwien.ac.at/files/pub-et_13682.pdf

[13] S. Caban, C. Mehlführer, R. Langwieser, A. L. Scholtz, and M. Rupp, "**Vienna MIMO testbed**," *EURASIP Journal on Applied Signal Processing, Special Issue on Implementation Aspects and Testbeds for MIMO Systems*, vol. 2006, Article ID 54868, 2006, doi: 10.1155/ASP/2006/54868.
http://publik.tuwien.ac.at/files/pub-et_10929.pdf

[14] M. Rupp, S. Caban, and C. Mehlführer, "**Challenges in building MIMO testbeds**," in *Proc. 15th European Signal Processing Conference (EUSIPCO 2007)*, Poznań, Poland, Sept. 2007.
http://publik.tuwien.ac.at/files/PubDat_112138.pdf

[15] S. Caban, C. Mehlführer, L. W. Mayer, and M. Rupp, "**2x2 MIMO at variable antenna distances**," in *Proc. 67th IEEE Vehicular Technology Conference (VTC2008-Spring)*, pp. 1311–1315, Singapore, May 2008, doi: 10.1109/VETECS.2008.276.
http://publik.tuwien.ac.at/files/PubDat_167444.pdf

[16] S. Caban and M. Rupp, "**Impact of transmit antenna spacing on 2x1 Alamouti radio transmission**," *IEE Electronics Letters*, vol. 43, no. 4, pp. 198–199, Feb. 2007.
http://publik.tuwien.ac.at/files/pub-et_12278.pdf

[17] B. A. Jones and J. R. Cavallaro, "**A rapid prototyping environment for wireless communication embedded systems**," *EURASIP Journal on Applied Signal Processing*, vol. 2003, no. 6, pp. 603–614, 2003, doi: 10.1155/S111086570330304X.
http://www.hindawi.com/journals/asp/2003/187410.pdf

[18] C. Mehlführer, F. Kaltenberger, M. Rupp, and G. Humer, "**A scalable rapid prototyping system for real-time MIMO OFDM transmissions**," in *Proc. 2nd IEE/EURASIP Conference on DSP enabled Radio*, Southampton, UK, Sept. 2005.
http://publik.tuwien.ac.at/files/pub-et_10207.pdf

[19] K. Freudenthaler, F. Kaltenberger, S. Paul, C. F. Mecklenbräuker, M. Huemer, and A. Springer, "**Cancellation of interference from synchronization and pilot channels on high speed downlink shared channel in UMTS**," in *Proc. 11th European Wireless Conference*, Nicosia, Cyprus, Apr. 2005.

[20] C. Mehlführer and K. Freudenthaler, "**HSDPA simulator environment**," ftw., C10 project deliverable 1-5, Jan. 2007.

[21] C. Mehlführer and R. Tresch, "**HSDPA simulator environment**," ftw., C12 project deliverable 1-4, Dec. 2007.

[22] A. Roca, "**Implementation of a WiMAX simulator in simulink**," Master's thesis, Technische Universität Wien, Institut für Nachrichtentechnik und Hochfrequenztechnik, Feb. 2007, supervisors Christian Mehlführer and Markus Rupp.
http://publik.tuwien.ac.at/files/pub-et_12498.pdf

[23] "**WiMAX simulator homepage**."
http://www.nt.tuwien.ac.at/wimaxsimulator/

[24] Q. Wang, C. Mehlführer, and M. Rupp, "**SNR optimized residual frequency offset compensation for WiMAX with throughput evaluation**," in *Proc. 17th European Signal Processing Conference (EUSIPCO 2009)*, Glasgow, Scotland, UK, Aug. 2009.

[25] Q. Wang, S. Caban, C. Mehlführer, and M. Rupp, "**Measurement based throughput evaluation of residual frequency offset compensation in WiMAX**," in *Proc. 51st International Symposium ELMAR-2009*, Zadar, Croatia, Sept. 2009.

[26] C. Mehlführer, S. Caban, and M. Rupp, "**Experimental evaluation of adaptive modulation and coding in MIMO WiMAX with limited feedback**," *EURASIP Journal on Advances in Signal Processing, Special Issue on MIMO Systems with Limited Feedback*, vol. 2008, Article ID 837102, 2008, doi: 10.1155/2008/837102.
http://publik.tuwien.ac.at/files/pub-et_13762.pdf

[27] C. Mehlführer, S. Caban, and M. Rupp, "**An accurate and low complex channel estimator for OFDM WiMAX**," in *Proc. 3rd International Symposium on Communications, Control and Signal Processing (ISCCSP 2008)*, pp. 922–926, St. Julians, Malta, Mar. 2008, doi: 10.1109/ISCCSP.2008.4537355.
http://publik.tuwien.ac.at/files/pub-et_13650.pdf

[28] C. Mehlführer, S. Caban, J. A. G. Naya, and M. Rupp, "**Throughput and capacity of MIMO WiMAX**," in *Conference Record of the 43nd Asilomar Conference on Signals, Systems and Computers*, Pacific Grove, CA, USA, Nov. 2009, submitted.

[29] C. Hoymann, "**Analysis and performance evaluation of the OFDM-based metropolitan area network IEEE 802.16**," *Computer Networks*, vol. 49, no. 3, pp. 341–363, 2005, selected Papers from the European Wireless 2004 Conference, doi: 10.1016/j.comnet.2005.05.008.
http://www.sciencedirect.com/science/article/B6VRG-4GFV2CF-1/2/596ad98cbf6983056f15e3c7e95ef339

[30] M. A. Hasan, "**Performance evaluation of WiMax/IEEE 802.16 OFDM physical layer**," Master's thesis, Helsinki University of Technology, Department of Electrical and Communications Engineering, Communications Laboratory, June 2007.
http://lib.tkk.fi/Dipl/2007/urn009599.pdf

[31] I. Koffman and V. Roman, "**Broadband wireless access solutions based on OFDM access in IEEE 802.16**," *IEEE Communications Magazine*, vol. 40, no. 4, pp. 96–103, Apr. 2002, doi: 10.1109/35.995857.
http://ieeexplore.ieee.org/stamp/stamp.jsp?tp=&arnumber=995857

[32] C. Eklund, R. Marks, K. Stanwood, and S. Wang, "**IEEE standard 802.16: a technical overview of the WirelessMAN air interface for broadband wireless access**," *IEEE Communications Magazine*, vol. 40, no. 6, pp. 98–107, June 2002, doi: 10.1109/MCOM.2002.1007415.
http://ieeexplore.ieee.org/stamp/stamp.jsp?tp=&arnumber=1007415

[33] D.-H. Cho, J.-H. Song, M.-S. Kim, and K.-J. Han, "**Performance analysis of the IEEE 802.16 wireless metropolitan area network**," in *Proc. 1st International Conference on Distributed Frameworks for Multimedia Applications 2005 (DFMA 2005)*, pp. 130–136, Feb. 2005, doi: 10.1109/DFMA.2005.41.
http://ieeexplore.ieee.org/stamp/stamp.jsp?tp=&arnumber=1385193

[34] S. Ramachandran, C. Bostian, and S. Midkiff, "**A link adaptation algorithm for IEEE 802.16**," in *Proc. IEEE Wireless Communications and Networking Conference 2005 (WCNC 2005)*, vol. 3, pp. 1466–1471, Mar. 2005, doi: 10.1109/WCNC.2005.1424731.
http://ieeexplore.ieee.org/stamp/stamp.jsp?tp=&arnumber=1424731

[35] F. Wang, A. Ghosh, R. Love, K. Stewart, R. Ratasukt, R. Bachu, Y. Sun, and Q. Zhao, "**IEEE 802.16e system performance: analysis and simulations**," in *Proc. 16th IEEE International Symposium on Personal, Indoor and Mobile Radio Communications (PIMRC 2005)*, Berlin, Germany, Sept. 2005.
http://ieeexplore.ieee.org/iel5/10989/34627/01651572.pdf

[36] B. Muquet, E. Biglieri, and H. Sari, "**MIMO link adaptation in mobile WiMAX systems**," in *Proc. IEEE Wireless Communications and Networking Conference 2007 (WCNC 2007)*, Hong Kong, Mar. 2007.
http://ieeexplore.ieee.org/iel5/4204175/4224245/04224585.pdf

[37] T. H. Chan, C. Y. Cheung, M. Hamdi, and M. Ma, "**Overview of rate adaptation algorithms based on MIMO technology in WiMAX networks**," in *Proc. IEEE Mobile WiMAX Symposium 2007*, Orlando, FL, USA, Mar. 2007.
http://ieeexplore.ieee.org/iel5/4156078/4156079/04156103.pdf

[38] M. Malkowski, "**Link-level comparison of IP-OFDMA (mobile WiMAX) and UMTS HSDPA**," in *Proc. IEEE 18th International Symposium on Personal, Indoor and Mobile Radio Communications 2007 (PIMRC 2007)*, 2007, doi: 10.1109/PIMRC.2007.4394134.
http://ieeexplore.ieee.org/stamp/stamp.jsp?tp=&arnumber=4394134

[39] O. Grøndalen, P. Grønsund, T. Breivik, and P. Engelstad, "**Fixed WiMAX field trial measurements and analyses**," in *Proc. 16th IST Mobile and Wireless Communications Summit, 2007*, July 2007, doi: 10.1109/ISTMWC.2007.4299213.
http://ieeexplore.ieee.org/stamp/stamp.jsp?tp=&arnumber=4299213

[40] P. Grønsund, P. Engelstad, T. Johnsen, and T. Skeie, "**The physical performance and path loss in a fixed WiMAX deployment**," in *Proc. International Conference on Wireless Communications and Mobile Computing 2007 (IWCMC 2007)*, pp. 439–444, 2007, doi: http://doi.acm.org/10.1145/1280940.1281035.
http://portal.acm.org/ft_gateway.cfm?id=1281035

[41] N. Scalabrino, F. De Pellegrini, I. Chlamtac, A. Ghittino, and S. Pera, "**Performance evaluation of a WiMAX testbed under VoIP traffic**," in *Proc. 1st International Workshop on Wireless Network Testbeds, Experimental Evaluation & Characterization (WiNTECH 2006)*, pp. 97–98, 2006, doi: 10.1145/1160987.1161009.
http://portal.acm.org/ft_gateway.cfm?id=1161009

[42] N. Scalabrino, F. De Pellegrini, R. Riggio, A. Maestrini, C. Costa, and I. Chlamtac, "**Measuring the quality of VoIP traffic on a WiMAX testbed**," in *Proc. 3rd International Conference on Testbeds and Research Infrastructure for the Development of Networks and Communities (TridentCom 2007)*, May 2007, doi: 10.1109/TRIDENTCOM.2007.4444719.
http://ieeexplore.ieee.org/stamp/stamp.jsp?tp=&arnumber=4444719

[43] K. Pentikousis, J. Pinola, E. Piri, and F. Fitzek, "**An experimental investigation of VoIP and video streaming over fixed WiMAX**," in *Proc. 6th International Symposium on Modeling and Optimization in Mobile, Ad Hoc, and Wireless Networks and Workshops 2008 (WiOPT 2008)*, pp. 8–15, Apr. 2008, doi: 10.1109/WIOPT.2008.4586026.
http://ieeexplore.ieee.org/stamp/stamp.jsp?tp=&arnumber=4586026

[44] A. Durantini, M. Petracca, and F. Ananasso, "**Experimental evaluation of IEEE 802.16 WiMAX performances at 2.5 GHz band**," in *Proc. International Wireless Communications and Mobile Computing Conference 2008 (IWCMC 2008)*, pp. 338–343, Aug. 2008, doi: 10.1109/IWCMC.2008.59.
http://ieeexplore.ieee.org/stamp/stamp.jsp?arnumber=04599958

[45] H. Sampath, S. Talwar, J. Tellado, V. Erceg, and A. Paulraj, "**A fourth-generation MIMO-OFDM broadband wireless system: design, performance, and field trial results**," *IEEE Communications Magazine*, vol. 40, no. 9, pp. 143–149, Sept. 2002, doi: 10.1109/MCOM.2002.1031841.
http://ieeexplore.ieee.org/stamp/stamp.jsp?tp=&arnumber=1031841

[46] C. Mehlführer, S. Caban, and M. Rupp, "**MIMO HSDPA throughput measurement results**," *IEEE Transactions on Vehicular Technology*, to be submitted.

[47] C. Mehlführer, S. Caban, and M. Rupp, "**MIMO HSDPA throughput measurement results**," in *HSDPA/HSUPA Handbook*, B. Furht and S. Ahson, Eds. CRC Press, 2009, submitted.

[48] C. Mehlführer, S. Caban, and M. Rupp, "**MIMO HSDPA throughput measurement results in an urban scenario**," in *Proc. 70th IEEE Vehicular Technology Conference (VTC2009-Fall)*, Anchorage, AK, USA, Sept. 2009.
http://publik.tuwien.ac.at/files/PubDat_176321.pdf

[49] C. Mehlführer, S. Caban, M. Wrulich, and M. Rupp, "**Joint throughput optimized CQI and precoding weight calculation for MIMO HSDPA**," in *Conference Record of the 42nd Asilomar Conference on Signals, Systems and Computers*, pp. 1320–1325, Pacific Grove, CA, USA, Oct. 2008, doi: 10.1109/ACSSC.2008.5074632.
http://publik.tuwien.ac.at/files/PubDat_167015.pdf

[50] C. Mehlführer and M. Rupp, "**Novel tap-wise LMMSE channel estimation for MIMO W-CDMA**," in *Proc. 51st IEEE Global Telecommunications Conference 2008 (GLOBECOM 2008)*, New Orleans, LA, USA, Nov. 2008, doi: 10.1109/GLOCOM.2008.ECP.829.
http://publik.tuwien.ac.at/files/PubDat_169129.pdf

[51] C. Mehlführer, L. Mayer, R. Langwieser, A. L. Scholtz, and M. Rupp, "**Free space experiments with MIMO UMTS high speed downlink packet access**," in *Proc. 2nd IEE/EURASIP Conference on DSP enabled Radio*, Southampton, UK, Sept. 2005.
http://publik.tuwien.ac.at/files/pub-et_10206.pdf

[52] C. Mehlführer, C. F. Mecklenbräuker, and M. Rupp, "**Double space-time transmit diversity with subgroup rate control for UMTS: Throughput analysis**," in *Conference Record of the 39th Asilomar Conference on Signals, Systems and Computers*, pp. 1258–1262, Pacific Grove, CA, USA, Nov. 2005.
http://publik.tuwien.ac.at/files/pub-et_10265.pdf

[53] C. Mehlführer, S. Caban, M. Rupp, and A. L. Scholtz, "**Effect of transmit and receive antenna configuration on the throughput of MIMO UMTS downlink**," in *Proc. 8th International Symposium on DSP and Communication Systems 2005 (DSPCS 2005)*, Noosa Heads, Australia, Dec. 2005.
http://publik.tuwien.ac.at/files/pub-et_10269.pdf

[54] C. Mehlführer, C. F. Mecklenbräuker, and M. Rupp, "**On reduced-complexity variants to the double space-time transmit diversity proposal for UMTS**," in *Proc. 2nd International Symposium on Communications, Control and Signal Processing 2006 (ISCCSP 2006)*, Marrakech, Morocco, Mar. 2006.
http://publik.tuwien.ac.at/files/pub-et_11011.pdf

[55] C. Mehlführer, D. Seethaler, G. Matz, and M. Rupp, "**An iterative MIMO-HSDPA receiver based on a K-Best-MAP algorithm**," in *Proc. 49th IEEE Global Telecommunications Conference 2006 (GLOBECOM 2006)*, San Francisco, CA, USA, Nov. 2006, doi: 10.1109/GLOCOM.2006.535.
http://publik.tuwien.ac.at/files/pub-et_11722.pdf

[56] D. Bosanska, C. Mehlführer, and M. Rupp, "**Performance evaluation of intra-cell interference cancelation in D-TxAA HSDPA**," in *Proc. International ITG Workshop on Smart Antennas (WSA 2008)*, pp. 338–342, Darmstadt, Germany, Feb. 2008, doi: 10.1109/WSA.2008.4475579.
http://publik.tuwien.ac.at/files/pub-et_13677.pdf

[57] C. Mehlführer, "**Iterative PARC MMSE equalizer**," ftw., C10 project deliverable 1-3a, Jan. 2007.

[58] C. Mehlführer, R. Tresch, and M. Guillaud, "**Channel estimation in MIMO HSDPA**," ftw., C12 project deliverable 1-1, Mar. 2008.

[59] D. Bosanska and C. Mehlführer, "**Intra-cell interference cancelation receiver for D-TxAA HSDPA**," ftw., C12 project deliverable 1-2, Mar. 2008.

[60] M. Wrulich and M. Rupp, "**Computationally efficient MIMO HSDPA system-level modeling**," *EURASIP Journal on Wireless Communications and Networking*, 2009.

[61] M. Wrulich, S. Eder, I. Viering, and M. Rupp, "**Efficient link-to-system level model for MIMO HSDPA**," in *Proc. 4th IEEE Broadband Wireless Access Workshop*, 2008.
http://publik.tuwien.ac.at/files/PubDat_170334.pdf

[62] M. Wrulich, W. Weiler, and M. Rupp, "**HSDPA performance in a mixed traffic network**," in *Proc. 67th IEEE Vehicular Technology Conference Spring (VTC2008-Spring)*, pp. 2056–2060, Singapore, May 2008.
http://publik.tuwien.ac.at/files/pub-et_13769.pdf

[63] M. Wrulich and M. Rupp, "**Efficient link measurement model for system level simulations of Alamouti encoded MIMO HSDPA transmissions**," in *Proc. ITG International Workshop on Smart Antennas (WSA 2008)*, Darmstadt, Germany, Feb. 2008.
http://publik.tuwien.ac.at/files/pub-et_13641.pdf

[64] T. E. Kolding, K. I. Pedersen, J. Wigard, F. Frederiksen, and P. E. Mogensen, "**High speed downlink packet access: WCDMA evolution**," *IEEE Vehicular Technology Society News*, pp. 4–10, Feb. 2003.
http://kom.aau.dk/group/05gr943/literature/hsdpa/evolution%20of%20HSDPA.pdf

[65] S. Parkvall, E. Dahlman, P. Frenger, P. Beming, and M. Persson, "**The evolution of WCDMA towards higher speed downlink packet data access**," in *Proc. 53rd IEEE Vehicular Technology Conference 2001 (VTC2001-Spring)*, vol. 3, pp. 2287–2291, 2001, doi: 10.1109/VETECS.2001.945103.
http://ieeexplore.ieee.org/stamp/stamp.jsp?arnumber=945103

[66] S. Parkvall, E. Dahlman, P. Frenger, P. Beming, and M. Persson, "**The high speed packet data evolution of WCDMA**," in *Proc. 12th IEEE International Symposium on Personal, Indoor and Mobile Radio Communications 2001 (PIMRC 2001)*, vol. 2, Sept. 2001, doi: 10.1109/PIMRC.2001.965315.
http://ieeexplore.ieee.org/stamp/stamp.jsp?arnumber=965315

[67] T. Moulsley, "**Throughput of high speed downlink packet access for UMTS**," in *Proc. 2nd IEE International Conference on 3G Mobile Communication Technologies 2001 (3G 2001)*, pp. 363–367, 2001.
http://ieeexplore.ieee.org/stamp/stamp.jsp?arnumber=923569

[68] A. Das, F. Khan, A. Sampath, and H.-J. Su, "**Performance of hybrid ARQ for high speed downlink packet access in UMTS**," in *Proc. 54th IEEE Vehicular Technology Conference 2001 (VTC2001-Fall)*, vol. 4, pp. 2133–2137, 2001, doi: 10.1109/VTC.2001.957121.
http://ieeexplore.ieee.org/stamp/stamp.jsp?arnumber=957121

[69] T. Kolding, F. Frederiksen, and P. Mogensen, "**Performance aspects of WCDMA systems with high speed downlink packet access (HSDPA)**," in *Proc. 56th IEEE Vehicular Technology Conference 2002 (VTC2002-Fall)*, vol. 1, pp. 477–481, 2002, doi: 10.1109/VETECF.2002.1040389.
http://ieeexplore.ieee.org/stamp/stamp.jsp?arnumber=1040389

[70] R. Love, A. Ghosh, R. Nikides, L. Jalloul, M. Cudak, and B. Classon, "**High speed downlink packet access performance**," in *Proc. 53rd IEEE Vehicular Technology Conference 2001 (VTC2001-Spring)*, vol. 3, pp. 2234–2238, 2001, doi: 10.1109/VETECS.2001.945093.
http://ieeexplore.ieee.org/stamp/stamp.jsp?arnumber=945093

[71] R. Love, A. Ghosh, W. Xiao, and R. Ratasuk, "**Performance of 3GPP high speed downlink packet access (HSDPA)**," in *Proc. IEEE 60th Vehicular Technology Conference (VTC 2004-Fall)*, vol. 5, pp. 3359–3363, Sept. 2004, doi: 10.1109/VETECF.2004.1404686.
http://ieeexplore.ieee.org/stamp/stamp.jsp?tp=&arnumber=1404686

[72] K. Pedersen, T. Lootsma, M. Støttrup, F. Frederiksen, T. Kolding, and P. Mogensen, "**Network performance of mixed traffic on high speed downlink packet access and dedicated channels in WCDMA**," in *Proc. IEEE 60th Vehicular Technology Conference (VTC 2004-Fall)*, vol. 6, pp. 4496–4500, Sept. 2004, doi: 10.1109/VETECF.2004.1404930.
http://ieeexplore.ieee.org/stamp/stamp.jsp?tp=&arnumber=1404930

[73] I. Siomina and D. Yuan, "**Enhancing HSDPA performance via automated and large-scale optimization of radio base station antenna configuration**," in *Proc. 67th IEEE Vehicular Technology Conference (VTC2008-Spring)*, pp. 2061–2065, May 2008, doi: 10.1109/VETECS.2008.463.
http://ieeexplore.ieee.org/stamp/stamp.jsp?tp=&arnumber=4526019

[74] M. Assaad and D. Zeghlache, "**On the capacity of HSDPA**," in *Proc. 46th IEEE Global Telecommunications Conference 2003 (GLOBECOM 2003)*, vol. 1, pp. 60–64, Dec. 2003, doi: 10.1109/GLOCOM.2003.1258203.
http://ieeexplore.ieee.org/stamp/stamp.jsp?arnumber=1258203

[75] M. Assaad and D. Zeghlache, "**Comparison between MIMO techniques in UMTS-HSDPA system**," in *Proc. 8th IEEE International Symposium on Spread Spectrum Techniques and Applications 2004*, pp. 874–878, Aug. 2004.
http://ieeexplore.ieee.org/stamp/stamp.jsp?arnumber=1371826

[76] J. Kunze, C. Schmits, A. Bilgic, and J. Hausner, "**Receive antenna diversity architectures for HSDPA**," in *Proc. 67th IEEE Vehicular Technology Conference (VTC2008-Spring)*, pp. 2071–2075, May 2008, doi: 10.1109/VETECS.2008.465.
http://ieeexplore.ieee.org/stamp/stamp.jsp?tp=&arnumber=4526021

[77] R. Love, K. Stewart, R. Bachu, and A. Ghosh, "**MMSE equalization for UMTS HSDPA**," in *Proc. IEEE 58th Vehicular Technology Conference (VTC 2003-Fall)*, vol. 4, pp. 2416–2420, Oct. 2003, doi: 10.1109/VETECF.2003.1285963.
http://ieeexplore.ieee.org/stamp/stamp.jsp?tp=&arnumber=1285963

[78] M. Heikkila and K. Majonen, "**Increasing HSDPA throughput by employing space-time equalization**," in *Proc. 15th IEEE International Symposium on Personal, Indoor and Mobile Radio Communications (PIMRC 2004)*, vol. 4, pp. 2328–2332, Sept. 2004.
http://ieeexplore.ieee.org/stamp/stamp.jsp?tp=&arnumber=1368735

[79] R. Stuhlberger, L. Maurer, G. Hueber, and A. Springer, "**The impact of RF-impairments and automatic gain control on UMTS-HSDPA-throughput performance**," in *Proc. IEEE 64th Vehicular Technology Conference (VTC 2006-Fall)*, Sept. 2006, doi: 10.1109/VTCF.2006.389.
http://ieeexplore.ieee.org/stamp/stamp.jsp?tp=&arnumber=4109654

[80] M. Nakamura, Y. Awad, and S. Vadgama, "**Adaptive control of link adaptation for high speed downlink packet access (HSDPA) in W-CDMA**," in *Proc. 5th International Symposium on Wireless Personal Multimedia Communications 2002*, vol. 2, pp. 382–386, Oct. 2002, doi: 10.1109/WPMC.2002.1088198.
http://ieeexplore.ieee.org/stamp/stamp.jsp?arnumber=1088198

[81] J.-B. Landre and A. Saadani, "**Hsdpa 14,4 mbps mobiles - realistic throughputs evaluation**," in *Proc. 67th IEEE Vehicular Technology Conference 2008 (VTC2008-Spring)*, pp. 2086–2090, May 2008, doi: 10.1109/VETECS.2008.468.
http://ieeexplore.ieee.org/stamp/stamp.jsp?arnumber=4526024

[82] D. Samardzija, A. Lozano, and C. Papadias, "**Experimental validation of MIMO multiuser detection for UMTS high-speed downlink packet access**," in *Proc. 47th IEEE Global Telecommunications Conference 2004 (GLOBECOM 2004)*, vol. 6, pp. 3840–3844, Nov. 2004, doi: 10.1109/GLOCOM.2004.1379087.
http://ieeexplore.ieee.org/stamp/stamp.jsp?arnumber=1379087

[83] T. Isotalo and J. Lempiäinen, "**HSDPA measurements for indoor DAS**," in *Proc. 65th IEEE Vehicular Technology Conference 2007 (VTC2007-Spring)*, pp. 1127–1130, Apr. 2007, doi: 10.1109/VETECS.2007.239.
http://ieeexplore.ieee.org/stamp/stamp.jsp?arnumber=4212667

[84] T. Isotalo, P. Lähdekorpi, and J. Lempiäinen, "**Improving HSDPA indoor coverage and throughput by repeater and dedicated indoor system**," *EURASIP Journal on Wireless Communications and Networking*, vol. 2008, Article ID 951481, 2008, doi: 10.1155/2008/951481.
http://www.hindawi.com/journals/wcn/2008/951481.pdf

[85] M. Jurvansuu, J. Prokkola, M. Hanski, and P. Perala, "**HSDPA performance in live networks**," in *Proc. IEEE International Conference on Communications 2007 (ICC 2007)*, pp. 467–471, June 2007, doi: 10.1109/ICC.2007.83.
http://ieeexplore.ieee.org/stamp/stamp.jsp?arnumber=4288754

[86] H. Holma and J. Reunanen, "**3GPP release 5 HSDPA measurements**," in *Proc. 17th IEEE International Symposium on Personal, Indoor and Mobile Radio Communications 2006 (PIMRC 2006)*, Sept. 2006, doi: 10.1109/PIMRC.2006.254116.
http://ieeexplore.ieee.org/stamp/stamp.jsp?arnumber=4022310

[87] M. Riback, S. Grant, G. Jongren, T. Tynderfeldt, D. Cairns, and T. Fulghum, "**MIMO-HSPA testbed performance measurements**," in *Proc. 18th IEEE International Symposium on Personal, Indoor and Mobile Radio Communications 2007 (PIMRC 2007)*, Sept. 2007, doi: 10.1109/PIMRC.2007.4394434.
http://ieeexplore.ieee.org/stamp/stamp.jsp?tp=&arnumber=4394434

[88] N. Johnston and H. Aghvami, "**Comparing WiMAX and HSPA – a guide to the technology**," *BT Technology Journal*, vol. 25, no. 2, pp. 191–199, Apr. 2007, doi: 10.1007/s10550-007-0044-2.
http://www.springerlink.com/content/v458565026g40989/fulltext.pdf

[89] K. J. Runarsdottir, "**Comparison of mobile WiMAX and HSDPA**," Master's thesis, KTH School of Information and Communications Technology (ICT), Department of Communication Systems (CoS), June 2008.
http://www.di.unipi.it/~ggiunta/comp1.pdf

[90] L. F. L. Salvado, "**Comparison between UMTS/HSDPA and WiMAX/IEEE 802.16e in mobility scenarios**," Master's thesis, Universidade Técnica de Lisboa, Instituto Superior Técnico, Feb. 2008.
https://dspace.ist.utl.pt/bitstream/2295/172830/1/tese_LS_FINAL.pdf

[91] A. Ghosh, D. R. Wolter, J. G. Andrews, and R. Chen, "**Broadband wireless access with WiMax/802.16: current performance benchmarks and future potential**," *IEEE Communications Magazine*, vol. 43, no. 2, pp. 129–136, 2005, doi: 10.1109/MCOM.2005.1391513.
http://ieeexplore.ieee.org/iel5/35/30297/01391513.pdf?tp=&arnumber=1391513

[92] I. S. Reed and G. Solomon, "**Polynomial codes over certain finite fields**," *Journal of the Society for Industrial and Applied Mathematics*, vol. 8, no. 2, pp. 300–304, June 1960.
http://www.jstor.org/stable/2098968

[93] P. Elias, "**Coding for noisy channels**," in *Proc. IRE Convention Record*, pp. 37–46, 1955.

[94] X.-Y. Hu, E. Eleftheriou, and D. Arnold, "**Regular and irregular progressive edge-growth tanner graphs**," *IEEE Transactions on Information Theory*, vol. 51, no. 1, pp. 386–398, Jan. 2005, doi: 10.1109/TIT.2004.839541.
http://ieeexplore.ieee.org/stamp/stamp.jsp?tp=&arnumber=1377521

[95] S. Caban, C. Mehlführer, G. Lechner, and M. Rupp, "**Testbedding MIMO HSDPA and WiMAX**," in *Proc. 70th IEEE Vehicular Technology Conference (VTC2009-Fall)*, Anchorage, AK, USA, Sept. 2009.
http://publik.tuwien.ac.at/files/PubDat_176574.pdf

[96] J.-J. van de Beek, O. Edfors, M. Sandell, S. K. Wilson, and P. O. Börjesson, "**On channel estimation in OFDM systems**," in *Proc. IEEE Vehicular Technology Conference (VTC 1995)*, vol. 2, pp. 815–819, Chicago, IL, USA, Sept. 1995, doi: 10.1109/VETEC.1995.504981.
http://ieeexplore.ieee.org/stamp/stamp.jsp?tp=&arnumber=504981

[97] M. Noh, Y. Lee, and H. Park, "**Low complexity LMMSE channel estimation for OFDM**," *IEE Proceedings-Communications*, vol. 153, no. 5, pp. 645–650, 2006.
http://ieeexplore.ieee.org/iel5/2191/36095/01714642.pdf?tp=&arnumber=1714642

[98] P. Robertson, E. Villebrun, and P. Hoeher, "**A comparison of optimal and sub-optimal MAP decoding algorithms operating in the log domain**," in *Proc. IEEE International Conference on Communications 1995 (ICC 1995)*, vol. 2, pp. 1009–1013, Seattle, WA, USA, June 1995, doi: 10.1109/ICC.1995.524253.
http://ieeexplore.ieee.org/stamp/stamp.jsp?tp=&arnumber=524253

[99] J. Jaldén and B. Ottersten, "**On the complexity of sphere decoding in digital communications**," *IEEE Transactions on Signal Processing*, vol. 53, no. 4, pp. 1474–1484, Apr. 2005, doi: 10.1109/TSP.2005.843746.
http://ieeexplore.ieee.org/stamp/stamp.jsp?tp=&arnumber=1408197

[100] C. Studer, M. Wenk, A. P. Burg, and H. Bölcskei, "**Soft-output sphere decoding: Performance and implementation aspects**," in *Conference Record of the 40th Asilomar Conference on Signals, Systems and Computers*, Pacific Grove, CA, USA, Nov. 2006.
http://ieeexplore.ieee.org/iel5/4176490/4176491/04176942.pdf?tp=&arnumber=4176942

[101] S. Caban, C. Mehlführer, A. L. Scholtz, and M. Rupp, "**Indoor MIMO transmissions with Alamouti space-time block codes**," in *Proc. 8th International Symposium on DSP and Communication Systems 2005 (DSPCS 2005)*, Noosa Heads, Australia, Dec. 2005.
http://publik.tuwien.ac.at/files/pub-et_9815.pdf

[102] A. J. Viterbi, "**Error bounds for convolutional codes and an asymptotically optimum decoding algorithm**," *IEEE Transactions on Information Theory*, vol. 13, no. 2, pp. 260–269, Apr. 1967.
http://ieeexplore.ieee.org/stamp/stamp.jsp?tp=&arnumber=1054010

[103] G. D. F. Jr., "**The Viterbi algorithm**," *Proceedings of the IEEE*, vol. 61, no. 3, pp. 268–278, Mar. 1973.
http://ieeexplore.ieee.org/stamp/stamp.jsp?tp=&arnumber=1450960

[104] L. Bahl, J. Cocke, F. Jelinek, and J. Raviv, "**Optimal decoding of linear codes for minimizing symbol error rate**," *IEEE Transactions on Information Theory*, vol. 20, no. 2, pp. 284–287, Mar. 1974.
http://ieeexplore.ieee.org/stamp/stamp.jsp?tp=&arnumber=1055186

[105] D. J. MacKay, "**Good error-correcting codes based on very sparse matrices**," *IEEE Transactions on Information Theory*, vol. 45, no. 2, pp. 399–431, Mar. 1999, doi: 10.1109/18.748992.
http://ieeexplore.ieee.org/stamp/stamp.jsp?tp=&arnumber=00748992

[106] J. H. Winters, "**On the capacity of radio communication systems with diversity in a Rayleigh fading environment**," *IEEE Journal on Selected Areas in Communications*, vol. 5, no. 5, pp. 871–878, June 1987.
http://ieeexplore.ieee.org/iel6/49/25831/01146600.pdf

[107] I. E. Telatar, "**Capacity of multi-antenna gaussian channels**," *European Transactions on Telecommunications, 1999, Technical Memorandum, Bell Laboratories, Lucent Technologies*, vol. 10, no. 6, pp. 585–595, Oct. 1998.
http://mars.bell-labs.com/papers/proof/proof.pdf

[108] G. J. Foschini and M. J. Gans, "**On limits of wireless communication in a fading environment when using multiple antennas**," *Wireless Personal Communications*, vol. 6, no. 3, pp. 311–335, 1998.
http://www.springerlink.com/content/h1n7866218781520/fulltext.pdf

[109] W. Hirt and J. Massey, "**Capacity of the discrete-time Gaussian channel with intersymbol interference**," *IEEE Transactions on Information Theory*, vol. 34, no. 3, pp. 380–388, May 1988, doi: 10.1109/18.6015.
http://ieeexplore.ieee.org/stamp/stamp.jsp?tp=&arnumber=6015

[110] J.-C. Belfiore, G. Rekaya, and E. Viterbo, "**The golden code: a 2x2 full-rate space-time code with nonvanishing determinants**," *IEEE Transactions on Information Theory*, vol. 51, no. 4, pp. 1432–1436, Apr. 2005, doi: 10.1109/TIT.2005.844069.
http://ieeexplore.ieee.org/stamp/stamp.jsp?tp=&arnumber=1412035

[111] A. Hottinen, Y. Hong, E. Viterbo, C. Mehlführer, and C. Mecklenbräuker, "**A comparison of high rate algebraic and non-orthogonal STBCs**," in *Proc. ITG/IEEE Workshop on Smart Antennas (WSA 2007)*, Vienna, Austria, Feb. 2007.
http://publik.tuwien.ac.at/files/pub-et_12314.pdf

[112] 3GPP, "**Technical specification group radio access network; physical layer procedures (FDD) (Tech. Spec. 25.214 V7.7.0)**," Nov. 2007.
http://www.3gpp.org/ftp/Specs/html-info/25214.htm

[113] H. Holma, A. Toskala, K. Ranta-aho, and J. Pirskanen, "**High-speed packet access evolution in 3GPP release 7**," *IEEE Communications Magazine*, vol. 45, no. 12, pp. 29–35, Dec. 2007, doi: 10.1109/MCOM.2007.4395362.
http://ieeexplore.ieee.org/stamp/stamp.jsp?arnumber=4395362

[114] H. Chao, Z. Liang, Y. Wang, and L. Gui, "**A dynamic resource allocation method for HSDPA in WCDMA system**," in *Proc. 5th IEE International Conference on 3G Mobile Communication Technologies 2004 (3G 2004)*, pp. 569–573, 2004.
http://ieeexplore.ieee.org/stamp/stamp.jsp?tp=&arnumber=1434541

[115] R. Naja, J.-P. Claude, and S. Tohme, "**Adaptive multi-user fair packet scheduling in HSDPA network**," in *Proc. International Conference on Innovations in Information Technology 2008 (IIT 2008)*, pp. 406–410, Dec. 2008, doi: 10.1109/INNOVATIONS.2008.4781652.
http://ieeexplore.ieee.org/stamp/stamp.jsp?tp=&arnumber=4781652

[116] R. Kwan, M. Aydin, C. Leung, and J. Zhang, "**Multiuser scheduling in HSDPA using simulated annealing**," in *Proc. International Wireless Communications and Mobile Computing Conference 2008 (IWCMC 2008)*, pp. 236–241, Aug. 2008, doi: 10.1109/IWCMC.2008.42.
http://ieeexplore.ieee.org/stamp/stamp.jsp?tp=&arnumber=4599941

[117] R. Tresch, C. Mehlführer, and M. Guillaud, "**LMMSE channel estimation for MIMO W-CDMA with out-of-cell interference mitigation**," in *Conference Record of the 42nd Asilomar Conference on Signals, Systems and Computers*, pp. 331–335, Pacific Grove, CA, USA, Oct. 2008, doi: 10.1109/ACSSC.2008.5074419.
http://publik.tuwien.ac.at/files/PubDat_167781.pdf

[118] T. K. Moon and W. C. Stirling, *Mathematical Methods and Algorithms for Signal processing*, 1st ed. Upper Saddle River, NJ: Prentice Hall, 2000.

[119] K. B. Petersen and M. S. Pedersen, Eds., *The Matrix Cookbook*, 2008, November 14.
http://matrixcookbook.com

[120] M. Harteneck, M. Boloorian, S. Georgoulis, and R. Tanner, "**Practical aspects of an HSDPA 14 Mbps terminal**," in *Conference Record of the 38th Asilomar Conference on Signals, Systems and Computers, 2004*, vol. 1, pp. 799–803, Pacific Grove, CA, USA, Nov. 2004.
http://ieeexplore.ieee.org/stamp/stamp.jsp?arnumber=1399246

[121] M. Harteneck, M. Boloorian, S. Georgoulis, and R. Tanner, "**Throughput measurements of HSDPA 14 Mbit/s terminal**," *Electronics Letters*, vol. 41, no. 7, pp. 425–427, Mar. 2005, doi: 10.1049/el:20058362. http://ieeexplore.ieee.org/stamp/stamp.jsp?arnumber=1421242

[122] C. Mehlführer, S. Caban, and M. Rupp, "**Measurement based evaluation of low complexity receivers for D-TxAA HSDPA**," in *Proc. 16th European Signal Processing Conference (EUSIPCO 2008)*, Lausanne, Switzerland, Aug. 2008. http://publik.tuwien.ac.at/files/PubDat_166132.pdf

[123] M. Wrulich, C. Mehlführer, and M. Rupp, "**Interference aware MMSE equalization for MIMO TxAA**," in *Proc. 3rd International Symposium on Communications, Control and Signal Processing (ISCCSP 2008)*, pp. 1585–1589, St. Julians, Malta, Mar. 2008, doi: 10.1109/ISCCSP.2008.4537480. http://publik.tuwien.ac.at/files/pub-et_13657.pdf

[124] C. Mehlführer, M. Wrulich, and M. Rupp, "**Intra-cell interference aware equalization for TxAA HSDPA**," in *Proc. 3rd IEEE International Symposium on Wireless Pervasive Computing (ISWPC 2008)*, pp. 406–409, Santorini, Greece, May 2008, doi: 10.1109/ISWPC.2008.4556239. http://publik.tuwien.ac.at/files/pub-et_13749.pdf

[125] M. Wrulich, C. Mehlführer, and M. Rupp, "**Managing the interference structure of MIMO HSDPA: A multi-user interference aware MMSE receiver with moderate complexity**," *IEEE Transactions on Wireless Communications*, accepted.

[126] M. Wrulich, C. Mehlführer, and M. Rupp, "**Advanced receivers for MIMO HSDPA**," in *HSDPA/HSUPA Handbook*, B. Furht and S. Ahson, Eds.   CRC Press, 2009, submitted.

[127] L. Mailaender, "**Linear MIMO equalization for CDMA downlink signals with code reuse**," *IEEE Transactions on Wireless Communications*, vol. 4, no. 5, pp. 2423– 2434, Sept. 2005. http://ieeexplore.ieee.org/iel5/7693/32683/01532226.pdf

[128] S. Geirhofer, C. Mehlführer, and M. Rupp, "**Design and real-time measurement of HSDPA equalizers**," in *Proc. 6th IEEE Workshop on Signal Processing Advances in Wireless Communications (SPAWC 2005)*, pp. 166–170, New York City, USA, June 2005, doi: 10.1109/SPAWC.2005.1505893. http://publik.tuwien.ac.at/files/pub-et_9722.pdf

[129] Y. Guo, J. Zhang, D. McCain, and J. Cavallaro, "**Efficient MIMO equalization for downlink multi-code CDMA: complexity optimization and comparative study**," in *Proc. 47th IEEE Global Telecommunications Conference 2004 (GLOBECOM 2004)*, vol. 4, pp. 2513–2519, Nov. 2004, doi: 10.1109/GLOCOM.2004.1378459. http://ieeexplore.ieee.org/stamp/stamp.jsp?arnumber=1378459

[130] Y. Guo, J. Zhang, D. McCain, and J. R. Cavallaro, "**An efficient circulant MIMO equalizer for CDMA downlink: Algorithm and VLSI architecture**," *EURASIP Journal on Applied Signal Processing*, vol. 2006, Article ID 57134, 2006, doi: 10.1155/ASP/2006/57134. http://www.hindawi.com/GetPDF.aspx?doi=10.1155/ASP/2006/57134

[131] G. H. Golub and C. F. van Loan, Eds., *Matrix Computations*, 3rd ed.   The Johns Hopkins University Press, 1996.

[132] C. Mehlführer and M. Rupp, "**A robust MMSE equalizer for MIMO enhanced HSDPA**," in *Conference Record of the 40th Asilomar Conference on Signals, Systems and Computers*, pp. 129–133, Pacific Grove, CA, USA, Oct. 2006, doi: 10.1109/ACSSC.2006.356599. http://publik.tuwien.ac.at/files/pub-et_11498.pdf

[133] D. Garrett, G. Woodward, L. Davis, G. Knagge, and C. Nicol, "**A 28.8 Mb/s 4x4 MIMO 3G high-speed downlink packet access receiver with normalized least mean square equalization**," in *Digest of Technical Papers IEEE International Solid-State Circuits Conference 2004 (ISSCC 2004)*, vol. 1, pp. 420–536, Feb. 2004, doi: 10.1109/ISSCC.2004.1332773.
http://ieeexplore.ieee.org/stamp/stamp.jsp?arnumber=1332773

[134] B. Hassibi and B. Hochwald, "**How much training is needed in multiple-antenna wireless links?**" *IEEE Transactions on Information Theory*, vol. 49, no. 4, pp. 951–963, Apr. 2003, doi: 10.1109/TIT.2003.809594.
http://ieeexplore.ieee.org/stamp/stamp.jsp?arnumber=1193803

[135] A. Szabo, N. Geng, A. Seeger, and W. Utschick, "**Investigations on link to system level interface for MIMO systems**," in *Proc. 3rd International Symposium on Image and Signal Processing and Analysis 2003 (ISPA2003)*, pp. 365–369, Rome, Italy, Sept. 2003.
http://ieeexplore.ieee.org/iel5/9084/28837/01296924.pdf?tp=&isnumber=&arnumber=1296924

[136] "**Recommendation ITU-R M.1225: Guidelines for evaluation of radio transmission technologies for IMT-2000**," Tech. Rep., 1997.

[137] Ericsson, "**64-QAM for HSDPA - link level simulation results**," 3GPP, Tech. Rep. TSG-RAN Working Group 1 Meeting #46, R1-062264, Aug. 2006.
http://www.3gpp.org/ftp/tsg_ran/WG1_RL1/TSGR1_46/Docs/R1-062264.zip

[138] J. A. García-Naya, C. Mehlführer, S. Caban, M. Rupp, and C. Luis, "**Throughput-based antenna selection measurements**," in *Proc. 70th IEEE Vehicular Technology Conference (VTC2009-Fall)*, Anchorage, AK, USA, Sept. 2009.
http://publik.tuwien.ac.at/files/PubDat_176573.pdf

[139] P. Xia, S. Zhou, and G. B. Giannakis, "**Adaptive MIMO-OFDM based on partial channel state information**," *IEEE Transactions on Signal Processing*, vol. 52, no. 1, pp. 202–213, 2004.
http://ieeexplore.ieee.org/iel5/78/28059/01254037.pdf?tp=&arnumber=1254037

[140] D. Bosanska, C. Mehlführer, and M. Rupp, "**Channel adaptive OFDM systems with packet error ratio adaptation**," in *Proc. International ITG Workshop on Smart Antennas (WSA 2009)*, Berlin, Germany, Feb. 2009.
http://publik.tuwien.ac.at/files/PubDat_175538.pdf

[141] J. Ylioinas, K. Hooli, K. Kiiskila, and M. Juntti, "**Interference suppression in MIMO HSDPA communication**," in *Proc. of the 6th Nordic Signal Processing Symposium 2004 (NORSIG 2004)*, pp. 228–231, 2004.
http://ieeexplore.ieee.org/stamp/stamp.jsp?arnumber=1344565

[142] G. G. Raleigh and J. M. Cioffi, "**Spatio-temporal coding for wireless communication**," *IEEE Transactions on Communications*, vol. 46, no. 3, pp. 357–366, Mar. 1998, doi: 10.1109/26.662641.
http://www-isl.stanford.edu/~cioffi/dsm/wlpap/mimocioffi98.pdf

[143] A. Paulraj, R. Nabar, and D. Gore, Eds., *Introduction to Space-Time Wireless Communications*, 1st ed. Cambridge University Press, 2003.

[144] E. Dahlman, S. Parkvall, J. Sköld, and P. Beming, *3G Evolution – HSPA and LTE for Mobile Broadband*, 1st ed. Academic Press, 2007.

[145] E. Dahlman, H. Ekstrom, A. Furuskar, Y. Jading, J. Karlsson, M. Lundevall, and S. Parkvall, "**The 3G long-term evolution - radio interface concepts and performance evaluation**," in *Proc. 63rd IEEE Vehicular Technology Conference 2006 (VTC2006-Spring)*, vol. 1, pp. 137–141, May 2006, doi: 10.1109/VETECS.2006.1682791.
http://ieeexplore.ieee.org/stamp/stamp.jsp?arnumber=1682791

[146] H. Ekstrom, A. Furuskar, J. Karlsson, M. Meyer, S. Parkvall, J. Torsner, and M. Wahlqvist, "**Technical solutions for the 3G long-term evolution**," *IEEE Communications Magazine*, vol. 44, no. 3, pp. 38–45, Mar. 2006, doi: 10.1109/MCOM.2006.1607864.
http://ieeexplore.ieee.org/stamp/stamp.jsp?arnumber=1607864

[147] S. Parkvall, E. Dahlman, A. Furuskar, Y. Jading, M. Olsson, S. Wanstedt, and K. Zangi, "**LTE-advanced - evolving LTE towards IMT-advanced**," in *Proc. 68th IEEE Vehicular Technology Conference 2008 (VTC2008-Fall)*, Sept. 2008, doi: 10.1109/VETECF.2008.313.
http://ieeexplore.ieee.org/stamp/stamp.jsp?arnumber=4657145

[148] M. Tanno, Y. Kishiyama, N. Miki, K. Higuchi, and M. Sawahashi, "**Evolved UTRA - physical layer overview**," in *Proc. IEEE 8th Workshop on Signal Processing Advances in Wireless Communications 2007 (SPAWC 2007)*, June 2007, doi: 10.1109/SPAWC.2007.4401427.
http://ieeexplore.ieee.org/stamp/stamp.jsp?arnumber=4401427

[149] J. J. Sánchez, D. Morales-Jiménez, G. Gómez, and J. T. Enbrambasaguas, "**Physical layer performance of long term evolution cellular technology**," in *Proc. 16th IST Mobile and Wireless Communications Summit 2007*, July 2007, doi: 10.1109/ISTMWC.2007.4299090.
http://ieeexplore.ieee.org/stamp/stamp.jsp?arnumber=4299090

[150] T. Tang and R. Heath, "**Opportunistic feedback for downlink multiuser diversity**," *IEEE Communications Letters*, vol. 9, no. 10, pp. 948–950, Oct. 2005, doi: 10.1109/LCOMM.2005.10002.
http://ieeexplore.ieee.org/stamp/stamp.jsp?tp=&arnumber=1515679

[151] A. Gyasi-Agyei, "**Multiuser diversity based opportunistic scheduling for wireless data networks**," *IEEE Communications Letters*, vol. 9, no. 7, pp. 670–672, July 2005, doi: 10.1109/LCOMM.2005.1461700.
http://ieeexplore.ieee.org/stamp/stamp.jsp?tp=&arnumber=1461700

[152] J. Andrews, "**Interference cancellation for cellular systems: a contemporary overview**," *IEEE Transactions on Wireless Communications*, vol. 12, no. 2, pp. 19–29, Apr. 2005, doi: 10.1109/MWC.2005.1421925.
http://ieeexplore.ieee.org/stamp/stamp.jsp?arnumber=1421925

[153] A. Simonsson, "**Frequency reuse and intercell interference co-ordination in E-UTRA**," in *Proc. 65th IEEE Vehicular Technology Conference 2007 (VTC2007-Spring)*, pp. 3091–3095, Apr. 2007, doi: 10.1109/VETECS.2007.633.
http://ieeexplore.ieee.org/stamp/stamp.jsp?arnumber=4213061

[154] H. Zhang, L. Venturino, N. Prasad, and S. Rangarajan, "**Distributed inter-cell interference mitigation in OFDMA wireless data networks**," in *Proc. 4th IEEE Broadband Wireless Access Workshop*, New Orleans, LA, USA, Dec. 2008.

[155] C. Mehlführer, M. Wrulich, J. C. Ikuno, D. Bosanska, and M. Rupp, "**Simulating the long term evolution physical layer**," in *Proc. 17th European Signal Processing Conference (EUSIPCO 2009)*, Glasgow, Scotland, UK, Aug. 2009.
http://publik.tuwien.ac.at/files/PubDat_175708.pdf

[156] "**LTE simulator homepage**."
http://www.nt.tuwien.ac.at/ltesimulator/

[157] M. Rupp, C. Mehlführer, S. Caban, R. Langwieser, L. W. Mayer, and A. L. Scholtz, "**Testbeds and rapid prototyping in wireless system design**," *EURASIP Newsletter*, vol. 17, no. 3, pp. 32–50, Sept. 2006.
http://publik.tuwien.ac.at/files/pub-et_11232.pdf

[158] E. Aschbacher, S. Caban, C. Mehlführer, G. Maier, and M. Rupp, "**Design of a flexible and scalable 4x4 MIMO testbed**," in *Proc. 11th IEEE Signal Processing Workshop (DSP 2004)*, pp. 178–181, Taos Ski Valley, NM, USA, Aug. 2004, doi: 10.1109/DSPWS.2004.1437937.
http://publik.tuwien.ac.at/files/pub-et_8758.pdf

[159] S. Caban, R. Langwieser, C. Mehlführer, E. Aschbacher, W. Keim, G. Maier, B. Badic, M. Rupp, and A. L. Scholtz, "**Design and verification of a flexible and scalable 4x4 MIMO testbed**," in *Slides, Workshop on MIMO Implementation Aspects (RAWCON 2004)*, Atlanta, GA, USA, Sept. 2004.
http://publik.tuwien.ac.at/files/pub-et_9210.pdf

[160] C. Mehlführer, S. Geirhofer, S. Caban, and M. Rupp, "**A flexible MIMO testbed with remote access**," in *Proc. 13th European Signal Processing Conference (EUSIPCO 2005)*, Antalya, Turkey, Sept. 2005.
http://publik.tuwien.ac.at/files/pub-et_9732.pdf

[161] "**Kathrein KG**."
http://www.kathrein.de/

[162] S. Caban, "**Testbed-based evaluation of mobile communication systems**," Ph.D. dissertation, Technische Universität Wien, Institut für Nachrichtentechnik und Hochfrequenztechnik, Sept. 2009, supervisor: Markus Rupp.

[163] C. Kakoyiannis, S. Troubouki, and P. Constantinou, "**Design and implementation of printed multi-element antennas on wireless sensor nodes**," in *Proc. 3rd International Symposium on Wireless Pervasive Computing 2008 (ISWPC 2008)*, pp. 224–228, Santorini, Greece, May 2008, doi: 10.1109/ISWPC.2008.4556202.
http://ieeexplore.ieee.org/stamp/stamp.jsp?arnumber=4556202

[164] A. Habib, C. Mehlführer, and M. Rupp, "**Performance comparison of antenna selection algorithms in WiMAX with link adaptation**," in *Proc. 4th International Conference on Cognitive Radio Oriented Wireless Networks and Communications (CROWNCOM 2009)*, Hannover, Germany, June 2009.
http://publik.tuwien.ac.at/files/PubDat_176038.pdf

[165] B. Efron and D. V. Hinkley, *An Introduction to the Bootstrap (CRC Monographs on Statistics & Applied Probability 57)*, 1st ed. Chapman & Hall, 1994.

[166] S. M. Kay, *Fundamentals of Statistical Signal Processing: Estimation Theory.* Upper Saddle River, NJ: Prentice Hall, 1993, vol. 1.